1-1-2019

Nanoscale Thermal Transport in Thermally Isolated Nanostructures

Brian G. Green
University of Denver

Nanoscale Thermal Transport in Thermally Isolated Nanostructures

Abstract

Experiments with nanoscale structures, designed to measure some of their thermal and optical properties, are the subjects of this dissertation. We studied the transport of thermal energy in systems of nanoparticles, and used the method of transient thermoreflectance to monitor those dynamics, and assess whether thermal transport features special to nanoscale systems emerged. This same method was also used to study the thermal transport of a single system of layered membranes. Optical properties were investigated using computational simulations of a nanoparticle system, using the method of finite-difference time-domain simulation.

In nanoparticle studies, there are two features of interest special to nanoscale systems: the transition from diffusive to ballistic thermal transport, and the presence of thermal resistance at interfaces. Our platform for studying these features was a system of gold nanoparticles, having citrate capping layers, and embedded in a polymer matrix. Our transient thermoreflectance method uses an ultrafast, infrared, pulsed laser to impulsively heat the particles, with an initial laser pulse, then measures the power of a second pulse, which reflects from the particles at a controlled delay time following the heating. The reflected power depends on the steadily decreasing temperature of the particles, and collecting this data over a range of delay times provides a picture of the nanoparticles' cooling dynamics. We have developed the first multilayer, spherical model of this diffusive cooling process, explicitly including interfacial boundary resistance. By adjusting it to our measurement results, we determine the amount of boundary resistance, the capping layer thickness, and the thermal conductivity of the matrix. Though we do not observe ballistic transport in this system, we have measured both the first value of the gold/polymer interfacial thermal resistance, and the capping layer thickness, and found both of them to significantly affect the transport of thermal energy.

Thermal boundary resistance was also a property of interest in our membrane systems, which consisted of a suspended bridge structure of a molybdenum (Mo) film deposited on a silicon nitride (SiN) substrate. This thermal isolation structure, designed and fabricated by our collaborators, enabled us to test whether the substrate material retains its bulk value of thermal conductivity and heat capacity at the nanoscale, which must otherwise be assumed in larger-scale experiments. Using transient thermoreflectance to monitor the thermal dynamics following impulsive heating of the upper surface of the metal film, we have measured the thermal boundary resistance present at the Mo/SiN interface, and found that, within experimental uncertainties, the bulk SiN conductivity and heat capacity values are retained.

In a separate study, we modeled the optical absorption properties of gold nanoparticles, in the visible range, using the method of finite-difference time-domain simulation. This method calculates the change induced in an incident pulse of visible light as it propagates past a particle, placed in a water matrix, and finds the fraction of the pulse's electromagnetic energy absorbed by the particle. The energy absorbed is determined by the dielectric properties of gold -- one picture of which is the Lorentz-Drude model, which derives dielectric properties from electron scattering behavior and resonances. Fitting this model to literature dielectric data, we predict an absorption spectrum which agrees with experimental values within several nanometers.

Document Type

Dissertation

Degree Name

Ph.D.

Nanoscale Thermal Transport in Thermally Isolated Nanostructures

---

A Dissertation

Presented to

the Faculty of Natural Sciences and Mathematics

University of Denver

In Partial Fulfillment

of the Requirements for the Degree

Doctor of Philosophy

---

by

Brian G. Green

June 2019

Advisor: Prof. Mark E. Siemens

Abstract

Author: Brian G. Green
Title: Nanoscale Thermal Transport in Thermally Isolated Nanostructures
Advisor: Prof. Mark E. Siemens
Degree date: June 2019

Experiments with nanoscale structures, designed to measure some of their thermal and optical properties, are the subjects of this dissertation. We studied the transport of thermal energy in systems of nanoparticles, and used the method of transient thermoreflectance to monitor those dynamics, and assess whether thermal transport features special to nanoscale systems emerged. This same method was also used to study the thermal transport of a single system of layered membranes. Optical properties were investigated using computational simulations of a nanoparticle system, using the method of finite-difference time-domain simulation.

In nanoparticle studies, there are two features of interest special to nanoscale systems: the transition from diffusive to ballistic thermal transport, and the presence of thermal resistance at interfaces. Our platform for studying these features was a system of gold nanoparticles, having citrate capping layers, and embedded in a polymer matrix. Our transient thermoreflectance method uses an ultrafast, infrared, pulsed laser to impulsively heat

the particles, with an initial laser pulse, then measures the power of a second pulse, which reflects from the particles at a controlled delay time following the heating. The reflected power depends on the steadily decreasing temperature of the particles, and collecting this data over a range of delay times provides a picture of the nanoparticles' cooling dynamics. We have developed the first multilayer, spherical model of this diffusive cooling process, explicitly including interfacial boundary resistance. By adjusting it to our measurement results, we determine the amount of boundary resistance, the capping layer thickness, and the thermal conductivity of the matrix. Though we do not observe ballistic transport in this system, we have measured both the first value of the gold/polymer interfacial thermal resistance, and the capping layer thickness, and found both of them to significantly affect the transport of thermal energy.

Thermal boundary resistance was also a property of interest in our membrane systems, which consisted of a suspended bridge structure of a molybdenum (Mo) film deposited on a silicon nitride (SiN) substrate. This thermal isolation structure, designed and fabricated by our collaborators, enabled us to test whether the substrate material retains its bulk value of thermal conductivity and heat capacity at the nanoscale, which must otherwise be assumed in larger-scale experiments. Using transient thermoreflectance to monitor the thermal dynamics following impulsive heating of the upper surface of the metal film, we have measured the thermal boundary resistance present at the Mo/SiN interface, and found that, within experimental uncertainties, the bulk SiN conductivity and heat capacity values are retained.

In a separate study, we modeled the optical absorption properties of gold nanoparticles, in the visible range, using the method of finite-difference time-domain simulation. This method calculates the change induced in an incident pulse of visible light as it propagates past a particle, placed in a water matrix, and finds the fraction of the pulse's electromagnetic energy absorbed by the particle. The energy absorbed is determined by the dielectric properties of gold – one picture of which is the Lorentz-Drude model, which derives dielectric properties from electron scattering behavior and resonances. Fitting this model to literature dielectric data, we predict an absorption spectrum which agrees with experimental values within several nanometers.

Acknowledgements

My heartfelt thanks go to my adviser Mark E. Siemens, and wife Kathryn Lucatelli, for their constant support. I am greatly thankful for the work performed by collaborators Sarah Mason and Stephen Budy in fabricating the samples used in these studies. My thanks also go to committee members Barry Zink, Xin Fan, and Mohammed Matin, and additionally to faculty Michelle Knowles (University of Denver) and Scott Reed (University of Colorado Denver). Many dear friends and family are owed my thanks as well, including John Hicks, Jennifer Stevenson, and Navead and Rachel Jensen.

Table of Contents

Chapter

List of Tables

Table

List of Figures

Figure

Chapter 1

Introduction

1.1 Physical systems which impel the study of nanoscale thermal transport

Multiple developing technologies continue to claim the advantages made possible by devices engineered at the nanoscale. The diversity of applications where siginificant or dramatic progress are enabled through nanotechnology is represented by examples in continually smaller and more powerful microelectronics; nanostructured, advanced materials, both solid and fluid, with enhanced properties; nano-sensors, including chemical sensing devices; medical applications in nanophototherapy, medical imaging and drug delivery; efficiency of chemical catalyts; and optical applications, including improved laser gain media and potential photovoltaic light trapping. Understanding these new systems includes understanding their thermal properties, and is essential for tasks such as optimizing thermal management of microelectronics, developing effective and efficient enhanced materials, and designing the nanoscale thermal devices of medical applications.

Accompanying the exciting developments that lie on the path to progressively smaller devices are challenges which are inherent in their advantageous small size: physical realities that bring into question, and eventually negate, the validity of previously accurate, classical approximations, as the nanometer scale is approached and entered. In the case of nanoscale thermal physics, the most significant considerations are the finite, *i.e.* non-zero, phonon

mean-free-path, and the finite, also non-zero, resistance of thermal interfaces. In particular, the increasing difficulty in controlling climbing temperatures in microelectronics, a recognized barrier to reducing device sizes, is due to both of these effects. In the case of medical nanoparticles used as nanoscale thermal sources, the choices of particle core and capping materials is significantly affected by thermal resistance at interfaces.

For macroscale systems, thermal dynamics are understood through proven, classical physical science. This understanding is theoretically grounded in the laws of thermodynamics, and material properties, primarily specific heat and thermal conductivity, are well-defined. The resulting ability to accurately predict system temperatures from known heating, material properties, and dimensions, is especially important and valuable. In fact, the classical theory even seems to incorporate and account for nanoscale considerations, at least initially: the concept of the mean-free-path is a basic part of the physical picture, and boundary resistance is represented properly and quantitatively in calculations.

However, in truly nanoscale systems, limitations of the classical method clearly emerge. Predictions increasingly and significantly underestimate temperatures as the nanoscale is approached. Just as importantly, the model of interface resistance is phenomenological only, *i.e.* it has no capability for, or intention of, predicting the interface resistance between two given materials.

The developing theories and experimental methods of nanoscale thermal physics address all of the above considerations.[1] In these studies in particular, we will examine the transition from a macro- to a nanoscale picture, begin to understand theories of thermal dynamics and interface resistance, and validate a theoretical interface resistance prediction with our experimental results. We continue with an outline of the successive sections of this dissertation.

1.2 Outline

In chapter 2, we begin by developing a physical picture of thermal transport, presenting two different intuitions of how transport occurs in macroscopic solids, and show that they both lead to the same fundamental, characteristic equation, the classical heat equation. We discuss how the heat equation is used to predict the specific distribution of temperatures resulting from a known source of heating, for both spherical and planar geometries.

Chapter 3 moves our study to the nanoscale, considering special features of transport which emerge there, the property of thermal boundary resistance in particular. We describe theories that move away from the classical continuum picture, toward the implications of lattice structure for available vibrational energies, and the effect of small scales on the transport of this energy. We also estimate the scales of length and time which are implied by this nanoscale picture, and which are required by the structures we employ to study nanoscale effects.

With an understanding in place of the physical mechanisms and systems being considered, chapter 4 describes the experimental method of transient thermoreflectance. We discuss how pulses from an ultrafast laser and the property of thermoreflectance work together in an apparatus capable of monitoring cooling dynamics at the time and length scales required by the nanoscale systems of chapter 3. The TTR description is completed by sections on additional components which provide the apparatus with its required sensitivity and stability.

Chapter 5 presents the studies of nanoscale thermal transport in a nanoparticle system. After reviewing some existing related studies, we describe in detail the design of our TTR apparatus for sensitive measurements of the nanoscale properties of interest. Here we

also derive a multilayer theoretical model of the TTR signal which is required to calculate thermal parameters from our data. We present the first simultaneous measurement of both TBR and capping layer thickness in the same NP system.

Chapter 6 begins with examples of experiments studying nanoscale thermal properties, using TTR with thin films on thick substrates, and points out some assumptions which were required in order to calculate numerical results. We then describe the thermal isolation platform structure, with its thin underlying substrate, and how our experiments were designed to test these assumptions. Our initial results suggest that the assumptions are valid in the case of thin metal films on thin membranes, and demonstrate the effectiveness of the TTR method in nanoscale transport studies on membranes. An accepted planar model of the TTR signal is applied to the calculation of our results.

We move from thermal to optical properties of gold NPs in chapter 7, with a description of the role of their absorption spectra in chemical sensing experiments and other applications. The FDTD computational method simulates the interaction of an NP with an incident pulse of visible light, and the calculation of absorption properties from this interaction is described. The features of the resulting spectrum are determined by the underlying dielectric function of gold, literature values of which vary significantly. We show that by fitting the Lorentz-Drude model of the dielectric function to recently published data, we predict absorption spectra that agree closely with experimental absorption results.

NP thermal transport and absorption simulation results are summarized in chapter 8, and we consider some interesting ideas for future studies suggested by these findings.

Chapter 2

Diffusive Thermal Transport

2.1 Equivalence of continuum and random walk pictures

Before beginning a description of the thermal systems used in these thermal transport studies, let's prepare tools that will enable the calculation of the thermal properties of interest from measurements made on those systems. Thermal properties such as TBR define how a system behaves when it possesses a given amount of thermal energy, and also how it responds to a change in that energy. In our experiments, we observe the response to energy changes in the form of system heating, and its response is its resulting temperature. So we are seeking a model that relates observed, changing temperatures, as the system heats or cools, at whatever location in the system the measurement is done, to known heating. We vary property values appearing in the model to match measurement data, thereby calculating a property value, if measured temperatures are sufficiently sensitive to the property's value.

So how does heating a certain material determine how temperatures respond over time, at a certain location in the system? Intuition suggests some key ideas: after heating has occurred, temperatures begin to decrease, so thermal energy must be moving, i.e. transport is happening; it seems natural that the hotter temperatures are, relative to surroundings, the faster the energy would move; the motion isn't the result of any directed

force, though, so it must move randomly, in such a way that it speads out over time; thermal energy in a solid must represent the vibrational energy of its atoms and molecules.

To make the first two above ideas quantitative, if hotter (compared to surroundings) means faster, then the thermal energy flow per unit area f, the thermal flux, must increase with the rate of temperature T decrease with distance x. Let's call this idea "continuum transport." Direct proportionality is the simplest such relation:

$$f \;\propto\; -\frac{\mathrm{d}T}{\mathrm{d}x} \tag{2.1}$$

for temperature decreasing along the x-axis. Relation (2.1) would be true at any point $\mathbf{r}$, at any time t, in the system, and extending it to three dimensions gives Fourier's law:

$$\mathbf{f}(\mathbf{r},t) = -k\ \nabla T(\mathbf{r},t) \tag{2.2}$$

where k is the thermal conductivity of the material. This is a classical, first step in predicting the field of temperatures caused by heating.

Returning to the ideas of vibrational energy and random motion, vibrational energy in a finite space is quantized on the atomic scale, so we can picture thermal transport as the random motion, in a series of steps of varying length, of individual thermal energy units, *phonons*. This picture of transport is reasonably thought to be the net result of more phonons diffusing *from* a higher energy-density, warmer region, than the diffusion *to* the same region from an adjacent, cooler, lower energy-density region. Calling this picture "diffusive transport," let's again write the flux in terms of temperature. With l the mean step length, the *mean free path*, and t the mean step duration, the mean *relaxation time*, consider a 1D space with temperature decreasing in the x-direction, on overall length scale $L \gg l$. Let's calculate the flux between two adjacent regions of length l, with total thermal energies E_i and energy densities e_i related by $E_i = e_i l$, and temperatures T_i. Over one relaxation time, since the phonon transport is random, and there are two options for the

direction of transport, half the energy in each region must cross the boundary between the two, as shown in figure 2.1, so the mean flux is

$$f(x,t) = \frac{\frac{E_1(x,t)}{2} - \frac{E_2(x,t)}{2}}{t} = -\frac{1}{2}\frac{l}{t}(e_2(x,t) - e_1(x,t)) = -\frac{1}{2}\frac{l^2}{t}\frac{e_2(x,t) - e_1(x,t)}{l}. \tag{2.3}$$

Since $l \ll L$, the last factor is $\frac{\partial e}{\partial x}$, and the flux becomes

$$f(x,t) = -\alpha\frac{\partial e(x,t)}{\partial x}, \tag{2.4}$$

with the diffusivity $\alpha = \frac{l^2}{2t}$. We're seeking flux in terms of temperature, and (2.4) is in terms of energy density, but the two are related through the volumetric specific heat $c_V = \frac{\partial e(\mathbf{r},t)}{\partial T}$, giving

$$f(x,t) = -\alpha\frac{\partial e(x,t)}{\partial T}\frac{\partial T(x,t)}{\partial x} = -\alpha c_v\frac{\partial T(x,t)}{\partial x}. \tag{2.5}$$

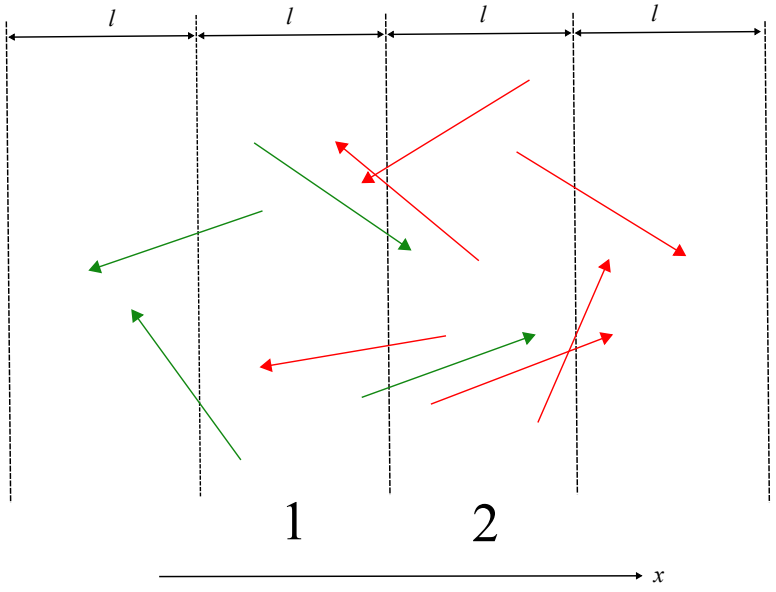

Figure 2.1: Projecting a single step of diffusion along one dimension x, between regions 1 and 2. Each phonon path is of mean length l. Green paths originate in region 1, red in region 2. Each may move in either the $+x$ or $-x$ direction, with equal numbers of each case. There is a net flow of thermal energy from region 2 to region 1.

The 3D extension is again Fourier's law,

$$\mathbf{f}(\mathbf{r},t) = -k\nabla T(\mathbf{r},t), \tag{2.6}$$

with diffusivity defined by $k = \alpha c_v$. This result indicates that it is the diffusion transport picture that actually underlies the continuum picture. We have assumed that conductivities and specific heats are material properties independent of space and time, and that the scale of the system is much larger than the phonon mean free path. Within these limits, the continuum and diffusive intuitions both lead to the same equation for flux and temperature, indicating that both pictures are equally and simultaneously correct. In the chapters that follow, the continuum picture most easily leads to the boundary conditions required to predict a temperature distribution from input heating, while the diffusion picture will lend itself to theoretical calculation of the main nanoscale quantity of interest, the thermal boundary resistance.

2.2 The heat equation

Fourier's law (2.2) relates flux and temperature to each other, but if we're seeking an expression for temperature only, let's look at the flux term: it's the energy flow at a point, and energy and temperature changes are related by the material's isochoric heat capacity, so writing flux in terms of energy could eliminate flux from the expression, leaving just temperature, as desired. Energy conservation is exactly the flux/energy connection we need. Vibrational energy would have to be attributed to a finite volume V of material instead of only a point, so the flux through the enclosing surface S must be the rate of decrease of the volume's energy E:

$$\oint_S \mathbf{f}(\mathbf{r},t)\cdot \mathrm{d}\mathbf{a} = -\frac{\partial E(\mathbf{r},t)}{\partial t}. \tag{2.7}$$

Again utilizing the volumetric specific heat c_v allows the RHS of (2.7) to be written as a function of temperature:

$$-\frac{\partial E(\mathbf{r},t)}{\partial t} = -\int_V \frac{\partial e(\mathbf{r},t)}{\partial T}\frac{\partial T}{\partial t}\mathrm{d}V = -c_v \int_V \frac{\partial T}{\partial t}\mathrm{d}V. \tag{2.8}$$

Applying the divergence theorem to the LHS of (2.7), with the arbitrarily-chosen V allowing the volume integration to be dropped, leaves

$$\nabla \cdot \mathbf{f}(\mathbf{r},t) = -c_v \frac{\partial T(\mathbf{r},t)}{\partial t}, \tag{2.9}$$

and $\mathbf{f}(\mathbf{r},t)$ is eliminated by equating the divergence of (2.2) with (2.9):

$$\nabla^2 T(\mathbf{r},t) = \frac{1}{\alpha}\frac{\partial T(\mathbf{r},t)}{\partial t}. \tag{2.10}$$

This is the classical *heat equation*, expressing the conditions on the temperature field $T(\mathbf{r},t)$ implied by the ideas of continuum transport, diffusive tranport, and energy conservation. It is the primary tool we will use to predict the response of our thermal systems to heating, as shown in the following sections. In the particular experimental systems studied here, the region of heating is well approximated by a surface area, as opposed to body heating, and is described in section 2.4 on boundary conditions. With no body heating term needed in the homogeneous heat equation (2.10), we move on to solutions for the temperature.

2.3 Steady-state planar and spherical solutions in infinite media

The TTR experimental method specifically measures the time-domain response of a system to heating - impulsive heating, in our case, so we will need to solve the heat equation (2.10) for the time-dependent temperature field due to a train of heating pulses. The heat equation is linear, and as mentioned all of the thermal parameters (including the TBR quantity defined below) are time-invariant. For systems that are linear and time-invariant

(LTI), Fourier analysis and superposition directly provide the temperature solution as the net response to the sinusoidal frequencies making up the impulsive heating input.

So if we need the response to certain frequencies as a prior step to calculating the time-domain response, let's convert the heat equation to the frequency domain for a given angular frequency ω. For the planar case, we expect a cylindrical geometry centered around the optical axis of the heating beam – this is the approach used in the widely-used model of Cahill,[2] in which the solution is calculated as an integration over a radial distribution of periodic point sources. In this section we'll establish the solution for a point source at the origin,[3] and extend it to the cylindrical geometry in section 6.2, where the TTR signal model is discussed.

The form of the heat equation implies a particular solution of

$$T(\mathbf{r},t) = \frac{Q}{8c_v(\pi\alpha t)^{3/2}} e^{\frac{-r^2}{4\alpha t}}. \tag{2.11}$$

The total energy would be $\int_{-\infty}^{\infty} c_v T(\mathbf{r},t)\mathrm{d}^3 r$, and at any time $t > 0$, the result is the constant Q. Also, (2.11) is zero at $t = 0$, except at the origin, where it diverges. Equation (2.11) therefore defines the impulse response to instantaneous heating at the origin $\psi(\mathbf{r},t) = Q\delta(\mathbf{r})\delta(t)$ of energy Q, in a solid of diffusivity α and specific heat c_v. Now for periodic heating of power amplitude A, we have $\psi(\mathbf{r},t) = Re\{A\delta(\mathbf{r})e^{i\omega t}\} = A\delta(\mathbf{r})\int_{-\infty}^{\infty} e^{i\omega t'}\delta(t'-t)\mathrm{d}t'$ (real parts are understood from here on). This is an integration over time of impulsive inputs with weights $e^{i\omega t}$, so for this LTI thermal system, the resulting output temperature becomes the time integral of the likewise weighted impulse solution (2.11) - with A replacing Q, since we're now integrating over time. For a steady-state response at time t, the integration is taken from $t' = -\infty$ to t:

$$T(\mathbf{r},t) = \frac{A}{8(\pi\alpha)^{3/2}} \int_{-\infty}^{t} e^{i\omega t'} \frac{e^{-\frac{r^2}{4\alpha(t-t')}}}{(t-t')^{3/2}} \mathrm{d}t' = A\frac{e^{-qr}}{4\pi kr} e^{i\omega t}, \tag{2.12}$$

where $q^2 = \frac{i\omega}{\alpha}$. Equation (2.12) is the steady-state temperature due to periodic heating at the origin.

For the isotropic, spherical geometry, the steady-state heat equation for a periodic source can be solved directly. Solutions are of the form $T'(r,t) = T(r)e^{i\omega t}$, and with the substitution $F(r) = rT(r)$, the heat equation becomes

$$\frac{\mathrm{d}^2F(r)}{\mathrm{d}r^2} - q^2F(r) = 0, \tag{2.13}$$

with general solution

$$F(r) = c^-e^{qr} + c^+e^{-qr}. \tag{2.14}$$

In chapters 5 and 6 we will apply the planar and spherical steady-state solutions to the multilayer geometries used in these experiments, and derive the TTR signals we need for comparison with experimental data.

2.4 Applicable boundary conditions

Although thermal boundary resistance R is the primary nanoscale thermal property of interest in these studies, its definition is independent of scale. In the continuum transport picture, thermal flux is driven by a temperature gradient, so for a boundary at x_0 between materials 1 and 2, as shown in figure 2.2, a finite boundary conductivity $G = \frac{1}{R}$ allows flux for a given discontinuity of temperature by:

$$f(x_0^-,t) = G(T_1(x_0^-,t) - T_2(x_0^+,t)) = \frac{1}{R}(T_1(x_0^-,t) - T_2(x_0^+,t)), \text{ and} \tag{2.15}$$

$$T_2(x_0^+,t) - T_1(x_0^-,t) = k_1R\frac{\partial T(x_0^-,t)}{\partial x}. \tag{2.16}$$

Fourier's law at point x_0^- has been used in the last step. Equation (2.16) also implies that temperatures are continuous at a boundary where $R = 0$.

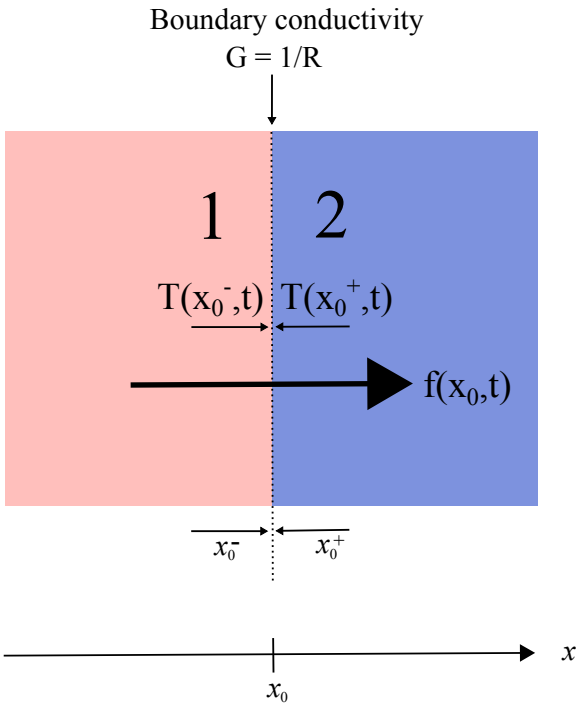

Figure 2.2: Quantities involved in the definition of thermal boundary resistance.

Surface heating is represented as a discontinuity of flux, when crossing the surface. For a surface located at x_0, heating of strength A_0 in the x direction induces the discontinuity

$$f_2(x_0^+) - f_1(x_0^-) = q, \text{ and} \tag{2.17}$$

$$k_2 \frac{\partial T(x_0^+, t)}{\partial x} - k_1 \frac{\partial T(x_0^-, t)}{\partial x} = -q, \tag{2.18}$$

showing that temperature derivatives are related by the ratio of conductivities in the absence of surface heating. These two boundary conditions will be used to both solve for the temperatures resulting from heating, and to construct the multilayer models we require.

2.5 Conclusions

We have developed pictures of how thermal transport happens in the systems of these studies, and clarified some assumptions on which we rely. The steady-state heat equations and their boundary conditions now provide a platform for developing a multilayer model of our experimental structures, and show how TBR is included in the thermal models of these structures. We now turn to considerations of transport that are special to the nanoscale regime.

Chapter 3

Nanoscale Thermal Transport

In section 2.1, macroscopic thermal transport was shown to arise from the underlying diffusive transport picture, with phonons moving randomly in three dimensions, and characteristic mean free paths and relaxation times for a given medium. The validity of the heat equation, as the means of predicting system temperatures from given heating, relies on the assumption that the system's overall scale is much greater than the largest mean free path of its materials. In these experiments, the greatest mean free path is that of electrons in gold NPs, and experiments are carried out near room temperature, where the mean free path of gold is approximately 38 nm[4]. Our NPs, with an average radius of 10 nm, are on a small enough scale to be significantly sensitive to nanoscale effects.

A range of such effects is surveyed in Cahill, *Nanoscale Thermal Transport II*, 2014.[5] In addition to ballistic transport and thermal boundary resistance, nanoscale effects also include anisotropy and reduction of conductivity due to surface scattering,[6] where, for example, the conductivity of silicon, in silicon-on-insulator transisitors, is observed to be reduced to about 25 W/m K from its bulk value of 150 W/m K. Boundary resistance along the path from active devices to the environment also plays a significant role in determining peak operating temperatures and long-term reliability. Complex non-equilibrium conditions can exist when fast electrical switching transient signals, on the order of 10 ps, are shorter than the silicon lattice thermal relaxation time.[5] Nanoscale dimensions also affect radiation

transport, where the surprising result of near-field thermal transfer exceeding that of black body transfer has been observed in systems with dimensions less than the thermal radiation wavelength, ~ 10 μm.

In these studies, the most significant effects to consider are the overall scale effect of ballistic transport and the surface effect of boundary resistance, described in the next two sections. Although the thermal transport measurements of these experiments agree well with the diffusive picture of chapter 2, several of the ideas underlying ballistic transport will be involved in our study and measurements of thermal boundary resistance.

3.1 Ballistic transport

3.1.1 Quantum oscillations and crystal structure

The above derivation of the heat equation, based on the simple but effective idea of thermal energy as randomly moving energy units, must be replaced by a far more sophisticated picture and theory of thermal energy in solids in order to predict thermal dynamics at the nanoscale. The nanoparticles of these experiments are primarily composed of gold, and taking this as an example material, the physical picture becomes one in which thermal energy is the vibrational energy of oscillation modes supported by the crystal lattice of gold ions, alongside the kinetic energy of their nearly-free conduction electrons. The new picture is also quantum mechanical, and the combination of the uncertainty principle and phonon and electron identicality imply that phonons populate energies according to Bose-Einstein statistics, while electrons populate by Fermi-Dirac statistics. These distributions depend very differently on temperature, such that as temperatures T increase from absolute zero, the number of phonon modes grows much more rapidly than those of electrons. With more modes available for the storage of thermal energy, metals at room temperature, including

gold, derive nearly all of their heat capacity from phonons, so only the phonon contribution to thermal energy is considered from here on. Electrons are the primary contributors to thermal conduction, however, through their scattering with the lattice vibrations represented by phonons, as discussed in section 3.1.3.

The *lattice structure* of gold is face-centered cubic (fcc), a simple cubic array with an additional lattice site at each face of each cubic element, and with one gold ion located at each site. The atoms located at a site are the *basis* of the material, and though our example of gold has only one gold ion at each site, in general each site may be polyatomic. The lattice structure along with the basis define the material's *crystal structure*. The fcc lattice is a Bravais lattice, whereby the structure, as viewed from a given site, is seen identically from all other sites, *i.e.* there are no variations such as regions of differing site density or dislocations. The entire lattice is defined by the set of lattice vectors, from a single site chosen as an origin, to every other site, and for a Bravais lattice, the set of lattice vectors is spanned by linear combinations, with integer coefficients, of three primitive lattice vectors $\mathbf{a}_i$:

$$\mathbf{a}_1 = \frac{a}{2}(\hat{y} + \hat{z}),\ \mathbf{a}_2 = \frac{a}{2}(\hat{z} + \hat{x}),\ \text{and}\ \mathbf{a}_3 = \frac{a}{2}(\hat{x} + \hat{y}). \tag{3.1}$$

A conventional cell is a region of volume of the lattice which, when translated through a subset of the lattice vectors, reproduces the full lattice, with no voids or overlap. Conventional cells contain more than one lattice site in general, and the natural choice for the fcc lattice is a conventional cell with vertices coinciding with the original simple cubic lattice - this choice implies 4 sites per conventional cell. A gold conventional cell has side length $a = 4.08\text{Å}$, its *lattice parameter*. A *primitive cell* has exactly one site per cell, reproduces the lattice by translation over all lattice vectors, and such a cell defined to contain points at the minimum possible distance from the contained lattice site is a *Wigner-Seitz* primitive cell. The FCC conventional and Wigner-Seitz cells are shown in figure 3.1.[7] The complete

set of lattice vectors $\mathbf{R}$ for cubic finite crystals of volume V and $N_0 = N^3$ atoms are spanned by the primitive vectors with integer coefficients n_i between $\pm\frac{N}{2}$. For example, for a 1 mm^3 volume of gold, $N \approx 4{\cdot}10^6$. Sums over $\mathbf{R}$ appear frequently in solid state physics derivations, such as for the total potential energy of a crystal.

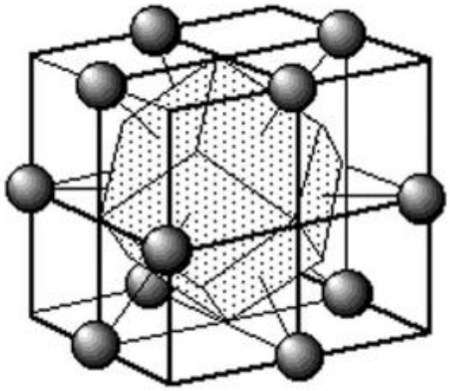

Figure 3.1: The FCC lattice conventional and Wigner-Seitz primitive cells. The smaller cell is the primitive cell. The conventional cell is not coincident with the cubic lattice - instead, the four vertices at half height are four cubic vertices, and the upper half/lower half of the conventional cells below/above the primitive cell are shown. Image from reference 7.

Lattice vibrations, *i.e.* periodic atomic displacements from equilibrium positions, are waves which occupy the space of a crystal (as are conduction electron wave functions (see section 4.2). Such a wave with wave vector $\mathbf{k}$ is represented by a point in *reciprocal space*, and the spatial Fourier transform of the real-space lattice (called the *direct* lattice in this context) is the *reciprocal lattice*. A point in the reciprocal lattice represents a wave with the periodicity of the direct lattice. Reciprocal lattice vectors of increasing length (in reciprocal space) represent waves with increasing numbers of oscillations (in direct space) between adjacent direct lattice points. The fcc reciprocal lattice is a bcc lattice with lattice parameter $\frac{4\pi}{a}$, spanned (with integer coefficients) by the primitive reciprocal vectors $\mathbf{b}_i$:

$$\mathbf{b}_1 = \frac{2\pi}{a}(\hat{y} + \hat{z} - \hat{x}),\ \mathbf{b}_2 = \frac{2\pi}{a}(\hat{z} + \hat{x} - \hat{y}),\ \mathbf{b}_3 = \frac{2\pi}{a}(\hat{x} + \hat{y} - \hat{z}). \tag{3.2}$$

The final construction needed to calculate the phonon energies making up the distribution is that of regions of reciprocal space called *Brillouin zones*. The original measurements of crystal structures were x-ray diffraction (XRD) experiments, in which incident x-ray wave vectors which will produce a diffraction maximum can be predicted as those lying on a Bragg plane, the plane midway between adjacent reciprocal lattice points and normal to the line joining them. The nth Brillouin zone is the region of reciprocal space reached by crossing exactly $n-1$ Bragg planes from the origin - the first Brillouin zone is also the Wigner-Seitz primitive cell of the reciprocal lattice. Section 4.2 discusses how Bragg planes affect the occupation of a material's electronic band structure. In the context of both phonons and electrons, energies in reciprocal space have the periodicity of the reciprocal lattice, due to the original periodicity of the direct lattice. All energies are thus spanned by wave vectors lying in the first Brillouin zone, and plots of representative energies are given in the *reduced-zone scheme* shown in figure 3.3.

The boundaries of the first Brillouin zone of the fcc lattice is shown in figure 3.2.[8] Each face is a region of a Bragg plane lying at the midpoint between the reciprocal lattice site at the zone center and the next-nearest points. The point Γ is at the center of the zone at $\mathbf{k}=0$. The paths Δ, Σ, and Λ are along the lines joining Γ with high-symmetry points X, K, and L respectively, and path Z joins points X and W.

3.1.2 Equilibrium mode distribution

For monatomic gold, each phonon *acoustic mode* is characterized by a wave vector and polarization branch designation as $(\mathbf{k}, j)$. Polarization can be either longitudinal, or one of two transverse, oscillations. (Materials with a basis of more than one atom possess additional *optical modes*.) The finite extent of the lattice is represented by the Born-von Karman periodic boundary conditions, whereby each dimension of the lattice is taken to

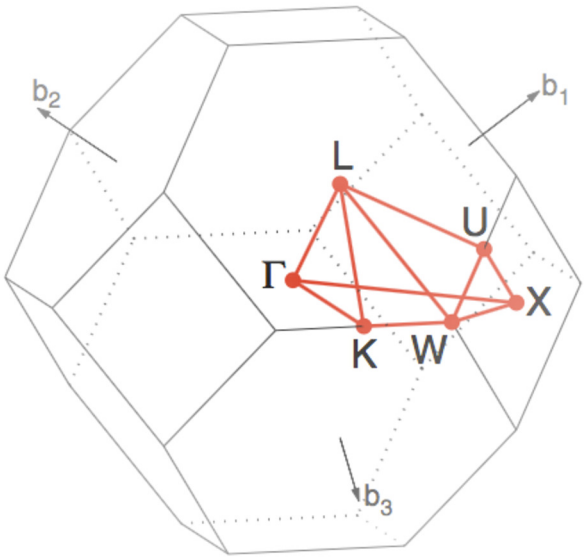

Figure 3.2: The boundary of the first Brillouin zone of the fcc lattice, along with the primitive reciprocal lattice vectors $\mathbf{b}_i$. In this plot [001] is upward, [100] is in the direction from Γ through the center of the left-front square face, and [010] is along the path from Γ to X. Image from reference 8.

loop back upon itself, and the displacement of the final ion in one direction is identical to that of the equivalent atom in the opposite direction. For macroscale crystals, or nanoscale crystals with nevertheless large numbers of atoms, edge effects are significant only for a very small fraction of the atoms, and the Born-von Karman conditions treat the edge effects as negligible. The possible values of k_i are multiples of $2\pi/L$, where L is the material's length in direction i, a near-continuum for a macroscopic system. Each atom oscillates about its stable equilibrium position as a quantum mechanical oscillator, its energy above its ground state is a multiple of $\hbar$ times its oscillation frequency, the single-phonon energy. From this point, if we can relate each mode to its energy, and determine how these modes are populated at equilibrium, then we can then determine what thermal flux would be generated by either a heating input or by a temperature gradient existing in the system, by considering how these excitations affect the distribution of modes.

To relate each mode to its vibration frequency, the lattice energy above the ground state is approximated by the sum of harmonic, *i.e.* quadratic, interatomic potentials, determined by gold's established and experimentally-confirmed elastic constants. Writing Newton's second law for the atomic displacements, and assuming their periodic time dependence, the result is an eigenvalue problem for each polarization, with eigenvalues giving the system's *dispersion relation*, its frequency as a function of wave number and polarization mode, denoted as $\omega(\mathbf{k}, j)$. The dispersion relation for gold is plotted in figure 3.3[9,10]. The lattice structure of the molybdenum films of our thermal isolation platforms is body-centered cubic (bcc), with a lattice parameter of $a = 3.15$Å, and the same method applies to the calculation of the phonon modes of Mo, using its appropriate elastic constants.

We will soon also need the propagation speed of an initial displacement in direction i of characteristic length $2\pi/k_i$, the displacement's *group velocity* $\mathbf{v}(\mathbf{k}, j) = \frac{\partial\omega(\mathbf{k},j)}{\partial\mathbf{k}}$. Dispersion relations calculated using this physical picture agree within a few percent of results from neutron scattering experiments for many materials of interest, including gold. The intervals of energy traversed by each branch of the curves in figure 3.3 define the phonon *band structure* - the equivalent structure for electrons determines the electron interband transition thresholds, relevant to section 4.3.

So if the phonon energy of a mode $(\mathbf{k}, j)$ is $\hbar\omega(\mathbf{k}, j)$, and the distribution among energies is (for bosonic phonons) the Bose-Einstein distribution

$$f_{BE}(E, T) = \frac{1}{e^{-\frac{E}{k_B T}} - 1}, \tag{3.3}$$

where $k_B = 1.38{\cdot}10^{-23}$ J/K is Boltzmann's constant, then the equilibrium mode distribution $\bar{n}(\mathbf{k}, j, T)$ is

$$\bar{n}(\mathbf{k}, j, T) = \frac{1}{e^{-\frac{\hbar\omega(\mathbf{k},j)}{k_B T}} - 1}. \tag{3.4}$$

Section 3.1.3 will apply the equilibrium distribution to the prediction of temperatures in

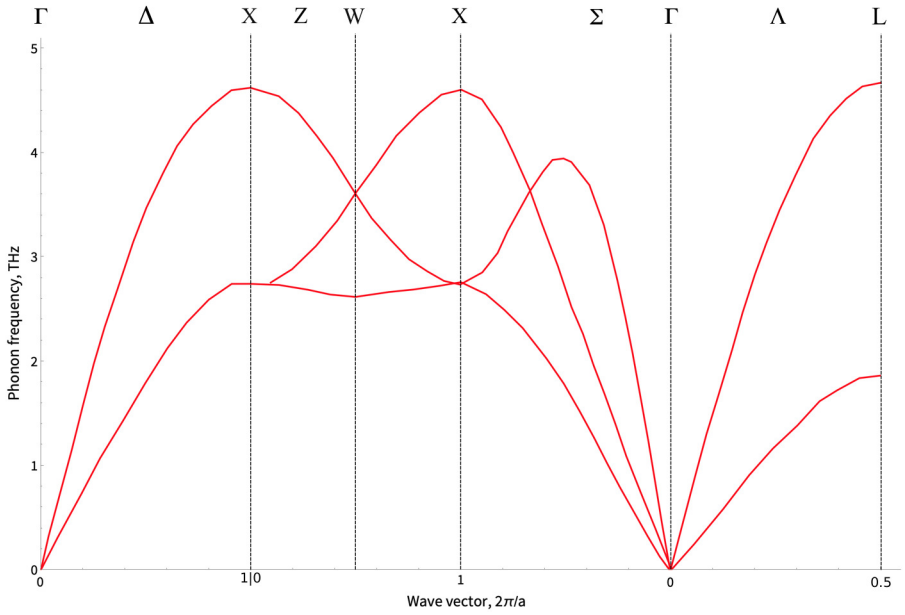

Figure 3.3: The calculated dispersion relation for gold in reciprocal space, at room temperature, plotted along paths joining high-symmetry points as indicated on the upper axis, with reciprocal space distances in fractions of $2\pi/a$. Data from reference 10.

response to excitation by considering the time rate of change of the distribution, expressed by the Boltzmann transport equation.

3.1.3 Ballistic conduction

As a process of thermal transport proceeds, energy is moving from one region to another in a thermal system, and in these TTR experiments, we observe, for example, the cooling of a nanoparticle to its surrounding medium. The energy distribution of the gold NP changes such that the NP contains less net energy as cooling occurs. The specific parameter being monitored is the NP's surface temperature, so if the temperature can be found from the energy distribution, and we can also express and predict how the dynamics of the distribution change during conduction, without assuming that system dimensions are large compared with the phonon mean free path, then we have a nanoscale theory and method for understanding how thermal features of a system affect its response to heating in an experiment such as TTR, and how those features correlate with a measured signal. The differing nature of diffusive versus ballistic conduction is illustrated in figure 3.4. In the diffusive case, with paths small relative to the sphere radius, phonons near the boundary experience net transport across the boundary (black, white, yellow phonons), while those near the nanosphere center remain within the nanosphere (blue, pink, green). In the ballistic case, over the same time period and number of steps, transport not occurring in the diffusive case is possible: the smaller nanopartice radius means that phonons originating near the nanosphere center may cross the boundary (green), those originating outside the boundary can arrive deep within the nanoparticle (blue), and phonons beginning near the boundary can travel a significant fraction of the particle size (pink). The net effect is reduced transport in the ballistic case relative to the diffusive case.

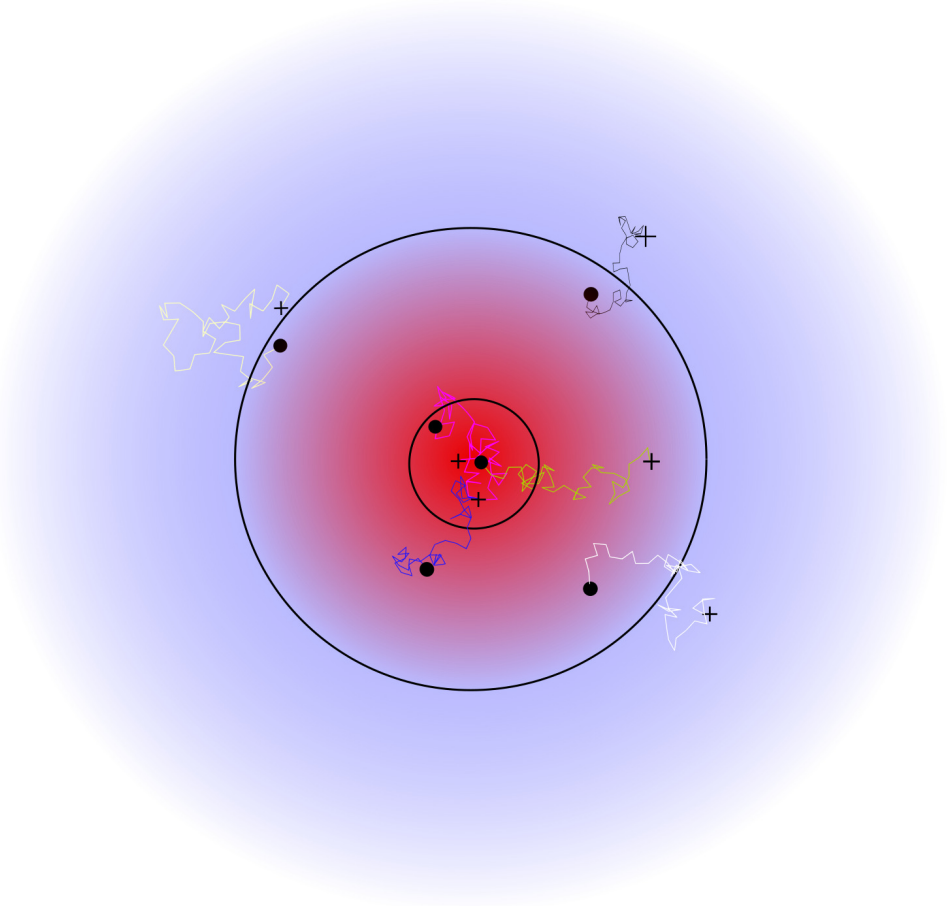

Figure 3.4: Illustration (not to scale) of differing characters of transport between the diffusive (nanosphere boundary represented by the large circle) and the ballistic (small circle) cases. Black dots are phonon beginning positions, and crosses are end points. All illustrated phonons move in random walks of 50 steps, with each step length equal to the phonon mean free path for clarity. See text for additional description.

The key quantity of this strategy is the energy distribution $n(\mathbf{k}, j, T, t)$, now taken as a dynamic, time-dependent quantity. The calculation and experimental verification of these dynamics are challenging areas of ongoing research. Two methods have received attention in recent years: *molecular dynamics* and solutions of the *Boltzmann transport equation* (BTE). Both methods have their own advantages. Molecular dynamics (MD) is a computational method that allows the explicit definitions of structures and interfaces, including roughness and composition, and successfully predicts transport in structures such as superlattices and interfaces. MD simulations solve Newton's second law for individual atoms and molecules using interatomic potential energies, well-known for many materials. Simulations can become computationally difficult for systems which require a large number of atoms for an accurate representation, and its classical basis overpredicts heat flow for materials with high phonon frequencies, such as graphene. Efforts to implement quantum mechanical MD are ongoing.

Let's consider the BTE more closely. In TTR experiments, an object is heated impulsively, and the system relaxes from a non-equilibrium state. BTE analyses begin with the initial non-uniform temperature field $T(\mathbf{r}, t = 0)$, and calculate the resulting flux. As the phonon population for a given mode experiences collisions with other phonons, electrons, grain boundaries and other defects, isotopes, and impurities, an imbalance between the rates of population and depopulation is represented by a 'collision' term in the distribution rate of change. Additionally, since temperatures are non-uniform, and the Bose-Einstein distribution depends on temperature, we would expect the distribution to be non-uniform also, with imbalances in phonon flux leading to a 'drift' term in the BTE:

$$\frac{\partial n(\mathbf{k}, j, \mathbf{r}, t)}{\partial t} = \left.\frac{\partial n(\mathbf{k}, j, \mathbf{r}, t)}{\partial t}\right|_{coll} - \mathbf{v}(\mathbf{k}, j) \cdot \nabla n(\mathbf{k}, j, \mathbf{r}, t), \tag{3.5}$$

the Boltzmann transport equation for phonons[11]. For a TTR experiment involving small temperature changes, the temperature as a function of positon and time could be approx-

imated by using an iterative method, beginning with the initial temperature field and the linearized, time-independent BTE:

$$\frac{\hbar\omega(\mathbf{k},j,\mathbf{r})}{k_B T(\mathbf{r})^2}\bar{n}(\mathbf{k},j,\mathbf{r})(\bar{n}(\mathbf{k},j,\mathbf{r})+1)\mathbf{v}(\mathbf{k},j)\cdot\nabla T(\mathbf{r}) = \left.\frac{\partial n(\mathbf{k},j,\mathbf{r})}{\partial t}\right|_{coll} \tag{3.6}$$

Here we utilize our equilibrium distribution $\bar{n}(\mathbf{k},j,\mathbf{r})$ and the dispersion relation $\omega(\mathbf{k},j,\mathbf{r})$. The collision term includes two contributions: one from phonon-phonon collisions, and another from independent phonon decay:

$$\left.\frac{\partial n(\mathbf{k},j,\mathbf{r})}{\partial t}\right|_{coll} = \sum_{\mathbf{k}'j'} C(\mathbf{k},j,\mathbf{k}',j')n(\mathbf{k}',j',\mathbf{r})\mathrm{d}^3\mathbf{k}' - \frac{n(\mathbf{k},j,\mathbf{r})}{\tau(\mathbf{k},j,\mathbf{r})}. \tag{3.7}$$

The second term, representing the rate of change due to decay and collision processes, is the relaxation time approximation for phonons, whereby phonon dynamics are simplified by assuming that, for a given mode, the distribution rate of change does not depend on the distribution value of other modes, but only on that of the given mode, and that once an equilibrium distribution value for the local temperature $T(\mathbf{r})$ has been reached, the rate of change becomes zero (driving the system to equilibrium). However, the distribution rate of change *does* depend on position through its dependence on temperature, and likewise for the lifetimes, in this approximation. A method for lifetime calculation is given in a classic paper by Maradudin[12], where an interatomic potential model, chosen to agree with experimental values, and crystal thermal expansion properties are used to calculate mode lifetimes.

An important simplification is that the phonon decay and collision rates are proportional to the temperature, for temperatures greater than the Debye temperature $\Theta_D = 170\mathrm{K}$ and less than the melting point $T_m = 1337\mathrm{K}$, as for these experiments, where three-phonon collisions are predominant. A calculation based on a nearest-neighbor central force model for fcc crystals is given by Maradudin and Tamura.[13] For low frequencies and wave vectors, collisions are dominant over decays in the Alkiezer regime[14] where $\omega\bar{\tau} < 1$, where $\bar{\tau}$ is

the mean lifetime, and thermoelastic damping and viscosity effects[15] must be taken into account.

The relaxation time approximation overestimates the effectiveness of phonon decays and collisions in returning a system to equilibrium. The first term in eq. 3.7 involves the *collision kernel* $C(\mathbf{k}, j, \mathbf{k}', j')$, which corrects this overestimate by giving a weight C to the distribution value of each mode $n(\mathbf{k}, j, \mathbf{r})$. Like the lifetimes, the collision kernel can also be calculated by defining an interatomic potential model, including harmonic and anharmonic terms[16].

Ballistic conduction calculations are challenging, and experimental confirmation of some of the approximations mentioned above is not yet available[5]. On the other hand, many of the required parameters are well-known for gold: the dispersion relation, elastic constants, potential energy coefficients to the third degree, and expansion coefficients. Such calculations have been done for silicon, germanium, and diamond[16–18].

A calculation of the ballistic impulse response for the gold NPs of these experiments can be visualized. An NP absorbs energy from an ultrashort pulse, and with gold's conductivity three orders of magnitude greater than that of the surrounding polymer matrix, the NP would be nearly at internal equilibrium relative to the matrix. A reasonable model for the initial temperature distribution would then be a nearly-constant value within the NP, with a sharp downward step of length δr at the NP radius a. With this initial distribution and the above parameters, eq. 3.6 would be solved numerically, with spherical symmetry, yielding $n(\mathbf{k}, j, r, t = 0)$, and the energy flux from[5]

$$j(r, t = 0) = \sum_{\mathbf{k},j} n(\mathbf{k}, j, r, t = 0) v_r(\mathbf{k}, j) \hbar\omega(\mathbf{k}, j), \tag{3.8}$$

where $v_r = |\mathbf{v}|$. The change of temperature ΔT over time t_i could be approximated by dividing the radius into thin shells of thickness $r_s \ll a$, and finding a new temperature

distribution at multiples of r_s, after a short time interval t_i, from the volumetric specific heat c_{pv} by

$$\Delta T(r = nr_s) = \frac{t_i}{c_{pv} r_s} \big[j((n-1)r_s, t=0) - j((n+1)r_s, t=0) \big] \tag{3.9}$$

where n is an integer between 0 and $\frac{a}{r_s}$. The process is then iterated with the shifted temperatures eq. 3.9 substituted into the BTE eq. 3.6, and the process repeated with successively smaller values for δr, r_s and t_i until $T(r,t)$ converges to within an acceptable approximation error.

3.2 Thermal boundary resistance

3.2.1 TBR concepts

When two different materials are in contact, and a temperature gradient is present to drive a thermal flux (power per unit area) across their interface, the thermal resistance of the boundary is defined as the temperature drop, per unit thermal flux, between opposite sides of the interface. It was in 1941 CE that the first measurement of TBR was reported by Kapitza[19] between a bronze wire thermometer and liquid helium.[20] Boundary resistance, defined this way, implies two additional specific points: that incident phonon reflections will occur at the interface, and also that there be a discontinuity of temperature on the opposite sides of the interface. The concept of resistance implies that there is a decrease in potential in the direction of transport - a temperature decrease, in the thermal case - and since we are considering boundary resistance, as opposed to that due to the thickness of a material, the temperature decrease must occur between points immediately adjacent to the boundary, on opposite sides. TBR is not inherently a nano- or atomic-scale property - the acoustic mismatch model (details in subsection 3.2.2) includes macroscale mechanisms of phonon reflection, and its predictions which are accurate in at least some cases. For many

interface pairs, TBR has relatively little effect at the macroscale, since experimental values (see figure 3.6) indicate that typical TBR at interfaces presents the equivalent resistance of a material thickness of well under 1 μm, but in nanoscale devices, TBR can be the controlling factor of thermal transport. So though not *inherently* nanoscale, TBR is of great nanoscale *significance*.

In a microscopic picture of thermal energy and transport, TBR for crystals is suggested intuitively[1] by the fact that the interface interrupts the periodicity of the lattice, and within the phonon mode picture of section 3.1 it is reasonable to suspect that differences in available phonon modes between the two materials could cause phonons to reflect at an interface. At any scale, interface roughness, mixing, disorder, or mismatch of acoustic velocity, or mass density, could cause reflection. Phonon reflection of any sort is a mechanism of thermal resistance, reducing thermal flux and implying a temperature discontinuity at the interface. Some of these ideas are developed theoretically in two different models: in the *acoustic mismatch* model (AMM),[21] phonon transmission probability is calculated from acoustic and mass density properties, while in the *diffuse mismatch* model (DMM),[22] phonons incident on the interface retain no memory of their original direction or polarization, and scatter with probabilities based on their energy densities of states and phonon dispersion.

These two models do not include explicit definitions of interface characteristics, such as morphology, bond strengths, or mixing, instead finding results from bulk properties of the two materials in contact. Molecular dynamics simulations very effectively allow such definitions, however, and agree well with experiments on interfaces between water and self-assembled monolayer silanes.[23,24] Other experiments[23,25] show a relationship of decreased TBR with greater interfacial bond strength. None of the models accurately predict TBR in all experimental cases, but they do give values that are generally useful for comparisons to

experimental results, and are accurate in special cases: the AMM is a good approximation at low temperatures,[5] and it predicts a lower limit of TBR even in the limit of high bond strengths.[26] The DMM predicts that TBR is decreased when the materials' vibrational spectra match, in cases where diffuse scattering is dominant. This effect has also been seen in MD simulations[27] and in experiments with carbon nanotubes in water.[28]

The models differ in their approaches to the calculation of phonon transmission probability. Once transmission probabilities for phonon modes are known, they can be used to calculate the TBR R through its reciprocal, the *thermal boundary conductivity* (TBC) $G = \frac{1}{R}$, defined as the thermal flux across the interface per unit temperature difference. For a given mode, thermal flux is the thermal energy density of the mode times its velocity, so for a rectangular volume V adjacent to the interface, a heuristic total flux incident to the interface is

$$\frac{1}{V} \sum_{\mathbf{k}_{inc},j} \hbar\omega(\mathbf{k},j) f_{BE}(\mathbf{k},j,T) v_z(\mathbf{k},j), \tag{3.10}$$

where $v_z(\mathbf{k},j)$ is the component of velocity along the z-axis, oriented away from the interface, and $\mathbf{k}_{inc}$ indicates summing only over modes with wave vectors directed toward the interface ($k_z < 0$). In section 3.2.3 below, we describe how the TBC can be determined from a derivative of thermal flux with respect to temperature. If each mode transmits with probability $\alpha_{\mathbf{k},j}$, the TBC is the difference in incident transmitted flux induced by a unit temperature change at the interface:

$$G = \frac{1}{R} = \frac{1}{V} \frac{\partial}{\partial T} \sum_{\mathbf{k}_{inc},j} \hbar\omega(\mathbf{k},j) f_{BE}(\mathbf{k},j,T) v_z(\mathbf{k},j) \alpha_{\mathbf{k},j}, \tag{3.11}$$

showing that TBC could, in principle, be calculated from the phonon dispersion (ω and v) along with the transmission probabilities α. More detailed derivations are described in the following sections.

3.2.2 The acoustic mismatch model

The AMM is set in a fully continuum picture - all properties are those of continuous media. TBR arises from differences in the acoustic impedances of the two materials. It approximates transport across an interface by supposing that no diffuse scattering occurs there: all interactions of phonons with the interface are either specular refraction or specular reflection. The AMM also accounts for the possibility of polarization conversion. Cheeke[29] describes the AMM derivation: boundary conditions of continuous stress and strain at the interface (*i.e.* requiring the interface to be fixed) leads to a system of four equations, with unknowns of the ratios of ingoing and outgoing amplitudes as well as outgoing angles, and with normal components of velocities, mass densities, and the angle of incidence as known parameters. The Snell-Descartes relations then allow the system to be solved for the transmission probability as a function of the angle of incidence. TBC of a given interface is calculated in terms of the transmission probability averaged over incoming angles, and Cheeke[29] describes how the averaged transmission can be expressed in terms of the ratios of acoustic velocities and mass densities of the two materials, and found from these ratios using their published tables. We follow this method of calculating TBC with the AMM in section 5.6.

The AMM tends to underestimate the TBC for solid-solid interfaces, especially for similar materials, *i.e.* those with similar Debye temperatures. In order to define a likely range of TBC for a given pair of solids, the *radiation limit* was proposed by Snyder[30] as the upper limit for TBC, assuming that transmission occurs through elastic, two-phonon processes only, and with the AMM prediction as the lower limit. To find the radiation limit, the maximum phonon frequencies are compared - whichever is lower, denoted ω_{max}, becomes the cut-off frequency for phonons from the other material, where transmission is 100% for incident phonons below ω_{max}, and zero above ω_{max}. The measured TBC of many

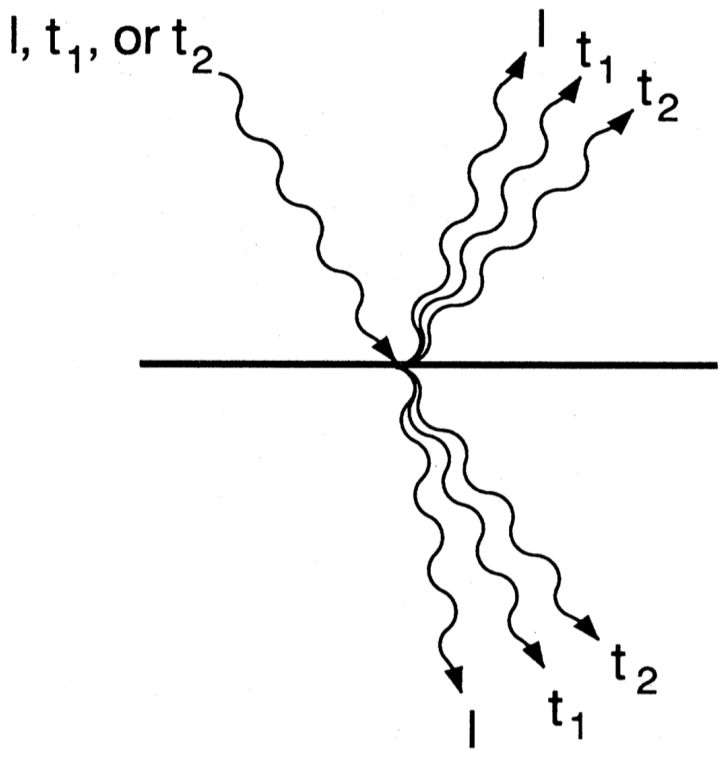

FIG. 12. Schematic of the many possibilities within the framework of the acoustic mismatch model for phonons incident on an interface. The picture simplifies if one of the sides is liquid helium; there are no transverse modes on that side.

Figure 3.5: Illustration from reference 20 of the acoustic mismatch picture of phonon scattering and transmission at the interface between two continuous media. Transmitted phonons refract according to the exact acoustic analog of Snell's law.

materials falls within the range of the AMM value as the lower limit, and the radiation limit as the upper limit. However, the TBC of very dissimilar materials tends to exceed the radiation limit value, motivating the development of the DMM.

3.2.3 The diffuse mismatch model

Figure 3.6[31] plots measured TBC against temperature for interfaces between several pairs of similar and dissimilar materials. The prediction of the DMM for the similar materials of the TiN/MgO interface is the upper dotted curve, and it agrees roughly with experimental values. The lower dotted line is the radiation limit for the dissimilar Bi/H-terminated diamond interface - these experiments show that the TBC is higher than the radiation limit for several interfaces, indicating that inelastic, three-phonon, or diffuse scattering at the interface, or a combination of those, contribute significantly to conduction. Both the AMM and DMM assume equilibrium, while in the experiments described here, measuring the impulse temperature response of structures, will necessarily be non-equilibrium systems. The models still provide useful values for comparison, and the validity of the equilibrium approximation is discussed in the DMM derivation below.

The DMM, though predicting values close to the AMM for similar materials, also improves estimates for dissimilar materials, by predicting TBC for some cases to be greater than the radiation limit. The DMM takes the transmission of an incident phonon to be independent of polarization, and material of origin, but dependent on energy or wave vector, and like the AMM also assumes elastic, two-phonon processes. Since the material of origin does not determine transmission, the sum of transmission from one side and reflection from the other side must be 100%.

Figure 3.7 depicts the behavior of phonons of differing modes/wavelengths arriving at an interface between two materials, with the label 1 assigned to the higher temperature material, and 2 for the lower temperature. Phonons from material 1 (red) can reflect from or transmit through the interface, but with no memory of their original direction, so their outgoing directions are generally altered from their incident directions. The same is true

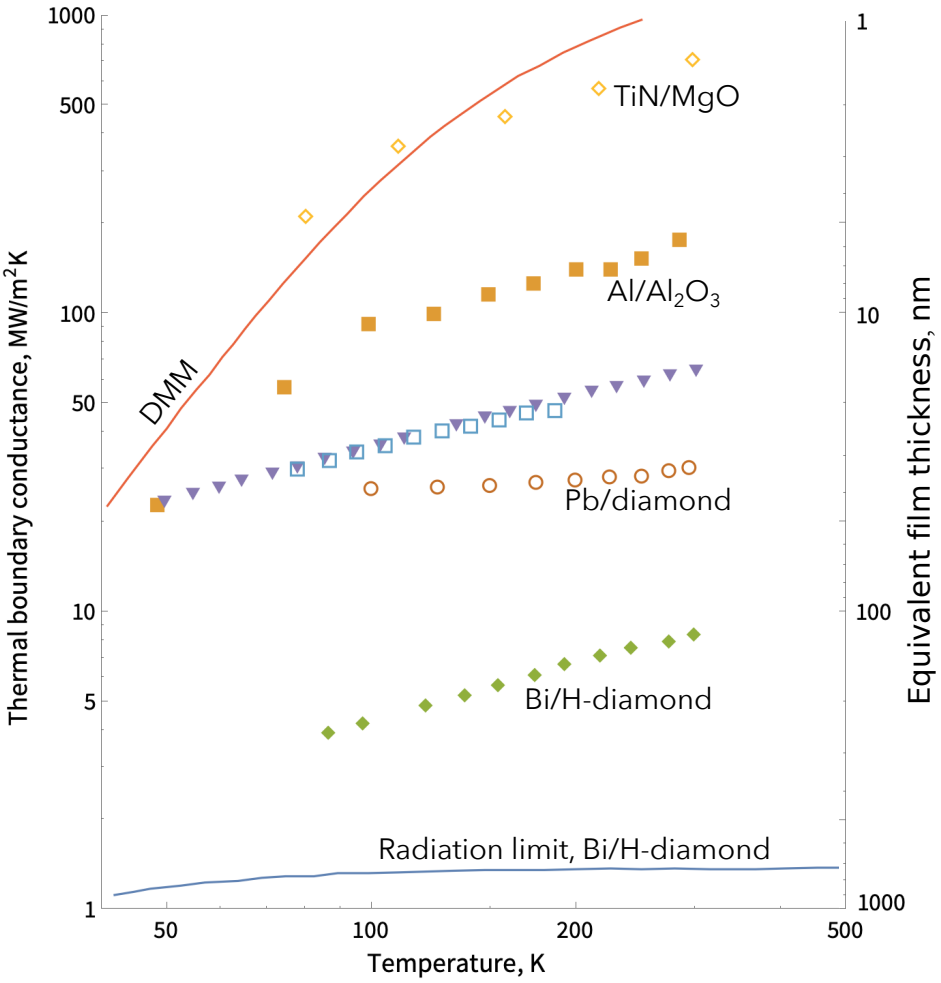

Figure 3.6: A plot from reference 31 of experimental TBC for solid-solid interfaces, with a prediction of the DMM for TiN/MgO TBC, and the radiation limit for Bi/H-terminated diamond. The triangles are for $Ge_2Sb_2Te_5/(ZnS, SiO_2$ composite), and the open squares are for Al/oxide/Si structures.

of phonons originating from material 2 (blue). Though not shown, longitudinal modes are also present.

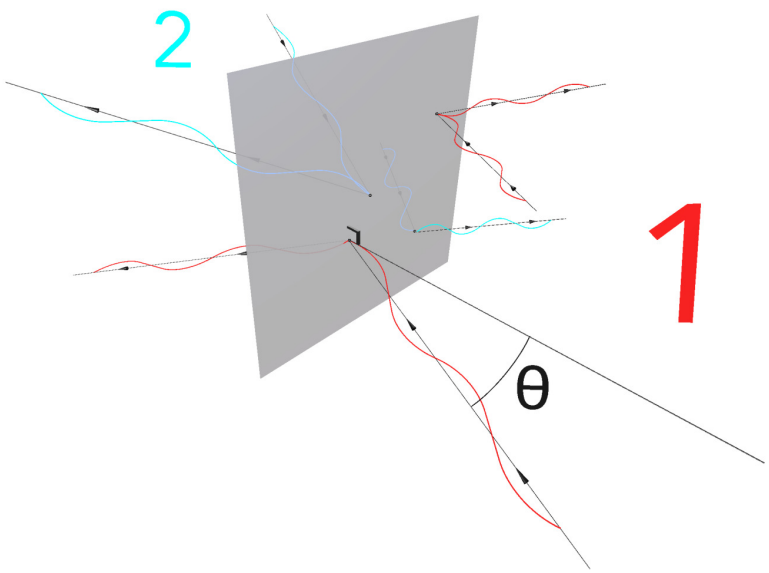

Figure 3.7: Scattering of phonons at a thermal interface in the basic diffuse mismatch model. Phonons originating from material 1 (foreground) are drawn in red, likewise blue for material 2 (background). Phonons can reflect from or transmit through the interface, but with no memory of their original direction, so their outgoing directions are generally altered from their incident directions.

The approach to calculating the TBC is to first express it by its definition in terms of thermal currents, then to replace currents with a sum over phonon modes of their energies, velocities, population, and probability of transmission. To this point, the derivation is identical to that of the AMM. The DMM differs in the calculation of the transmission probability, using the model's above condition that the sum of transmission from one side and reflection from the other side must be 100%. The TBC is then known in terms of the phonon dispersion, for which the Debye approximation is made.

The TBC definition is

$$G = \frac{1}{R} = \frac{\dot{Q}/A}{T_1 - T_2} \tag{3.12}$$

for thermal current $\dot{Q}$ over area A, and temperatures T_i. For practical cases in which a metal or other crystal is in contact with an amorphous material, as it is in our own experiments, the calculation is assisted by expressing, as much as possible, the TBC in terms of properties of the crystal, for which phonon modes may be defined. In fact, this approach can be implemented very well by approximating the system by one in equilibrium, and through conservation of energy. In our experiments, with temperature differences across the interface at 1 K or less, the equilibrium approximation is at least a reasonable initial approach. As described below, the result is that the TBC is expressed in terms of modes and dispersion of the crystal, with dependence on the opposite material entering through the transmission probabilities.

By energy conservation, and with no energy being stored or converted at the interface itself, the current approaching the interface from one side equals that leaving the interface on the opposite side, and the reverse is also true. The net current $\dot{Q}$ is the difference between currents in opposite directions. For a given side, the current approaching the interface originates on the same side, and is at the temperature of that side, unlike the current leaving the interface, part of which originates from the other material at a different temperature. The DMM therefore uses the incident currents initially, so that $\dot{Q} = \dot{Q}_{1,inc}(T_1) - \dot{Q}_{2,inc}(T_2)$, where $\dot{Q}_{1,inc}$ is the incident current from side 1. If material 1 is the crystal, we want expressions in terms of that side, so the net current becomes $\dot{Q} = \dot{Q}_{1,inc}(T_1) - \dot{Q}_{1,dep}(T_2)$ from energy conservation, with $\dot{Q}_{1,dep}$ as the current departing the interface on side 1. Though departing currents are initially not known, with the equilibrium approximation detailed balance requires that departing currents are balanced by incident currents. The

side 2 temperature is retained, so the net current becomes

$$\dot{Q} = \dot{Q}_{1,inc}(T_1) - \dot{Q}_{1,inc}(T_2) \tag{3.13}$$

and the TBC is

$$G = \frac{\dot{Q}_{1,inc}(T_1) - \dot{Q}_{1,inc}(T_2)}{A(T_1 - T_2)} \tag{3.14}$$

which for small temperature differences is

$$G = \frac{\mathrm{d}(\dot{Q}_1(T)/A)}{\mathrm{d}T}. \tag{3.15}$$

The derivation now turns to calculating $\dot{Q}_1(T)/A$. The transmitted phonon energy current density is the product of the phonon energy $\hbar\omega$, spatial density of states per unit frequency n, the Bose occupation factor $f_{BE}(\omega, T)$, the normal component of the phase velocity v_j for polarization j, and the transmission probability α, summed over modes (frequency and polarization). In this simple form of the DMM, the properties of materials are assumed to be isotropic and temperature-independent. The isotropy approximation is relaxed in a study by Duda[32] *et al.* The small temperature differences of our experiments again make this last approximation reasonable. Regarding isotropy, and considering any dependence on direction of the quantities to be integrated over phonon modes, we find that the DMM model of phonon behavior at the interface is that they lose any memory of their incident direction, so the probability α must be independent of initial direction. Expressions for n and v are found from the phonon dispersion. The DMM utilizes the Debye approximation for the dispersion, making both quantities direction-independent, and mode-independent, with the exception of retaining the significant dependence of velocity on polarization. We note that Reddy[33] and Young[34] have studied the effect of exact phonon dispersions on TBC calculations in the case of metal/Ge and metal/Si interfaces, finding that, in the case of interfaces with copper, the models differ by about $\pm 50\%$ of the Debye result. This difference suggests that including phonon dispersion could improve the accuracy of the DMM, possibly

more than removing the equilibrium approximation. The only dependence on incident angle that remains is a cos θ factor for the normal component of phase velocity.

In the Debye approximation, phonons have fixed velocities independent of wave number, and an upper cutoff frequency ω_D. The number of phonon states per unit volume and frequency is

$$n_j(\omega) = \frac{1}{2\pi^2}\frac{\omega^2}{v_j^3}. \tag{3.16}$$

This form of $n_j(\omega)$ is for a single state of polarization j (one longtitudinal and two transverse) - Debye approximations grouping polarizations together have an additional factor of three. The current density per unit solid angle and frequency for polarization j is

$$\frac{1}{4\pi}\alpha\, n_j(\omega) f_{BE}(\omega, T)\, \hbar\omega\, v_j \cos\theta. \tag{3.17}$$

The dependences of α are discussed in the following paragraph. To integrate over all modes, we integrate over frequencies up to the Debye frequency, and sum polarizations, so that the TBC is

$$G = \frac{1}{2}\sum_j v_{1,j}\Gamma_{1,j}\int_0^{\omega_D} \hbar\omega\, n_{1,j}(\omega)\frac{\mathrm{d}f_{BE}(\omega,T)}{\mathrm{d}T}\mathrm{d}\omega, \tag{3.18}$$

where the subscript 1 indicates material 1, and $\Gamma_{1,j}$ is

$$\Gamma_{1,j} = \int_0^{\pi/2} \alpha\cos\theta\sin\theta\,\mathrm{d}\theta, \tag{3.19}$$

and is called the averaged transmission probability: it is the probability averaged over polar angles, but also weighed by the cos θ factor for the normal component of velocity.

Given the approximations of isotropy, equilibrium, and the Debye approximation, eq. 3.18 is applicable to both the DMM and the AMM. Results special to the DMM follow from the following evaluation of the transmission probability α. In general, phonons of a given wave number and polarization have multiple energy values, as shown in figure 3.3, but with the fully diffuse scattering of the DMM and no memory of incident side and direction, the

transmission probability must be independent of wave vector and polarization. Temporarily retaining dependence on energy and frequency, we have the condition $\alpha_{1,j}(\omega, \mathbf{k}) = \alpha_1(\omega)$, and the equivalent for side 2. Most importantly, no memory of incident side means that the transmission probability from one side must equal the reflection probability from the other side, *i.e.* a phonon leaving the interface into a given side must be equally likely to have been reflected from that side or transmitted from the other side, so that $\alpha_1(\omega) = 1 - \alpha_2(\omega)$, and likewise for side 2. Again within the equilibrium approximation and detailed balance, we consider the number of phonons leaving side 1, per unit area, time, and frequency, which must equal the same for side 2. The three polarizations are summed:

$$\sum_j v_{1,j}\, n_{1,j}(\omega)\, f_{BE}(\omega, T)\, \alpha_1(\omega) = \sum_j v_{2,j}\, n_{2,j}(\omega)\, f_{BE}(\omega, T)\, \alpha_2(\omega). \tag{3.20}$$

Finally, the above independence of side memory condition and expressions for densities of states and Bose-Einstein distributions are substituted, resulting in solutions for the transmission probabilities:

$$\alpha_1(\omega) = \alpha_1 = \frac{\sum_j v_{2,j}^{-2}}{\sum_{i,j} v_{i,j}^{-2}}, \tag{3.21}$$

where the sum over i is over sides 1 and 2, and $\Gamma_{i,j} = \Gamma_i = \frac{1}{2}\alpha_i$ ($\Gamma_{i,j}$ is independent of polarization j). With the Debye approximation for the phonon dispersion, we find that the probabilities are independent of frequency. In this implementation of the DMM, the TBC can be calculated from the acoustic velocities and Debye frequencies of the two materials.

We also consider any contribution to interface thermal transport that could be made by electron transmission. In fact, for metal-metal interfaces in general, which can have conductances an order of magnitude higher than our metal/organic case, TTR experiments[35] have found that electron transmission accounts for about 90% of transport. The authors successfully adapt the DMM to electron transmission at an interface.[35] Another study by the same research group[31] conversely shows that, in the case of metal/dielectric interfaces, electron-phonon coupling is minimal, and transport is dominated by phonon

transmission. In this work, TTR measurements of TBC between either Bi, a semimetal, or Pb, a metal, on one side of an interface, and several different dielectrics on the opposite side, reveal TBC values falling within a fairly narrow range. By making this comparison between conduction from a material with a high availability of electrons (Pb) to another with relatively few (Bi), the conclusion is that electron transport does not contribute strongly to metal/dielectric transport. We take this conclusion to also be applicable to our metal/dielectric (gold/organic) experiments.

To close the description of this theory of boundary resistance and the DMM, we consider implications of the several approximations that have been made to this point. Thinking broadly, there are several approximations and assumptions present: the equilibrium and Debye approximations; spatial uniformity, as well as temperature and time independence, of properties; isotropy; elastic scattering; the absence of crystal defects or coating impurities; and the harmonic approximation. Of these, we suggest that the Debye approximation is likely to be the least accurate, and we give the following reasons for retaining it.

The Debye approximation is valid for a material at low temperatures, *i.e.* below the Debye temperature (170 K for Au), a condition not satisfied in our room-temperature experiments. At low temperatures, only modes near the center of the 1st Brillouin zone are excited, and experimental phonon dispersion measurements confirm the validity of the Debye approximation for these modes. At higher temperatures, both the nondispersive assumption of the basic DMM, and the approximated density of states, are inaccurate, and we acknowledge this difficulty. However, as mentioned earlier in the section, the use of exact phonon dispersions in the work of Reddy[33] and others seems very promising: dispersion relations are well-known for gold and other metals, and in their study, the expression for TBC remains primarily in terms of the better-known properties of just one side of the interface (the metal). Also, the TBC can be expressed in a variant form of summing over

wave vectors and polarizations, rather than frequency, which implicitly includes the actual density of states in the result. For our purposes, the problem arises in calculating the last required quantity, the transmission probabilities. In our studies, these would be in terms of the unknown dispersion relation for amorphous citrate, whereas in the work of Reddy, known dispersions are available for the two crystals on both sides of the interface in the cases they consider.

Another published DMM calculation, which has been shown to agree fairly well with experiments on metal/(amorphous) water interfaces, is also initially a good possibility for a more accurate theory: the work of Caplan,[36] utilizing the phonon theory of liquids of Bolmatov,[37] calculates the TBC at the interfaces between Al/water and Au/water, and the results differ from measurements by 18% or less. This method accounts for the fact that transverse modes do indeed propagate in liquids in general (not only longitudinal), if they are above a minimum frequency (the Frenkel frequency). The TBC integration over modes is carried over frequency ranges selected by the polarization of a mode, and also by whether the interface is hydrophobic or hydrophilic. However, upon closer examination of this method, we find that the Debye approximation appears once again. So, although this study does not provide a new method of calculating TBC at a crystalline/amorphous interface, we see that the DMM with the Debye approximation can provide an approximate value in some cases. We therefore move ahead with applying it to our metal/organic case.

The best possibility for improvement of the model for our case would be to use the exact phonon dispersion for gold on one side of the interface, while using the Debye approximation for the amorphous organic side. This would allow a calculation of the transmission probability by equating the phonon number flux on opposite sides, similarly to eq. 3.20. The RHS (amorphous) would be unchanged, while the LHS (metal) would change to an integral over wave numbers throughout the first Brillouin zone. The gradient of the phonon

dispersion would provide the velocity factor. An expression for the phonon dispersion as a function of band and wave number would be needed for the metal. Finding this from the well-known method[38] of solving the system of equations resulting from Newton's second law and the harmonic approximation, with elastic constants as the main inputs, would improve results significantly over the Debye approximation.

3.3 Conclusions

A nanoscale picture of thermal energy and transport, based on the vibrational modes of an atomic lattice structure, has been presented to provide a means of understanding and predicting thermal processes for systems of size smaller than the phonon mean free path. Boundary resistance is the effect of greatest interest in these studies, and the TTR method of measuring it is described in chapter 5. Though a predictive general theory of TBR does not yet exist, relevant features of transport, such as the nature of collisions occurring at an interface and the degree of diffuse scattering, can be applied to problems such as thermal management. We continue with a description of the TTR method.

Chapter 4

Transient Thermoreflectance

4.1 Pump/probe design

Transient thermoreflectance[2,39] is an ultrafast optical experimental method for measuring thermal dynamics of a nanoscale system. Our implementation of TTR applies excitation and measurement pulses to nanostructure samples such that all of the requirements placed on pulse duration, frequency, power, resolution, and delay time between excitation and measurement, as described in section 4.6, are satisfied. The thermal parameters we are interested in are determined by measuring an experimental signal which is sensitive to those parameters,[40,41] and varying their values in a mathematical model until a best fit to the data is found. The quantitative verification of these requirements is discussed in sections 5.4 and 6.3.

Figure 4.1 shows a diagram of our TTR optical layout - this figure is shown again in section 5.4, where it is discussed in greater detail. TTR measures a signal which is a frequency component of the impulse response of the system by impulsively heating the system with a pump pulse, and measuring its response with a probe pulse. The separate pump and probe arms are shown in figure 4.1. The pump pulse heats the system by photoabsorption over a pulse duration that is small fraction of the system's response time, so that the measured signal is not significantly different than the ideal impulse response. Allowing samples

to be excited and measured by a continuous train of pulses makes adjustment and noise reduction efforts much easier, so ideally pump pulses are far enough from each other in time that the response is not significantly affected by the arrival of earlier pulses, requiring that the pulse repetition rate be low enough to allow a repetition period that is long relative to the response time. As described in section 5.4.2, our repetition period meets this condition. As described in section 4.3, each pump pulse should carry sufficient energy so that the fraction absorbed by the target surface increases its temperature by about 1 kelvin.

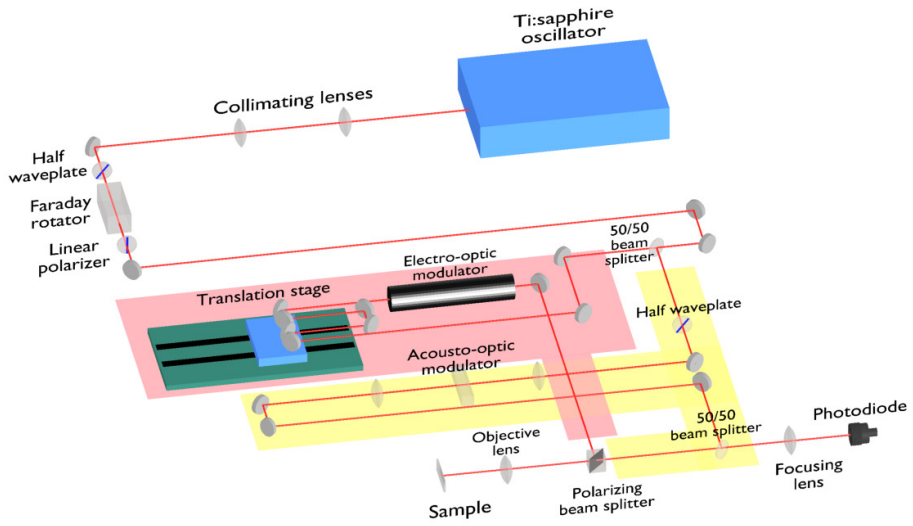

Figure 4.1: TTR optical layout, with pump (pink) and probe (yellow) arms identified. Pump and probe pulse paths rejoin at the polarizing beamsplitter, upstream of the objective lens.

The response of our nanostructures to impulsive heating is measured by monitoring the optical power of the beam of probe pulses reflected from the nanostructure surface. The probe reflected power is proportional to the target's surface temperature, and is sensitive to the values of the thermal parameters we are seeking. The origin of this dependence is discussed in section 4.3. For each data point each must be from a reflected probe pulse sufficiently short that its power is a good approximation of the instantaneous cooling of a target surface, following prior impulsive heating. In our implementation of TTR, pump

and probe pulses split from the same beam and having the same durations satisfy these requirements.

A natural choice for the probe power would be a value which is a small fraction of the pump power, so that the measured value of its reflected power is not significantly different than an ideal measurement which causes no perturbation of the response of the nanostructure. In practice, reducing the probe power this low would result in a signal which can not be distinguished from measurement noise, so the probe power has been set to 50% of the pump for most measurements. However, the detection of the probe signal is locked into a narrow band centered on the modulation frequency of the pump, while the probe beam is modulated at a distantly-located frequency. This ensures that probe measurements are only sensitive to temperature changes caused in targets by the pump pulse train, as opposed to a response to an original component of the probe pulse train itself. Probe pulse powers near this 50% (relative to the pump power) value are typical of TTR experiments.

4.2 Electron band structure

As discussed in section 3.1, the theory of phonon ballistic transport relied on the phonon energy band structure as an essential quantity. Similarly, an understanding of why and how optical reflection properties (of gold in our case) depend on temperature, enabling the mechanism of thermoreflectance to serve as a nanoscale temperature measurement, requires knowledge of the electron energy band structure of gold. The essential picture of electrons in a metal is that of their nearly-free motion in a weak periodic potential due to the atoms of the metallic crystal. Similarities with the phonon case then arise. An electron state is characterized in part by a wave vector $\mathbf{k}$, and while there are no vibration modes to consider, the two values of electron spin each denote a distinct state. The direct lattice periodicity and extent again determine the same possible values of $\mathbf{k}$ as in the phonon case.

A non-relativistic, time-independent equation of motion (Schrödinger equation instead of Newton's second law), employing an interatomic potential with coefficients that decrease with increasing order, predicts energies which agree well with measurements. Energies are again represented in reciprocal space, divided into the same Brillouin zones, which take on additional importance in the electron case. Energies again resolve into bands which may or may not overlap in general.

For the case of the electron energies of gold, with atomic number 79, 54 electrons of the filled $5p$ shell of xenon, and below, are tightly bound to each nucleus, and are considered to remain fixed at each lattice site. Fourteen electrons of the $4f$ shell, though at the next higher single-atom energy, are likewise bound, leaving ten $5d$ and one $6s$ electron per atom which are termed *conduction electrons*. Those of $4f$ energies and below are *core electrons*. The atomic nuclei and core electrons together make up the positive *ions* of the lattice, the matrix in which the motion of conduction electrons takes place. Accurate energies of the $5d$ shell are calculated using the *tight-binding* method, while the 6s electron energies are found through the *nearly-free electron* approximation. The results of both methods are relevant to the transitions involved in the mechanism of thermoreflectance.

Both methods account for the finite extent of a crystal via the Born-von Karman boundary conditions. Each ion is taken to have the same interatomic potential, and electron wave function periodicity is established by Bloch's theorem, which requires that the wave function has the form of a plane wave times another function $u_{n\mathbf{k}}(\mathbf{r})$ which has the periodicity of the lattice:

$$\psi_{n\mathbf{k}}(\mathbf{r}) = e^{i\mathbf{k}\cdot\mathbf{r}} u_{n\mathbf{k}}(\mathbf{r}), \tag{4.1}$$

which also implies

$$\psi_{n\mathbf{k}}(\mathbf{r}+\mathbf{R}) = e^{i\mathbf{k}\cdot\mathbf{R}} \psi_{n\mathbf{k}}(\mathbf{r}), \tag{4.2}$$

i.e. wave functions change only by the phase $\mathbf{k}\cdot\mathbf{R}$ between primitive cells. The symbol n

is the *band index*. The Bloch and Born-von Karman conditions together lead to the same wave vector values $\mathbf{k}$ as for phonons.

For the d-shell energies, the tight-binding method considers a given electron to be mobile throughout the crystal, and equally likely to be found at any lattice site, but to have a probability density centered around the ions (unlike the nearly-free electron approximation, which represents them as modified traveling plane waves). Its wave function is expanded as a linear combination of (isolated) atomic orbitals (abbreviated as LCAO), with modification due to the proximity of neighboring ions, if its isolated wave function has a spatial extent comparable to the lattice constant. The form of the wave function in Bloch's theorem is not used explicitly in the tight-binding method, though the allowed wave vector values $\mathbf{k}$ are found from it. Coefficients and associated energies are found by solving the eigenvalue problem of a two-dimensional square matrix, with each dimension length equal to the number of degenerate isolated atom energies, *i.e.* five for the d-shell. The matrix is the operator for the difference of the actual interatomic potential from the isolated-atom (Coulomb potential) case, in the isolated atom wave function basis.

Applied to the fcc lattice of gold, the tight-binding method yields a relation $\mathcal{E}_n(\mathbf{k})$ for the d-shell energies in which the originally degenerate, discrete levels are broadened into finite bands, and partially split, but continue to lie close to each other relative to the s-shell levels, as shown in figure 4.2[42]. The energy scale is plotted relative to the *Fermi energy*, the highest energy occupied by free electrons for a solid at zero temperature. At room temperature, a small fraction of the electron population occupies energies above the Fermi energy. The energies spanned by curves lying fully below (not crossing) the Fermi energy span the gold d-band.

For the s-band, the nearly-free electron approximation takes the wave function form of Bloch's theorem, expands a known interatomic potential in terms of plane waves $e^{i\mathbf{K}\cdot\mathbf{r}}$ with

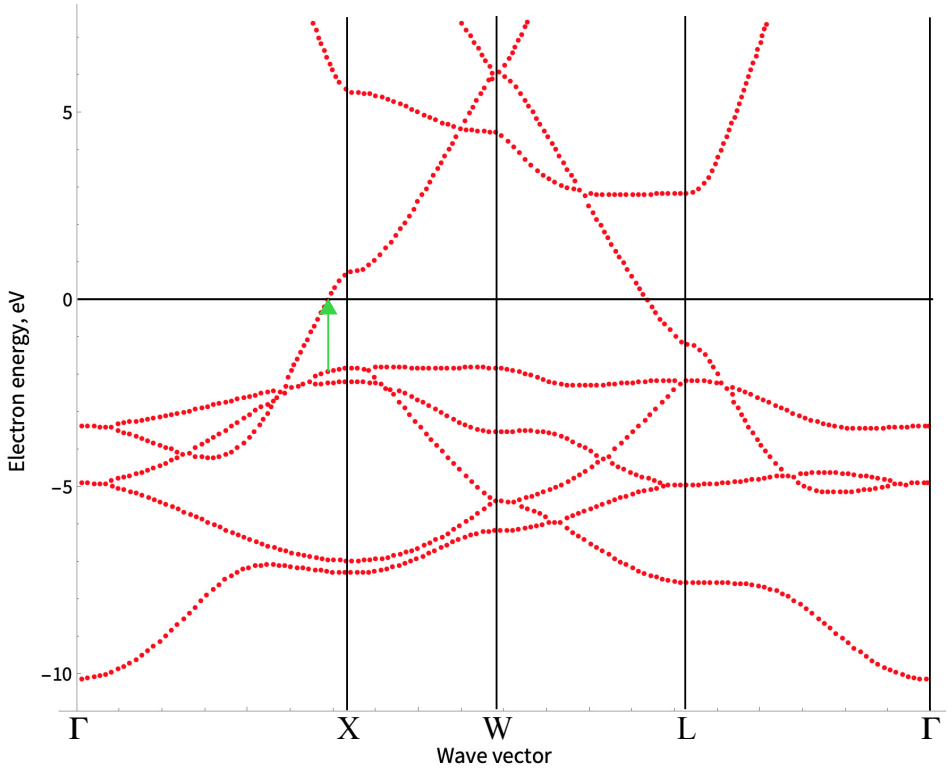

Figure 4.2: The electron band structure of gold, calculated using many-body perturbation theory, from reference 42. Energies are plotted relative to the Fermi energy. Note the overlap in energy, characteristic of conductors, of the full (below the Fermi level) d-bands and the partially filled or empty (spanning or above the Fermi level) s-band curves.[42] The green arrow indicates the energy of the interband transition threshold, about 2.5 eV.

the periodicity of the direct lattice, and substitutes these into the Schrödinger equation. The result is a reciprocal space Schrödinger equation in terms of $\mathbf{k}$ and the potential Fourier coefficients $U_{\mathbf{k}}$. The nearly-free approximation takes the electron wave functions to be perturbations of free-electron waves due to the weak potential of the lattice, such that keeping only first-order terms in $U_{\mathbf{k}}$ is justified. As a result, only degenerate energies located near a Bragg plane contribute a significant term to the perturbed energies. Since the electron wave functions and energies are both periodic in reciprocal space, the effect of the weak periodic potential can be characterized by its shifting of energies as $\mathbf{k}$ approaches

the first Brillouin zone boundary.[38] Figure 4.2 shows the effect of the lattice potential as an increased curvature of $\mathcal{E}_n(\mathbf{k})$, for a given n, as $\mathbf{k}$ approaches one of the high-symmetry points X, W and L.

With the nearly-free electron and tight-binding models providing an accurate band structure $\mathcal{E}_n(\mathbf{k})$, the equilibrium electron distribution $g_n^0(\mathbf{r},\mathbf{k})$ over $\mathbf{k}$ for band n is

$$g_n^0(\mathbf{r},\mathbf{k}) = \frac{1}{e^{\frac{\mathcal{E}_n(\mathbf{k})-\mu(\mathbf{r})}{k_B T(\mathbf{r})}} + 1}. \tag{4.3}$$

Shifts in this distribution with temperature are the origin of the property of thermoreflectance, discussed in section 4.3.

4.3 Thermoreflectance properties

A TTR experiment, prepared with its excitation and measurement pulses appropriate to the length and time scales of the thermal properties being studied, acquires its capacity to measure temperature through the mechanism of thermoreflectance. Thermoreflectance relates the optical power reflected from a surface to its temperature, and for the small temperature changes of about 1 kelvin in these experiments, the relation is nearly a direct proportionality[43], with the magnitude and sign of the proportionality constant, the *thermoreflectance coefficient*, generally depending on material and wavelength. The thermoreflectance is defined as the fractional change in reflectance per unit temperature increase.

The coefficient of reflection, of a paramagnetic surface, for incident radiation of frequency ω depends, weakly, through its refractive index, on its *dielectric function* $\epsilon(\omega)$, or $\epsilon(\lambda)$ with wavelength λ. For a classical electromagnetic wave of frequency ω at normal incidence on a surface from vacuum, the reflectance R, the ratio of reflected to incident

optical power, is

$$R = \left| \frac{1 - \tilde{n}}{1 + \tilde{n}} \right|^2, \tag{4.4}$$

with the complex refractive index $\tilde{n}$ related to the dielectric function by $\tilde{n}^2 = \epsilon(\omega)$.

The width of the step of the electron Fermi-Dirac distribution increases with temperature, so that fewer states above the Fermi level are available for absorption, and vice-versa. The phonon population also increases with temperature, such that increased electron-phonon scattering decreases the electron relaxation time. In fact, at room temperature, scattering of electrons by phonons predominates over that by impurities, isotopes, and other electrons. At time scales longer than those involved in our experiments, thermal expansion also affects the dielectric function through additional shifts in the electron band structure due to the resulting increase of lattice spacing.

The thermoreflectance coefficient for gold is measured by spectroscopic ellipsometry by Wilson[44], and has a value of $-3.25 \cdot 10^{-5}\mathrm{K}^{-1}$, at 800 nm, as shown in figure 4.3. Its negative value is due to increased scattering of photon-absorbing electrons by lattice phonons, due to the increase of phonon population with temperature. Electron-phonon scattering transfers optical energy to lattice vibrational energy, increasing absorption and decreasing reflectance. Our experiment uses a probe beam of wavelength 800 nm, with photon energies of 1.55 eV, significantly below the $5d$ to $6s$ interband transition threshold (see section 3.1) of gold at 494 nm (2.54 eV). The interband transition threshold value is revealed in figure 4.2, as the minimum energy difference between an unoccupied state (above the Fermi energy) and an occupied state (below), occurring for $\mathbf{k}$ slightly less than its value at high symmetry point X. The thermoreflectance of molybdenum is $5.80 \cdot 10^{-4}\mathrm{K}^{-1}$ [44], and is shown in figure 4.4, at photon energy 1.55 eV.

4.4 Time-resolved measurements with pulsed laser excitation

TTR experiments measure the probe signal as a function of a well-known delay time between the arrival of pump and probe pulses at a sample. The same method of controlling delay time is used in both our NP and thermal isolation platform experiments. Our TTR experiment implements the delay with a fixed optical path for the probe arm of the optical set up, and an adjustable pump arm path length. The pump path is adjusted until the two paths are equal, and the pump path is then incrementally shortened to advance the arrival of the pump pulse at the sample relative to the probe pulse. Our TTR experiment uses a translation stage to shorten four segments of the pump path simultaneously. Constant overlap of the pump and probe spots on samples during stage motion requires careful alignment of the four segments with each other and with the axis of stage motion. Procedures for the equalizing of pump and probe arms and the alignment of pump beams to the stage axis are described in section 5.4.

4.5 Dynamics of ultrafast excitation of metals

As mentioned in section 4.6 below, the thermal response time for the nanostructures of our studies is expected to be on the order of 300 ps or longer. The applied ultrafast excitation pulse duration is on the order of 100-200 fs, about three orders of magnitude faster than the thermal response time, so we justifiably consider the excitation to be impulsive, and presume that the energy of each absorbed optical pulse causes a rise in temperature in the nanostructure material. This picture is correct but simplified - there is actually a structure of energy conversion underlying the pulse absorption process which moves through several stages of time scale, as described in Siemens[46], von der Linde[47], and Hohlfeld[48]. This structure implies a minimum delay time of the probe pulse for which the measured TTR

signal represents a dynamic thermal diffusive or ballistic process, and not an incomplete, different relaxation process occurring on an earlier time scale. This consideration affects the choice of probe delay times for curve fitting and thermal parameter calculation purposes. An overview of associated time scales is shown in figure 4.5.

Ion cores and surrounding conduction electrons are the two candidates, in our model of a gold target nanoparticle, for direct absorption of incident pulse energy. The ions prove to absorb almost none of the incident 1.55 eV photons directly, and the Debye quantum model of harmonic crystals provides a reason. A quantum harmonic model finds the specific heat of a crystal by considering each ion to be a harmonic oscillator, and calculates the specific heat as the temperature derivative of the crystal's energy density, in turn found as an integral, over the first Brillouin zone due to lattice periodicity, of lattice vibrational energies. The Debye model approximates the lattice vibrational band structure as consisting of three non-dispersive modes, with an upper vibration frequency limit, the Debye frequency ω_D, and upper energy limit of $\hbar\omega_D$. ω_D is taken to be the crystal's speed of sound times the radius in reciprocal space of a sphere which encloses a number of wave vectors equal to the density of ions in the crystal, equivalent to the reasonable assertion that the maximum wave vector of a vibration is that of one cycle per lattice spacing. For gold, $\hbar\omega_D$ evaluates to 15 meV as the greatest available vibrational energy, about 1% of the incident photon energy of 1.55 eV. With effectively no energies available for excitation, lattice ions absorb no significant pulse energy directly.

Therefore nearly all of the incident pulse energy which is not reflected or transmitted is absorbed by conduction electrons. Initially polarized, these electrons are excited and dephase over a time scale of $\sim$ 10 fs. Only a small fraction of conduction electrons are within 1.55 eV of the Fermi level and can be excited to an available state, so only these are excited by the pulse directly, up to an optical depth of about 13 nm[49] in the case

of gold. The electron population is now in a non-equilibrium condition, and the excited electrons penetrate ballistically further into the metal, up to about 100 nm[48] for gold, while also thermalizing with the rest of the conduction electrons, over about a 100 fs scale. The two-temperature model of Anisimov[50] now describes the 'hot' electron and phonon populations of the crystal in this state, with different temperatures and specific heats for electrons and the lattice, but with each in thermal equilibrium separately. Ultrafast pump-probe experiments can induce very high hot electron temperatures: Hohlfeld describes 400 nm pump pulses heating electrons to about 2700 K in a 1 μm gold film[48]. After electron-phonon scattering on a scale of $\sim$ 1 ps, the much greater specific heat of the lattice places the final equilibrium temperature closer to the initial lattice temperature. Phonon diffusion proceeds over times of about 10 ps or greater, determined by the thermal conductivities and dimensions of the metal and its matrix or substrate.

In our TTR experiments with both gold nanoparticles and membrane systems, cooling times are observed to be occurring over 100s of ps. Since our models represent cooling due to thermal diffusion, we generally begin fitting TTR signal models to data at 100 ps or later delay time, out to 1500 ps, to avoid fitting models to data that represent non-diffusive electron thermalization and hot electron-phonon scattering processes occurring at short delay times.

4.6 Diffusive transport length and time scales required for sensitivity to thermal boundary resistance measurement

4.6.1 Length and time scales of a nanoparticle system

With a primary goal of measuring the TBR of the Au/polymer interface of gold nanoparticles, the TTR experiment must be applied to an NP system in which the TBR is the controlling channel of transport, so that changes (by say 10%) produce a significant

and measureable change in the measured signal, which in our case is the mean power of the beam reflected from NP surfaces, and is proportional to NP surface temperature (see section 4.3). As mentioned in section 3.1.3, gold NPs come to internal equilibrium rapidly, relative to the system response time. For this type of system, Ge *et al.*[40] estimate a critical value of the TBR for a spherical NP, above which TBR becomes the controlling channel, by equating the response times for two systems: an NP of zero TBR, where transport is controlled by the conductivity of the surrounding matrix, and a finite TBR NP surrounded by a perfectly conducting matrix. Effectively, the TBR of the second case is increased until the response time equals that of the zero TBR case. For the zero TBR case, the response time τ_d is found by equating the heat capacity of the NP with that of a surrounding layer of the matrix, with a thickness equal to a matrix 1D diffusion length $d = \sqrt{\alpha\,\tau_d}$:

$$\tau_d = \frac{r^2 c_{vNP}^2}{9 c_{vm} k_m}, \tag{4.5}$$

with NP radius r, volumetric specific heat c_{vNP}, matrix volumetric specific heat c_{vm}, matrix conductivity k_m, and diffusivity α related to the specific heat and conductivity by $c_m \alpha = k_m$. For the TBR case, the heat capacity of the NP is equated to the TBC times the response time, giving response time

$$\tau_i = \frac{r c_{vNP} R}{3}. \tag{4.6}$$

Equating the two times gives the critical TBR value

$$R_{crit} = \frac{r c_{vNP}}{3 c_{vm} k_m}. \tag{4.7}$$

Equation 4.7 indicates that the minimum value of TBR for TBR-controlled transport decreases with the NP radius. Well-known fabrication methods exist for NPs of radius in the 10s of nm, as discussed in detail in section 5.4, and NPs of mean radius of 10 nm were selected for the experiment. Gold and the polymer matrix are very dissimilar materials, with significantly different bond types, strengths, and Debye temperatures, so a low value

of TBC may be expected, perhaps near values for the dissimilar metal/diamond materials in figure 3.6, about 20 MW/m^{2}K. Evaluating eq. 4.7 with literature values for the specific heat of gold, and estimated values of specific heat and conductivity for the polymer matrix, we find $\frac{1}{R_{crit}} = 28$ MW/m^{2}K, near the above Pb/diamond results. MD Si/polymer TBC simulations[51] estimate a value of 17.5 MW/m^{2}K, so we expect that our choice of matrix material and NP radius will likely be sensitive to the TBR value.

As an estimation of the impulse response time of NPs, the R_{crit} value above gives a response time of $\sim$ 300ps, so the time-resolved method of TTR must have data points spaced in time sufficiently closely to resolve this cooling time, thereby minimizing uncertainty in fitting parameters. It must also generate heating in a small fraction of this time so that the NP response is not significantly different than the impulse response. These considerations will be evaluated in section 5.4.

4.6.2 Length and time scales of a membrane system

As mentioned in section 1.1, these experiments test thermal transport assumptions which are relied on in TTR studies, by measuring the TTR reponse of a metal/insulating membrane structure. The *thermal isolation platform* structure we studied was a molybdenum film of 200 nm thickness, thermally deposited on an insulating silicon-nitride membrane. The impulse response time of this system is that of the diffusive transport channel of excited phonons from near the upper Mo surface, where optical absorption takes place within a thin optical penetration depth of 5.5 nm[52] (at the 800 nm wavelength of heating pulses used in these experiments) from the upper surface, to the opposite side of the Mo film. Again applying the 1D diffusion formula $t = d^2/\alpha$ as an estimate of diffusion time, using bulk values for Mo cross-plane conductivity and specific heat, we find that phonons diffuse 200 nm in about 1900 ps. The TTR experiment must be able to measure temper-

ature changes over this time in order to provide data for a thermal tranport model which tests the assumptions in question.

4.7 Conclusions

TTR experiments combine short pulse durations, pump/probe measurement with controlled delay times, sensitive lock-in measurement, and the thermoreflectance mechanism itself, described by electron band structure theory, to produce an apparatus able to measure the thermal responses of a nanostructure on a picosecond time scale. An understanding of the ultrafast excitation of metals allows appropriate delay times to be selected for measurement of thermal parameters by fitting models to data. The next chapters are detailed descriptions of the TTR experiments with two different types of interesting nanostructures.

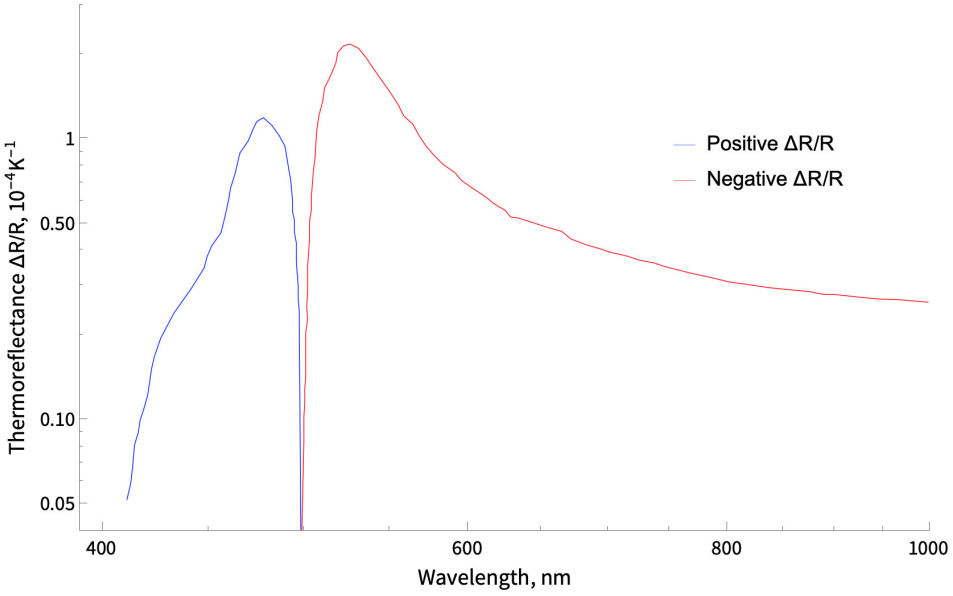

Figure 4.3: The thermoreflectance coefficient of Au against wavelength, given in reference 44. The probe wavelength used in our implementation of TTR is 800 nm.

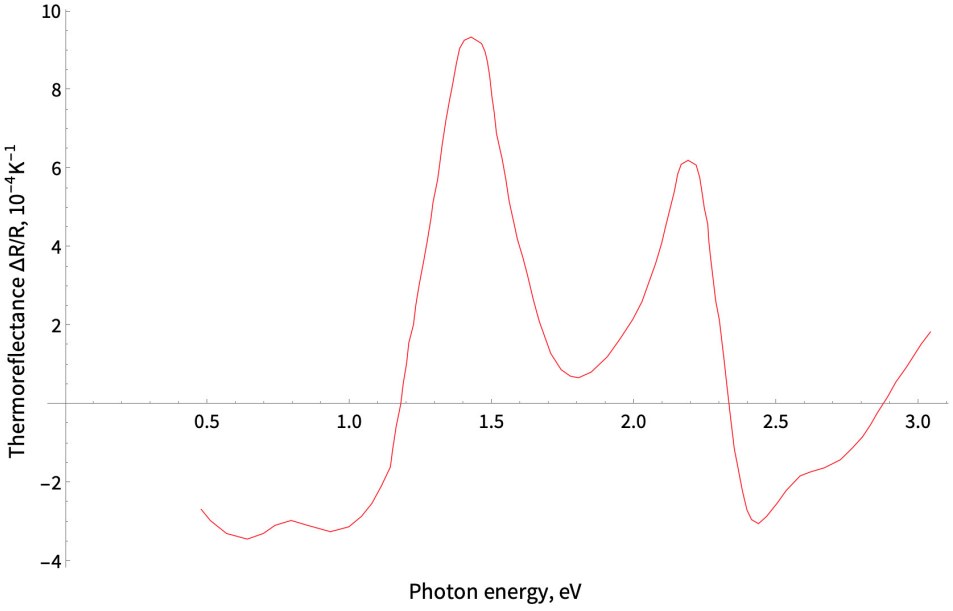

Figure 4.4: The thermoreflectance coefficient of Mo against photon energy, given in reference 45. The photon energy of our implementation of TTR is 1.55 eV, with a thermoreflectance value of $5.80 \cdot 10^{-4}\mathrm{K}^{-1}$.

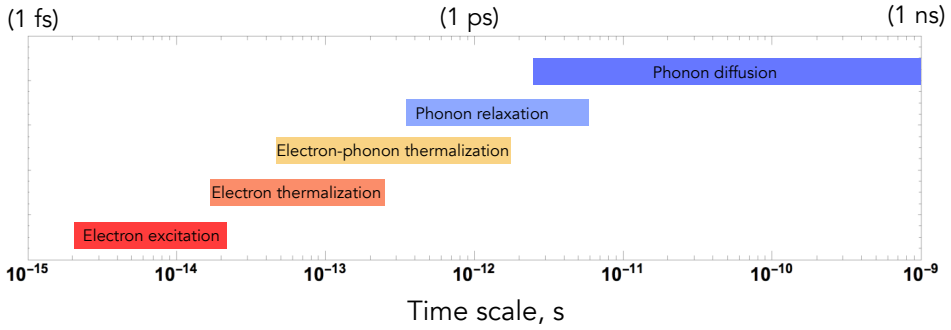

Figure 4.5: Time scales involved in the ultrafast excitation of metals, showing stages of evolution in overall energy transfer from incident photon energy to diffusing phonon energy.

Chapter 5

Nanoparticle Systems

5.1 Introduction

Nanotechnological materials are being studied and produced in diverse forms, including nanostructured materials (e.g. corrosion-resistant nanocomposites), nanoscale devices (e.g. microcircuits), and nanoparticles. In the case of nanoparticles, fabrication methods and optical property tuning have been well-studied. The predictive power of theoretical methods has been confirmed: for the case of spherical particles, Mie theory is an accurate analytical method, while finite-difference time-domain (FDTD, see chapter 7) simulations perform well as a numerical analysis method, and as one which is not restricted to spherical particles.

Combining absorption spectrum tunability and nanoscale dimensions, nanoparticles have generated interest for their use as nanoscale thermal sources.[5] For example, nanothermal phototherapy,[53] the ablation of vascularized tumors by the thermal energy of irradiated NPs, is possibly such a use, and is being actively studied as a potential medical application.[54] However, while potentially relied on to raise biological temperatures, as well as in other applications, the thermal transport properties of NPs have been the subject of relatively few studies,[41] including the property of thermal boundary resistance. The scale on the right of figure 3.6[31] is the equivalent thickness, of a material of 1 W/mK conduc-

tivity, to a TBC value on the opposite scale, illustrating that the TBR for typical metals such as aluminum and gold, in contact with oxides, can have a resistance equivalent to a material layer with thickness on the order of 10 nm, the scale of a nanoscale device. In this chapter we describe the application of the method of ultrafast transient thermoreflectance, which resolves thermal dynamics[55] in response to impulsive heating, to a system of gold NPs embedded in a polymer matrix, allowing the calculation of thermal properties, including TBR. We find that TBR is a significant controller of transport in this system, with a high value relative to that measured in other studies of metallic particles in contact with insulators.

Calculations of the TTR response, often carried out in the frequency domain, require a thermal model giving amplitude and phase values of the particle surface temperature. Suitable multilayer planar models for this purpose are common,[2] but are not relevant to studies of the cooling of spherical NPs. Existing spherical models,[40,56] though inclusive of the TBR property, do not represent stratified particle structures, as is the case when capping layers are present, or in core-shell NP geometries. We therefore have developed a multilayer, spherical model of thermal transport, and apply it to the calculation of the signal expected in TTR experiments. Our multilayer model enables us to explicitly separate the effect on measurements of nanoparticle structural layers, typically capping layers (as in our study) or those in core/shell geometries, which would otherwise mimic or contribute to an apparent TBR effect.

5.2 Existing studies of metallic nanoparticle thermal boundary resistance

Several distinct types of physical phenomena in NPs have been studied using TTR, including electron and phonon dynamics,[57,58] acoustic behavior,[59,60] plasmon resonance,[61]

optical absorption and scattering,[62] and thermal properties.[40,41,55,56,63,64] Important modeling methods include molecular dynamics,[65] finite-difference time domain simulation,[66] and classical electromagnetism,[67–72] including Mie theory.[73–77] Among experiments that have examined NP thermal dynamics, some have included thermal boundary resistance as a parameter, in terms of its reciprocal thermal boundary conductance. These experiments used colloidal, thiol-capped Au and Au/Pd alloy NPs in toluene,[40,64] and Au NPs embedded in glass.[56] For the colloidal NP measurements of TBR, these studies use a frequency-domain solution of the heat equation with TBR as an explicit parameter, but the model does not include any effect of the capping layers, so results could be dependent on the capping layer present. In order to differentiate the effects of TBR and any capping layers, we have developed the following multilayer model for the measured signal in TTR studies, presented in the next section, which represents capping layers and TBR independently, and which we use to fit to measurements and determine experimental TBR values.

5.3 Multilayer spherical diffusion and TTR signal model

The primary inputs to TTR signal model mentioned in section 5.1 are detector responsivity, nanoparticle thermoreflectance, and particle surface temperature. Presuming that the heating strength generated in the particle from optical excitation may be treated as a fitting parameter, we then need a spherical, multilayer thermal model which predicts surface temperature from given heating. General multilayer spherical models exist, but none have been applied to thermal systems with resistance at boundaries, and measured using TTR. Following the matrix formulation approach of Feldman for the propagation of thermal waves in planar stratified media,[78] we develop a spherical wave model by defining a stratified spherical system, as shown in figure 5.1, and solve for the steady-state temperature throughout the system. Individual layers are denoted by the label n, with $n = 1$ for

the material at the center, and $n = N$ for the surrounding matrix. Each layer n ends at radius r_n, and has thermal parameters of diffusivity α_n, volumetric isobaric specific heat c_n, and thermal conductivity $k_n = \alpha_n c_n$.

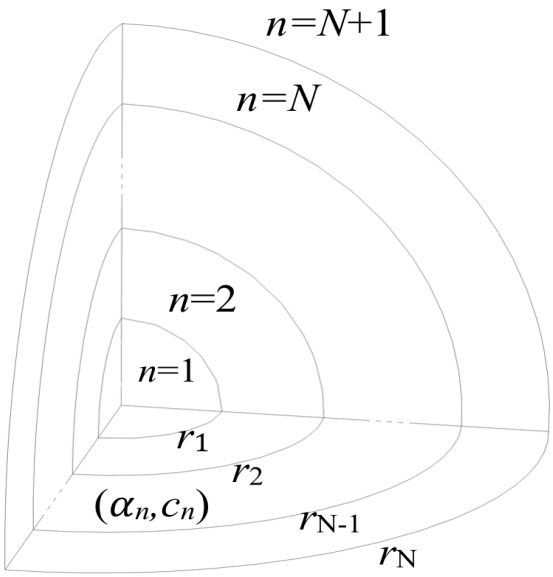

Figure 5.1: The multilayer spherical system, with layer labeling indicated. Each layer has distinct diffusivity α_n, specific heat c_n, and thickness $r_n - r_{n-1}$.

The modulated absorption of optical energy at the surface of a layer is represented by a surface thermal source of strength A_0 as $A_0 e^{i\omega t}$, at frequency ω and time t. $T_n(r)$ is the temperature at radial distance r in a layer n, and the radially-scaled temperature F_n is defined as $F_n(r) = r\ T_n(r)$. Since heat sources are treated as surfaces between layers, diffusion within a uniform, isotropic layer is described by the one-dimensional homogeneous heat equation

$$\frac{d^2 F_n}{dr^2} - q_n^2 F_n = 0, \tag{5.1}$$

with general solution

$$F_n(r) = c_n^-\ e^{q_n r} + c_n^+\ e^{-q_n r}. \tag{5.2}$$

$F_n(r)$ is the temperature distribution within the layer, where the coefficient superscript indicates the direction of wave propagation, $1/q_n = \sqrt{\alpha_n/i\omega}$ is the thermal penetration depth at frequency ω, along with a factor of $1/\sqrt{i}$ conventionally included for notational simplicity[2]. Because q_n is compex, the two terms in the expression for the radially-scaled temperature $F_n(r)$ represent decaying waves. We will also be using the symbols $\gamma_n = q_n k_n$ and $\gamma_n^{\pm} = (q_n \pm 1/r)k_n$.

The matrix formulation represents the scaled temperature as the vector

$$\mathbf{F}_n(r) = \begin{pmatrix} F_n^-(r) \\ \\ F_n^+(r) \end{pmatrix}, \tag{5.3}$$

with the upper component equal to the first term in eq.(5.2), describing a wave traveling in the negative radial direction, and likewise the lower element for a positive-traveling wave. The complete temperature expression is the sum of the two vector components. The temperature throughout the system is determined by applying a succession of transition matrices to the temperature vectors at the system limits of $r = 0$ and $r \to \infty$, giving temperature at all points in terms of the limit temperatures, and solving the resulting system of two equations in two unknowns for the complete temperature field. The required transition matrices are calculated using interface boundary conditions, layer thickness, and knowledge of source strength, as next described.

5.3.1 Transition matrix calculation

The transitions of crossing an interlayer boundary, and traversing a single layer, are each represented by distinct matrices. A surface heating boundary condition is also implemented in matrix form. Temperature and thermal flux discontinuity conditions are used to calculate these expressions. For an interlayer boundary at an interface at radius r_j between an inner layer i and adjacent outer layer $j = i + 1$, with thermal resistance R, no thermal

source at the boundary, and flux f, the temperature discontinuity condition is

$$T_j(r^+) - T_i(r^-) = R_i \; f(r^-), \tag{5.4}$$

where $r^\pm$ is the decreasing/increasing radius as the boundary at r_j is approached. In terms of the scaled temperature $F(r)$, the matrix notation of eq.(5.3), and

$$f(r^-) = -k_i \frac{dT_i}{dr}\bigg|_{r^-}, \tag{5.5}$$

the discontinuity condition reads

$$F_j^+ + F_j^- = (1 + \gamma_i^- R_i) \; F_i^+ + (1 - \gamma_i^+ R_i) \; F_i^-. \tag{5.6}$$

Flux discontinuity at an interface with surface heating strength A_0 is

$$f_j(r^+) - f_i(r^-) = A_0 \tag{5.7}$$

which likewise becomes

$$\gamma_j^- F_j^+ - \gamma_j^+ F_j^- = \gamma_i^- F_i^+ - \gamma_i^+ F_i^- - A_0 r. \tag{5.8}$$

At a boundary with no heating, combining eqs. (5.6) and (5.8) to successively express first F_j^+, then F_j^-, in terms of $F_i^\pm$, yields

$$\mathbf{F}_j(r^+) = \mathbf{\Gamma}_{ji}(r_j) \; \mathbf{F}_i(r^-) \tag{5.9}$$

where

$$\mathbf{\Gamma}_{ji}(r_j) = \frac{1}{2\gamma_j} \begin{pmatrix} \gamma_j^+ + \gamma_i^- + \gamma_j^+ \gamma_i^- R_i & \gamma_j^+ - \gamma_i^+ - \gamma_j^+ \gamma_i^+ R_i \\ \gamma_j^- - \gamma_i^- + \gamma_j^- \gamma_i^- R_i & \gamma_j^- + \gamma_i^+ - \gamma_j^- \gamma_i^+ R_i \end{pmatrix}. \tag{5.10}$$

The matrix $\mathbf{\Gamma}_{ji}(r_j)$ thus represents the transition of the temperature vector from layer i to layer j.

The traversal matrix $\mathbf{U}_i(d)$ for traversing a distance d above initial radius r_0 within layer i is determined by requiring

$$\mathbf{F}_i(r_0 + d) = \mathbf{U}_i(d) \; \mathbf{F}_i(r_0), \tag{5.11}$$

which directly gives

$$\mathbf{U}_i(d) = \begin{pmatrix} e^{q_i d} & 0 \\ 0 & e^{-q_i d} \end{pmatrix}. \tag{5.12}$$

In crossing a heating surface at radius r, lying within layer i, the temperature is continuous, and eq.(5.6) with $R = 0$ is

$$F_j^+ + F_j^- = F_i^+ + F_i^-, \tag{5.13}$$

which, combined with eq.(5.8), gives the condition

$$\mathbf{F}_i(r^+) - \mathbf{F}_i(r^-) = \frac{A_0 r}{2\gamma_i} \begin{pmatrix} -1 \\ 1 \end{pmatrix}. \tag{5.14}$$

Heating surfaces which are coincident with an interface are handled by placing the source a distance ζ from the interface, and evaluating eq.(5.14) in the limit $\zeta \to 0$.

In a spherically-symmetric system with concentric surface heating only, thermal flux at the origin is zero, $f(r \to 0) = 0$, and for finite temperatures as $r \to \infty$, $F_N(r \to \infty) = 0$. From eq.(5.2), these conditions yield

$$\mathbf{F}_1(r = 0) = c_1^- \begin{pmatrix} 1 \\ -1 \end{pmatrix}, \tag{5.15}$$

and

$$\mathbf{F}_N(r_N) = c_N^+ \begin{pmatrix} 0 \\ 1 \end{pmatrix}. \tag{5.16}$$

5.3.2 Determination of temperature

Temperatures throughout the system, for the case of a single heating surface located within layer i at radius $r_s = r_i - \zeta$, are determined by relating the vectors $\mathbf{F}_i(r_s^{\pm})$ on opposite sides of the surface by eq.(5.14). Using the transition matrices $\mathbf{\Gamma}_{ji}$ and $\mathbf{U}_i$, $\mathbf{F}_i(r_s^{\pm})$ are then

expressed in terms of $\mathbf{F}_1(r=0)$ and $\mathbf{F}_N(r_N)$, leaving two equations in the two unknowns c_1^- and c_N^+ of eqs. (5.15) and (5.16) above.

Defining

$$\begin{aligned}\mathbf{A} = \begin{pmatrix} A^- \\ A^+ \end{pmatrix} &= \mathbf{U}_i(r_i - r_{i-1} - \zeta)\mathbf{\Gamma}_{i,i-1}(r_{i-1}) \\ &\quad \mathbf{U}_{i-1}(r_{i-1} - r_{i-2})\mathbf{\Gamma}_{i-1,i-2}(r_{i-2}) \\ &\quad ...\mathbf{U}_1(r_1)\begin{pmatrix} -1 \\ 1 \end{pmatrix} \end{aligned} \tag{5.17}$$

and

$$\begin{aligned}\mathbf{B} = \begin{pmatrix} B^- \\ B^+ \end{pmatrix} &= \mathbf{U}_i(-\zeta)\mathbf{\Gamma}_{i,i+1}(r_i)\mathbf{U}_{i+1}(r_i - r_{i+1}) \\ &\quad ... \ \mathbf{\Gamma}_{N-1,N}(r_N)\begin{pmatrix} 0 \\ 1 \end{pmatrix}, \end{aligned} \tag{5.18}$$

$\mathbf{F}_i(r_s^{\pm})$ become

$$\mathbf{F}_i(r_s^+) = c_N^+\mathbf{B}, \tag{5.19}$$

and

$$\mathbf{F}_i(r_s^-) = c_1^-\mathbf{A}. \tag{5.20}$$

The source condition (5.14) then reads

$$c_N^+\mathbf{B} - c_1^-\mathbf{A} = \frac{A_0(r_i - \zeta)}{2\gamma_i}, \tag{5.21}$$

yielding

$$c_1^- = \frac{A_0(r_i - \zeta)}{2\gamma_i}\frac{B^- + B^+}{A^-B^+ - A^+B^-} \tag{5.22}$$

and

$$c_N^+ = \frac{A_0(r_i - \zeta)}{2\gamma_i}\frac{A^- + A^+}{A^-B^+ - A^+B^-}. \tag{5.23}$$

Temperature distributions in any layer i may now be calculated from $T_i(r) = \frac{1}{r}[F_i^-(r) + F_i^+(r)]$. For example, in layer 2, $T_2(r) = \frac{1}{r}[F_2^-(r) + F_2^+(r)]$, with

$$\mathbf{F}_2(r) = c_1^- \mathbf{U}_2(r - r_1)\mathbf{\Gamma}_{21}(r_1)\mathbf{U}_1(r_1) \begin{pmatrix} -1 \\ \\ 1 \end{pmatrix}. \tag{5.24}$$

5.3.3 Incorporation into a frequency-domain TTR signal model

TTR experiments define a TTR signal based[79] on the increase in phase of the optical power of a reflected or transmitted probe pulse, in response to an underlying temperature increase[44] in the system induced by a pump, or excitation, pulse, arriving at the system a time τ before the probe. Pulses are typically generated by ultrafast lasers with pulse durations on the order of 10 to 100 fs, impulsively heating nanoparticles with typical cooling times of 10 to 100 ps. In addition, the heating pulse train is typically optically modulated for subsequent lock-in detection. Here we assume the case of sinusoidal modulation at frequency $\omega_0 = \frac{2\pi}{T_0}$. Probe beams are not necessarily modulated in general. The signal is measured by a lock-in amplifier, receiving its input from a probe beam photodetector, and referenced to the modulation frequency ω_0 of the pump pulse beam. The lock-in amplifier mixes the input with a modulation reference signal, and outputs the in-phase (real) and 90° out-of-phase (imaginary) parts of the detected signal. In order to relate this to a quantity which is positive and increases with temperature, and which is also independent of the pump and probe beam powers, the TTR signal $TTR(\omega_0, \tau)$ is defined[79] as

$$TTR(\omega_0, \tau) = -\frac{\mathrm{Re}(Z(\omega_0, \tau))}{\mathrm{Im}(Z(\omega_0, \tau))}, \tag{5.25}$$

where $Z(\omega_0, \tau)$ is the lock-in signal.

The complex lock-in output for a TTR experiment, as a function of probe delay time τ, is given by Schmidt[80] as

$$Z(\omega_0, \tau) = \frac{\beta Q Q_{probe}}{T^2} \sum_{k=-\infty}^{\infty} H(\omega_0 + k\omega_{rep}) e^{ik\omega_{rep}\tau} \tag{5.26}$$

where β is the product of detector responsivity and electronics gain, $1/T$ is the repetition rate of the laser, Q and Q_{probe} are the absorbed pump and incident probe pulse energies, and H is the frequency-domain surface temperature.

We can now apply our spherical transport model to calculate thermal parameters by fitting the signal (5.25) to TTR data. For the simple case of a particle of radius a at layer 1, in an embedding medium at layer 2, with resistance R at the interface, $H(\omega) = \frac{1}{r}[F_1^-(a) + F_1^+(a)]$, where

$$\mathbf{F}_1(a) = c_1^- \, \mathbf{U}_1(a) \begin{pmatrix} -1 \\ \\ 1 \end{pmatrix}, \tag{5.27}$$

$$c_1^- = \frac{A_0 a}{2\gamma_1} \frac{B^- + B^+}{A^- B^+ - A^+ B^-}, \tag{5.28}$$

and

$$\mathbf{A} = \mathbf{U}_1(a) \begin{pmatrix} -1 \\ \\ 1 \end{pmatrix}, \; \mathbf{B} = \mathbf{\Gamma}_{12}(a) \begin{pmatrix} 0 \\ \\ 1 \end{pmatrix}. \tag{5.29}$$

5.3.4 Multilayer model applications

Before applying the multilayer model to our own experimental measurements, in this section we present interesting applications of the model for broader purposes in studies of nanoparticle thermal responses. The model may be used to predict the thermal response of a stratified nanoparticle system generally, to evaluate the sensitivity of the TTR signal to changes in thermal and geometric parameters, and to simulate the effect of the presence of layered structures. As described previously, nanoparticle systems usually have characteristic sizes well below the phonon mean free path of one or more of the constituent

materials, calling for a quasi-[81,82] or fully[83,84] ballistic model of transport. Although ballistic thermal flux is not determined by the local temperature as in diffusive transport, a pseudo-temperature[81] may be defined in terms of the system's internal energy at a given position and time, providing a means of comparing the results of diffusive and ballistic models. The diffusive model presented here is useful as an approximation to a more accurate and mathematically complex ballistic model.

Utilizing a multilayer model can improve agreement with TTR measurements of multilayer and core/shell nanoparticles, and can produce more accurate values for fitted parameters, than simpler models. Figure 5.2 shows the results of fitting the multilayer model to the TTR data of Wilson[64] *et al.* for Pt nanoparticles in water, with nanoparticle radius of 5 nm, a citrate capping layer, and TTR parameters given by the authors.[64] The change in optical depth shown in this data may be calculated in the multilayer model by replacing the thermoreflectance coefficient of the model given above[80] with a $\Delta T/T$ coefficient, such as calculated by Averitt *et al.*[85] The fitting parameters were thermal boundary conductance at the Pt/citrate interface and capping layer thickness. The multilayer model fits the TTR data with a slightly improved R^2 value of 0.974, compared to the estimated value of 0.966 for the original two-layer model fit by Wilson. We find a conductance of 226 MW/m^{2}K, about 70% greater than the authors' result of 130 MW/m^{2}K, and a capping layer thickness of 0.17 nm. The greater quality of fit indicates that the citrate layer contributes significantly to thermal resistance, and that correspondingly less resistance is due to interface resistance, as opposed to other models which effectively replace the TBR plus cappin glayer with TBR only. Consequently, the multilayer model finds a more accurate, higher value of TBC. Additionally, the similarity of the fitted citrate thickness value to measurements found for gold citrate-capped nanoparticles,[86] determined by observing increased aggregation with increasing known adsordbed hycarbon lengths, shows that the thickness value is reasonable.

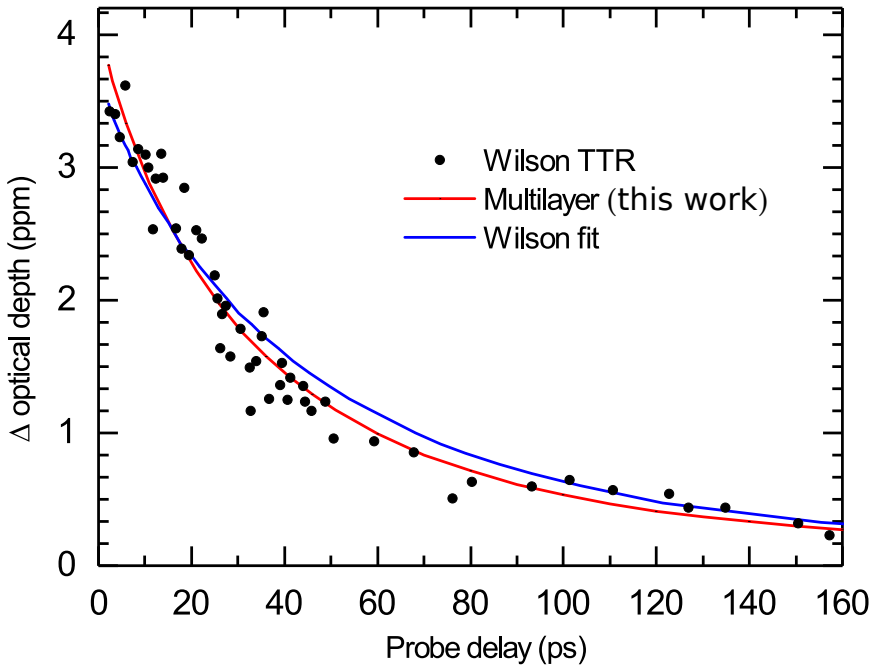

Figure 5.2: Fit of the multilayer model to TTR data of Wilson[64] *et al.* for Pt nanoparticles in water, with TBR value and capping layer thickness as fitting parameters. The multilayer model fits the measurements with an improved R^2 value, and yields a thermal boundary conductance of 226 MW/m^{2}K.

We also consider the case of aqueous gold nanoparticles, applicable to biological applications, and show the predicted increase of TTR signal decay times due to increasing TBR at the Au/H_2O interface. Figure 5.3 is a plot of the modeled TTR signal for aqueous gold nanoparticles of radius $a = 10$ nm, with the parameters in Table 5.1. The value for TBR is estimated as the intermediate value of the range given by Ge *et al.*[40] for Au-core/AuPd shell and solid AuPd nanoparticles.

For this example and others with dimensions well below the phonon mean free path of gold, we expect that models employing platinum and gold thermal conductivities that are reduced for nanoscale effects may provide the best match to data. However, not all NP systems are sensitive to all conductivities present. To assess the sensitivity of the

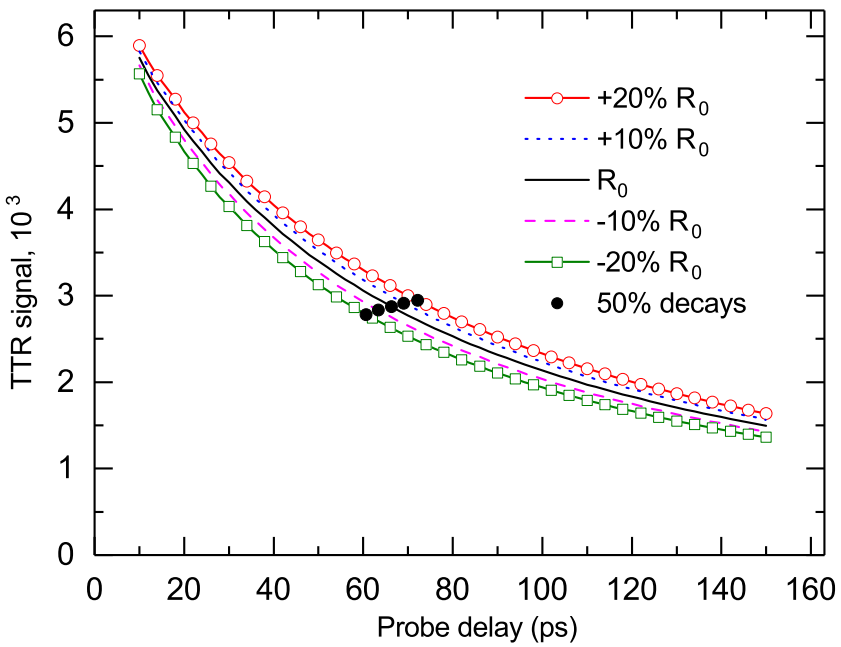

Figure 5.3: Raw (unscaled) modeled TTR signal for aqueous Au nanoparticles. Times are indicated for decay to 50% of the signal at probe delay of 10 ps. The TTR signal is dimensionless, as indicated by eq. (5.25).

fit to conductivity values in this case, we vary both gold[88] and citrate[89] conductivities between 50% of bulk and twice bulk values, finding essentially no change in results for fitted parameters, the calculated TTR signal, or for sensitivities to parameters found from TTR values. With a large conductivity for gold, relative to both the water matrix and the citrate layer, interface transport and diffusion in the water matrix are the dominant decay channels, so the TTR signal is not sensitive to the nanoparticle conductivity. We also expect sensitivity to citrate conductivity to decrease with capping thickness, so low sensitivity to citrate conductivity is expected for the fitted thickness value, which is small relative to particle radius. In general, however, when fitting the diffusive multilayer model to data from cooling nanostructures, large differences between modeled and measured TTR values imply the need for a more advanced ballistic transport model.[81]

Aqueous gold NP modeling			
Repetition rate	ω_s	$2\pi \cdot 75$	Mrad/s
Pump modulation frequency	ω_0	$2\pi \cdot 100$	krad/s
Nanoparticle radius	a	10	nm
Au thermal conductivity[87]	k_1	318	W/mK
Au volumetric specific heat[87]	c_1	$2.49 \cdot 10^6$	J/m^{3}K
H_2O thermal conductivity[87]	k_2	0.6	W/mK
H_2O volumetric specific heat[87]	c_2	$4.18 \cdot 10^6$	J/m^{3}K
Au/H_2O thermal boundary conductance[40]	$1/R$	200	MW/m^{2}K

Table 5.1: Model parameters for aqueous gold nanoparticles.

Resistance to thermal flux in nanoparticles can be due to both TBR and capping layers simultaneously, and with similar magnitudes of effect on the TTR signal. These physically distinct resistances are modeled independently in the multilayer thermal model, and the model can therefore show that the TTR signal changes differently, at different delay times, with changes to these parameters, so that the two quantities can be determined separately by fitting the model to TTR data. These differences are quantified by the *sensitivity* of the TTR signal, which for TBR is defined as the relative change of the signal with respect to the fractional change in TBR, at a fixed probe delay time of 100 ps.[90] For example, a sensitivity of 0.5 means that a 10% increase in the TBR would cause a 5% increase in the TTR signal. Figure 5.4 shows the change of the TTR signal for separate changes to TBR and capping thickness for a Pt nanoparticle in water, with a citrate capping layer. The signal change between 0 and 60 ps probe delay shows that increasing TBR has a greater effect on the signal at short times than increasing capping thickness, which is reasonable because the TBR is located closer to the source of heating at the nanoparticle. Increasing capping thickness has greater effect on the signal at times after 60 ps. Because the TTR signal responds differently to TBR and capping thickness at different delays (except at the single time near 60 ps), fitting the model to TTR data will reveal a local minimum at the

independent TBR and capping values that give a best fit. Figure 5.5 plots the sensitivity of the TTR signal to TBR and capping thickness changes, and shows that the greatest sensitivities occur at 275 and 285 ps respectively. Fitting the model to data that includes these delays will yield the least uncertainty in results.

5.4 Design of the gold nanoparticle experiment

The elements mentioned in section 4.7, required for TTR meaurements of thermal dynamics of a nanoscale system, are implemented by the experimental setup shown in figure 5.6. In the following sections we discuss details of each component of the TTR apparatus, and table 5.2 lists typical parameters.

TTR parameters		
Source wavelength	800	nm
Pulse duration	150	fs
Repetition rate	76	MHz
Maximum probe pulse delay	1.8	ns
Pump modulation rate	50	kHz
Probe modulation rate	500	Hz
Beam waist	6.59	μm FWHM
Pump average power at sample	2.9	mW
Pump pulse energy	38	pJ
Probe average power at sample	1.5	mW
Objective lens focal length	20	mm
Beam diameter before objective	0.95	mm FWHM
Pump lock-in integration time	100	μs
Pump lock-in sensitivity	100	mV
Probe lock-in integration time	3	s
Probe lock-in sensitivity	1	mV
Lock-in roll-off	6	dB/octave
Lock-in reserve	60	dB

Table 5.2: Numerical parameters of the ultrafast TTR experiment. FWHM indicates 'full width half maximum,' the beam diameter at 50% of peak intensity.

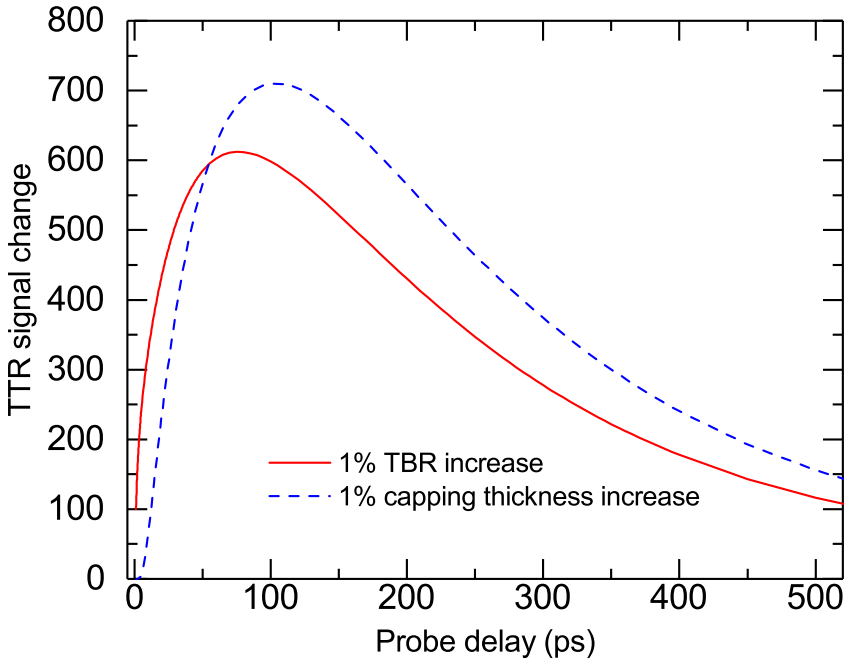

Figure 5.4: Calculated change of the TTR signal for a 1% increase of TBR and capping thickness, as a function of delay time, for Pt nanoparticles in water. TBR has the experimentally-measured value[64] $R_0 = 7.69 \cdot 10^{-9}$ m^{2}K/W, and the capping layer is 1 nm of citrate. The nanoparticle radius is 5 nm.

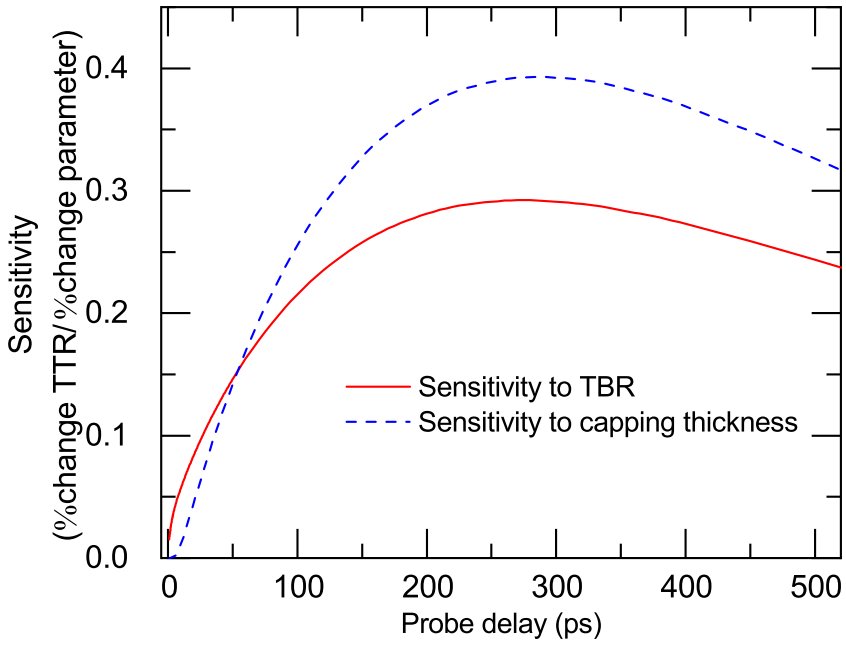

Figure 5.5: Sensitivity of the TTR signal to TBR and capping layer thickness for Pt nanoparticles in water. The multilayer model predicts the greatest sensitivities to TBR and capping thickness at 275 and 285 ps, respectively.

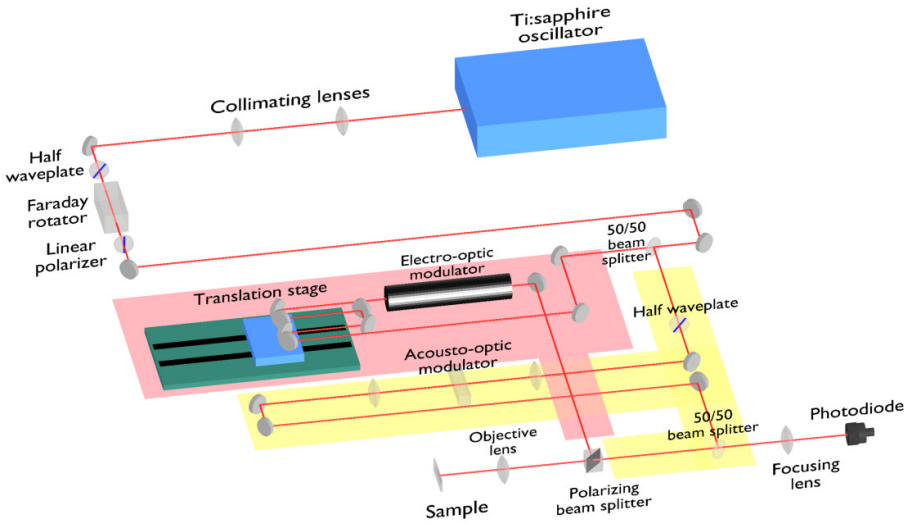

Figure 5.6: Optical layout of the TTR apparatus. The pump and probe beams include colinear alignment at the sample and objective, crossed linear polarizations, dual modulation and separate lock-in detection. Red shading indicates the pump arm, and yellow shading is for the probe arm. The pump arm also includes a 4-passed delay line. To equal the optical path of the pump arm for simultaneous arrival of pulses at the sample, the extended section of the probe path, including the acousto-optic modulator, is measured to the appropriate length. Half-waveplates are aligned to rotate linear polarizations by 90° relative to the vertical.

TTR equipment	
Ti:sapph pulsed laser	In-house
Pump lock-in amplifier	Stanford Research SR 844
Probe lock-in amplifier	Stanford Research SR 830, 810
Electro-optic modulator (pump)	Conoptics 350-210, M-25D controller
Function generator (EOM)	Hewlett-Packard 3325
Acousto-optic modulator (probe)	Isomet 1250C-2, 535C-1 controller
Function generator (AOM)	Hantek DDS-3X25
Delay line translation stage	Newport Research, ESP 300 controller
CCD camera	Mightex BCE-C050-US
Photodetector	Thor Labs DET 110
Band-pass filter	In-house
Objective lens	Mitutoyo 10X NIR

Table 5.3: Major equipment used in the TTR experiment.

5.4.1 Ultrafast source and optical isolation

For our experiments we used a home-built ultrafast laser, which uses a Coherent Verdi G5, 532 nm, 5 W OPSL laser as a pump laser, and a Ti-doped sapphire (Ti:sapph) crystal as its broadband gain medium, lasing at 800 nm. Our laser uses a typical ultrafast laser configuration, in which Kerr lens mode-locking occurs as a balance between the pulse-shortening Kerr effect and the pulse-stretching self-phase modulation effect. Focusing of mode-locked pulses onto the crystal is by a pair of curved mirrors, and a pair of triangular prisms provide the negative dispersion required for Kerr lens mode-locking. The laser cavity length was about 2 m, giving a repetition rate of $\omega_{rep} = 76.33$ MHz of this Ti:sapph oscillator. The average optical power after the output coupler was about 350 mW. Following the oscillator are a red-reflecting dichroic mirror to eliminate 532 nm leak-through from the beam, as well as a collimating lens pair.

We have measured the pulse duration using an auto-correlation method: a non-linear, frequency-doubling BBO (β BaB_2O_3) crystal, followed by a filter that transmits the frequency-doubled pulses at 400 nm and blocks the original 800 nm. Frequency doubling is a '$\chi^{(2)}$' non-linear process, with an output that is proportional to the square of the sum of the incoming pulse power from the pump and probe pulses each, so that the 400 nm output pulse power is very sensitive to the amount of overlap of pump and probe pulses in the BBO crystal. By stepping the translation stage of the pump arm (see section 5.4.2), we can estimate the duration of ultrafast pulses: we find a duration of about 150 fs for our laser, more than fast enough to time-resolve thermal dynamics taking place on a 100s of ps scale.

Our apparatus also includes an optical isolator, which allows pulses to propagate in the downstream direction only. In early trials, using reflective thin film samples at normal incidence to the incoming beam, pulse backreflections propagated to the Ti:sapph source,

causing it to easily drop out of mode-locked operation into continuous-wave (CW) operation. The polarization-dependent isolator readily fixed this problem, using the mechanism of Faraday rotation of the linearly polarized beam. The beam leaving the oscillator has linear polarization in the horizontal ('P') direction, which is rotated to vertical ('S') polarization by a periscope mirror pair before the dichroic mirror. A 1/2-wave ('$\lambda/2$') plate aligns the incoming S beam to a polarizer just after the isolator's incoming aperture at 45° to the vertical so that the beam is passed. The Faraday effect rotates the beam back to S mode. The upstream, backreflected beam experiences Faraday rotation in the same absolute direction, crossing it with the polarizer at the isolator incoming end, where the upstream beam is extinguished.

5.4.2 Heating (pump) and signal (probe) arm parameters

As time-domain experiments, TTR designs must consider any possible residual heating of the system due to pulses arriving at the sample prior to the last pulse before a given instantaneous time. For our nanoparticle system, the cooling time estimated in section 4.6 was approximately 300 ps. At the oscillator's repetition rate of 76.33 MHz, the time between pulses is 13.1 ns, very long relative to the estimated cooling time, so we expect only a small effect due to pulse accumulation. The pulse accumulation effect is accounted for in the TTR signal model we employ in eq. (5.26).

Again as a time-resolved measurement, the TTR apparatus must pump and probe nanoparticles using pulse durations much shorter than the estimated cooling time. The ultrafast pulse duration of 150 fs certainly fulfills this requirement, being about 10^3 times shorter than the cooling time estimate. However, pulses are stretched in time by propagation through dispersive media, and while the air medium of the majority of the beams' paths has relatively little stretching effect, the passage of the beam through the crystal medium of the

optical isolator of the previous section, as well as that of the pump beam through the KDP crystal of the EOM discussed in section 5.4.3, have a significant stretching effect. Pulse durations folowing the EOM were measured using the BBO method described in section 5.4.1, and although precise data were not retained, the result was a pulse duration near 1 ps, so that pump pulses were stretched up to approximately seven times their original duration. This value remains sufficiently short for time-resolved TTR measurement.

The controlled delay time of probe pulses arriving at NP samples is effected by shortening the pump beam path, so that pump pulses arrive successively earlier than probe pulses. Probe delay times are calculated by dividing the speed of light into the amount by which the pump path length is shortened, found by multiplying the pump delay line position relative to a 'time zero' position, where the two arm paths are of equal length, by a factor of 4 to account for the 4-passing of the delay line described in section 4.4. The time zero position of the translation stage is generally found by moving the stage until a sharp peak in the lock-in signal of eq. (5.26) is observed. At this position, very high electron temperatures, occuring prior to thermalization with the ionic lattice, give the Au NPs a very high thermoreflectance coefficient,[48] which is observed as a large change in the lock-in signal at the pump modulation frequency. Prior to interaction with the lattice, but following electron thermalization among themselves, electrons can generally have temperatures on the order of 10^3 K, and at these high temperatures the effect of the broadening of the step of their Fermi distribution function becomes dominant over that of the phonon density increase mentioned in section 4.3. The broadening effect is much stronger at photon energies near the ITT of 2.54 eV (494 nm), but is still significant at our experiment's photon energy of 1.55 eV (800 nm).

The time resolution of the TTR apparatus is nominally the minimum step size of the delay line, times four for the four-passing of the stage, divided by the speed of light, for a

value of about 14 fs. Actually, the limiting factor of time resolution is the greater value of the pump and probe pulse duration, mentioned above.

As discussed in section 4.3, we choose a maximum phonon temperature increase of 1 K per pump pulse absorption by a nanoparticle to ensure that changes in reflected probe pulse power are linearly related to the particle surface temperature. As mentioned in section 4.1, the probe pulse energy was adjusted downward, with neutral-density (ND) filtering, to equal 50% of the pump pulse energy. Lab optical power meters measure the average optical power P_{ave} of a pulse train beam. To determine the desired P_{ave} to cause the chosen temperature increase of 1 K, we consider two features of the absorption process. First, with a pulse duration of 150 fs, and diffusion taking place on the 100 ps scale, no significant pulse energy will have diffused from the nanoparticle, so we may estimate the thermal energy ΔE_{th} gained by the particle, but prior to diffusion, as the pulse energy initially absorbed E_{abs}. Second, although greater absorption within the particle occurs near its surface facing incident photons, the gold particle has a thermal conductivity about three orders of magnitude greater than the surrounding polymer, and the particle comes to an internal equilibrium prior to significant diffusion, so that the specific heat of gold $c_{p,V}$ may be used to calculate the thermal energy required to raise its temperature by $\Delta T = 1$ K. We then have

$$\Delta E_{th} = E_{abs} = c_{p,V}\ V\ \Delta T, \tag{5.30}$$

where V is the nanoparticle volume. The absorbed pulse energy E_{abs} is the average absorbed power P_{abs} times the period of pulse repetition, or in terms of the pulse repetition rate f_{rep}

$$E_{abs} = \frac{P_{abs}}{f_{rep}}. \tag{5.31}$$

The natural choice to express absorbed power in terms of the desired incident average pump beam power, the nanoparticle absorption cross-section σ_{abs} is the natural choice, with $P_{abs} = \sigma_{abs} I_{inc}$, where I_{inc} is the incident beam intensity. For the cross-section,

we find a value calculated from Mie theory and the discrete dipole approximation[75] of $\sigma_{abs} = \sigma_{\text{eff}}\ A_{proj} = 0.030\ A_{proj}$, where A_{proj} is the particle's projected area and σ_{eff} is the nanoparticle *absorption efficiency*. The particle reflectivity is effectively included in the value of σ_{eff}. For the intensity, we use the average intensity over the $\frac{1}{e^2}$ beam diameter, w, for $I_{inc} = \frac{P_{inc}}{\pi \frac{w}{2}^2}$. Combining expressions for $E_{abs},\ P_{abs},$ and I_{inc} in eq. 5.30, we have P_{inc} in terms of ΔT with

$$P_{inc} = \frac{\pi}{3} \frac{c_{p,V} f_{rep} r w^2}{\sigma_{\text{eff}}} \Delta T, \tag{5.32}$$

with r the nanoparticle radius. The most readily adjusted values in eq. 5.32 are the pump incident power and the beam diameter. Rearranging, and considering other parameters as constants, we have

$$\frac{P_{inc}}{w^2} = \frac{\pi}{3} \frac{c_{p,V} f_{rep} r}{\sigma_{\text{eff}}} \Delta T = \text{constant}, \tag{5.33}$$

to show the relationship between changes in these two most easily adjusted parameters (incident power and beam diameter). To ensure that sufficient beam power is present at the sample, we see that its required value can be reduced by lowering w, and that it scales as the square of w. Choosing an objective lens with a typically short focal length and small spot size should assure that the required pump power can be achieved. Short focal lengths suggest utilizing microscope objectives: for a Mitutoyo near-infrared 10X objective with a focal length of 20 mm, we measure a waist size of $w = 6.59\ \mu$m, about 12% below an estimate of 7.47 μm from the Gaussian beam optics formula $w = \frac{4\lambda}{\pi} \frac{f}{D}$ for the waist diameter of a converging or diverging beam, where the parameters of wavelength λ, lens focal length f, and beam width incident to the lens D, are listed in table 5.2. The 12% discrepancy is most likely due to a change in optics between the times of beam diameter and waist size measurements, which caused an increase in the value of the beam diameter from the value in the table. Evaluating eq. 5.32 with this waist size, we find $P_{inc} = 2.9$ mW. Additionally, the square wave modulation of the pump beam causes its average power to drop to half the

value of the unmodulated beam, so a reading of $2 \cdot 2.9$ mW $= 5.9$ mW is set using a lab power meter to obtain the proper pulse energy for 1 K temperature increase.

We note that in the formula for waist diameter the beam width D is defined as the $\frac{1}{e^2}$ beam width, while the width in table 5.2 is the FWHM value D_{FWHM}. Both definitions refer to a Gaussian intensity profile along a normal to and through the optical axis, with maximum intensity I_0, of the form $I(r) = I_0 e^{-2\frac{r^2}{(D/2)^2}}$, at distance r from the axis. The two definitions of beam width are related by

$$I(D_{\mathrm{FWHM}}) = \frac{I_0}{2} = I_0 e^{-2\frac{(D_{\mathrm{FWHM}}/2)^2}{(D/2)^2}}, \tag{5.34}$$

from which $D_{\mathrm{FWHM}} = \sqrt{\frac{\log 2}{2}}\ D = 0.589\ D$.

5.4.3 Modulation and lock-in detection

As described in section 4.3, TTR relies on a change in reflected optical power with temperature as a temperature probe. A linear relationship between power and temperature is expected for temperature increases of about 1 K. From the values of the thermoreflectance coefficients for Au and Mo, the reflected power fractional change for a 1 K temperature change is on the order of one part in 10^4. At the very least, a photodetector with more than 4 digits of precision would be required to detect such a change. In practice, the contribution of each noise source has to be reduced as much as reasonably possible to reduce the accumulation of uncertainties in final results, to extract the change in power from a background about 10^4 times larger than the quantity of interest, and to safely attribute the measurement to NP temperature increase, rather than to other plausible effects: examples include changing pump/probe spot overlap at the sample due to imperfect alignment of an incoming beam to the translation stage employed to control pump and probe pulse relative delay times, or unintended heating due to probe pulses, as opposed to the intended heating due to pump pulses.

TTR experiments apply beam modulation with lock-in amplifier detection, referenced to the modulation frequency, to meet these practical needs. In all implementations of our TTR experiments, pump and probe pulses traversed two different optical paths, or arms, and were recombined into a single beam upstream of arrival at a sample. All beams were linearly polarized. In early implementations of our TTR apparatus, the probe arm was unmodulated, and its path length was fixed. During data collection with this early implementation, probe pulses were continually incident on samples at fixed, regular times. For the pump arm, the optical path passed over a translation stage four times, using retroreflecting mirrors to ensure mutually parallel beams and negligible lateral beam drift during stage translation. The pump path length was adjusted to equal that of the probe by moving the stage by small increments, setting that stage position as 'time zero,' the position of zero delay of probe pulses relative to pump pulses. To effect a probe delay, the pump arm was shortened by moving the stage, advancing the arrival of pump pulses at the sample, providing the equivalent of a probe pulse delay.

The translation stage in the pump arm was followed immediately by an electro-optic modulator (EOM), modulating both phase and amplitude. The EOM functions by passing light through several cm of a potassium dideuterium phosphate (KDP) crystal, an optical material with a strong Pockels, or electro-optic, effect: a degree of birefringence which depends on the strength of an externally applied, DC, electric potential, supplied to the KDP by a separate controller. By applying the Pockels effect to one component of the beam polarization, we have a voltage-controlled phase delay of that component, and with the delay adjusted to 90 °, a voltage-controlled polarization rotation. The beam then passes through a polarizing beamsplitter (internal to the EOM) aligned to the unmodulated beam, and the EOM then functions as an amplitude modulator, turning the beam off whenever a control signal is applied to the EOM controller. The controller output could be either at a fixed voltage, or off, *i.e.* the controller was a 'digital,' as opposed to continuous or

'analog' controller, so that the EOM functioned as a square wave modulator of the pump beam power. The EOM control signal was run at frequency $1/T_0 = 50$ kHz for final data collection. This frequency value was chosen as a balance between high values, to reduce signal noise which decreasd with frequency, while remaining below about 1 MHz, where decreasing sensitivity of the TTR signal to TBR was predicted, shown in figure 5.7. The pump pulse train is illustrated in figure 5.8.

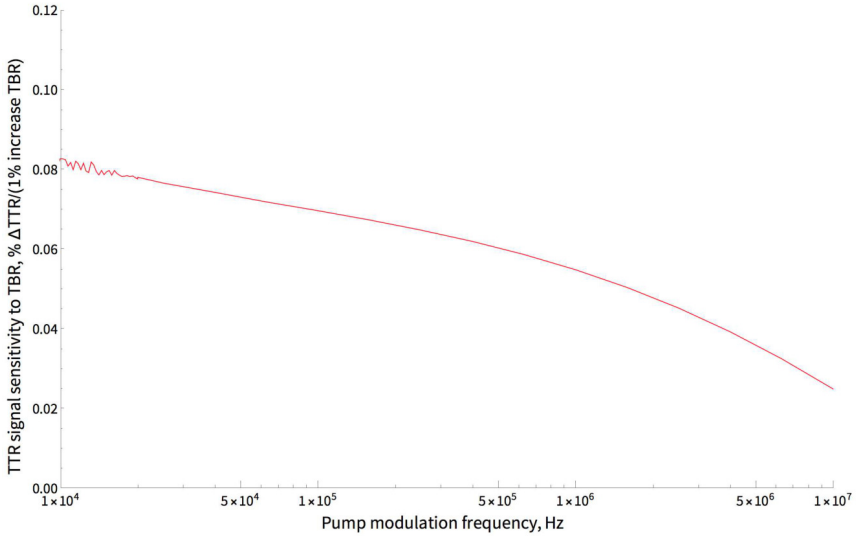

Figure 5.7: Plot of sensitivity of the TTR signal to a 1% increase in TBR value at the Au/citrate interface.

Later experiments added sinusoidal modulation of the probe beam optical power by means of acousto-optical modulation (AOM), the Bragg diffraction of light by a transient grating induced by RF acoustic waves in an optical crystal, TeO_2, in our experiment. The acoustic waves are generated by a piezoelectric crystal attached to the optical crystal. Our AOM used traveling acoustic waves, which cause a Doppler shift in the diffracted beam wavelength, which was a small fraction of the incoming wavelength. The probe arm was routed to use the first order diffracted beam, which had intensity proportional to the AOM control signal amplitude applied to its controller. The control signal frequency $1/T_{probe}$ was

set to 500 Hz for final data collection, observed to have the least measurement uncertainty within the bandwidth of the signal generator providing the signal. Sinusoidal modulation of the probe beam is graphed in figure 5.9.

Figure 5.10 shows the effect of the two modulation stages on the intensity of pulses arriving at the sample. In addition to modulation, the pump and probe arms were arranged with linear polarizations crossed at 90°, and beams reflected from samples passed through a polarizing beamsplitter before reaching the photodetector, as discussed in subsection 5.4.4, so that any pump signal reaching the detector carries about 10^4 times less power than the probe beam, and any oscillation in the probe signal, at the pump modulation frequency, may be attributed to the temperature changes in samples and consequent modulation in reflected probe power via the thermoreflectance effect. To detect this frequency, the detector output was first sent to a lock-in amplifier referenced to the pump modulation frequency; this lock-in was followed by another lock-in referenced to the probe modulation frequency. In this arrangement, the first modulation stage serves as a detector of temperature effects in the sample. The second stage, with the probe beam locked into its own modulation frequency, functioned as a noise reduction measure. As discussed in section 5.5.1, we believe fluctuations in the beam powers arriving at the sample to be the main source of noise. Additionally, although the probe pulse train induces heating in the sample, at a strength lower than, but on the same scale, as the pump train, because it has no significant component at the pump modulation frequency, the reflected probe pulse train may be taken as responsive to the surface temperature as heated by the pump pulses.[80]

The component of the reflected probe spectrum which is actually measured at the output of the second lock-in is shown in figures 5.11 through 5.13. This and the following plots show the amplitude of a frequency spectrum. Before modulation, the probe has the delta function comb spectrum of a pulse train. With a measured pulse duration of

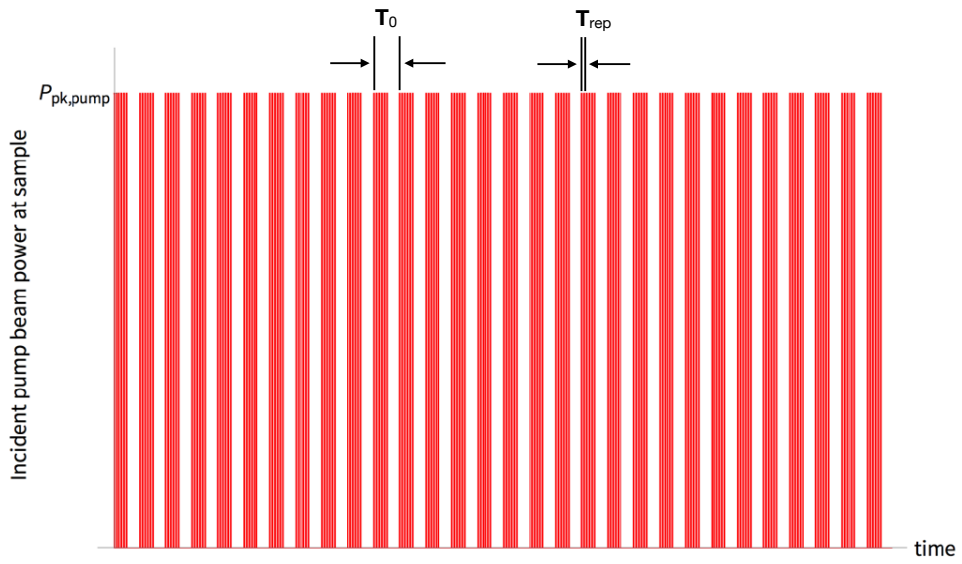

Figure 5.8: Pump beam intensity arriving at samples. In our experiment, $T_0/T_{rep} \approx 10^2$.

$t_{pulse} \approx 100$ fs, the envelope in figure 5.11 has width relative to the repetition rate ω_{rep} $1/t_{pulse}/\omega_{rep} \approx 10^6$, so that the peaks effectively have equal areas. Although the width of each peak in the spectrum is actually finite and found from the time of exposure t_{exp} of the sample to probe pulses as $2/t_{exp}$, this bandwidth is many orders of magnitude smaller than ω_{rep}, so that the peaks may be taken as delta functions.

In figure 5.12, the square wave modulation of the reflection coefficient of the sample, at rate ω_0, shown in figure 5.10, and thus of the reflected probe power, adds sidebands to each original delta function, at multiples of distance ω_0 from the original delta functions, as seen by the *convolution theorem* of Fourier transforms. The theorem specifies that the transform of a product of functions is the convolution of individual transforms, and that the same is true for inverse transforms. The first stage of probe modulation occurs indirectly

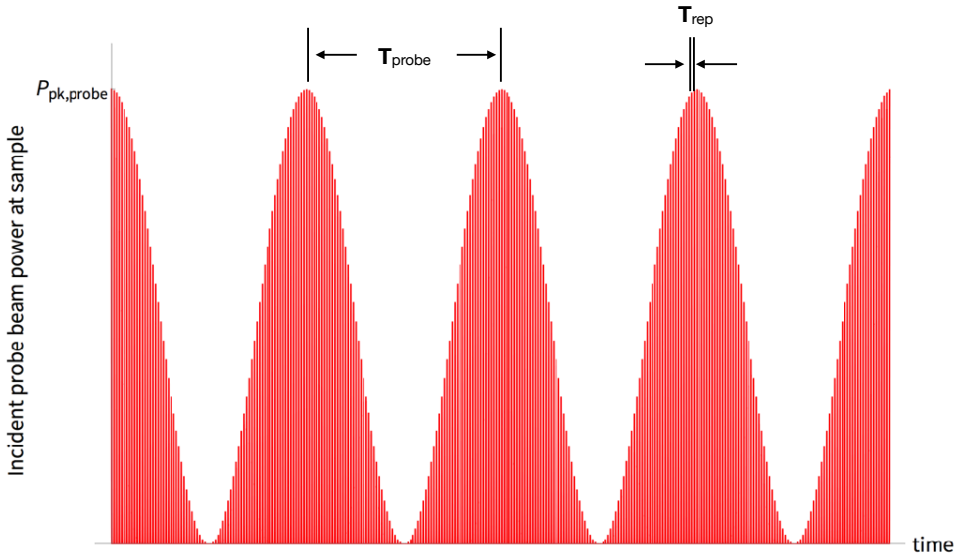

Figure 5.9: Incident probe beam intensity at samples. $T_{probe}/T_{rep} \approx 10^5$ in our TTR implementation.

through the temperature changes induced by the pump beam, effectively multiplying the time-domain probe by a square wave plus a constant. Being a linear transform, the Fourier transform of a sum is the sum of transforms, so that the added constant only increases the weight of the delta function at zero frequency. A square wave of frequency ω_0 has a spectrum of delta functions with relative weights 1, 1/3, 1/5, *etc.,* and spacing ω_0. The first three harmonic sidebands are shown. Because the thermoreflectance effect only modifies the probe time-domain signal by a small fraction, the sidebands weights shown in figure 5.12 are exaggerated. The convolution of a function with a delta function shifts the original function origin to the delta function location, giving a modified comb spectrum.

The second stage of modulation follows the same frequency shifting process as for square wave modulation, except that the modulating spectrum is that of a sine wave of

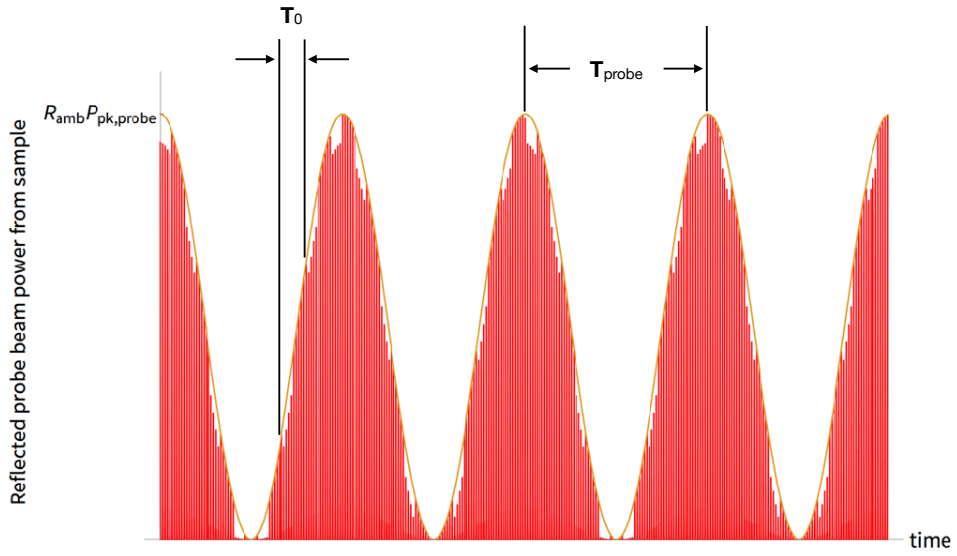

Figure 5.10: Illustration of the effect of the two stages of modulation on the beam intensity reflected from samples. With frequency $\omega_0 = 2\pi/T_0$, probe pulses have reduced (in the case of Au NPs) intensity due to pump-induced thermoreflectance of the sample material. Signal detection is locked in to frequency ω_0.

frequency $\omega_{probe} \ll \omega_0$ plus a constant, *i.e.* delta functions located at $\pm\omega_{probe}$. Convolution then adds two sidebands next to each probe component, giving the spectrum in figure 5.13, with those chosen for dual lock-in measurement indicated. Lock-in amplifiers measure a signal's amplitude and phase by mixing a signal with a reference, *i.e.* multiplying the signal by a sine wave at the reference frequency. In the frequency domain, this process is again described by the convolution theorem: the mixing operation is equivalent to convolution with the single delta function spectrum of a sine wave, effectively selecting the reference frequency for measurement. The indicated probe spectral components, of relatively small weight relative to the original comb spectrum weights, can be differentiated from the original

signal due to their being shifted away from the original frequency values of the spectrum, enabling the small thermoreflectance changes induced in the probe signal to be measured.

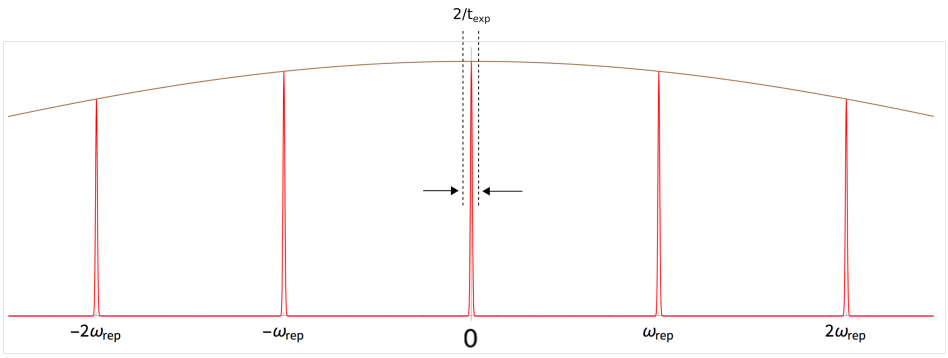

Figure 5.11: Frequency spectrum of the probe pulse train, with spacing ω_{rep}. The decay of the envelope function is exaggerated, and the peaks are considered to have equal areas; similarly the pulse width $2/t_{exp}$ is not significant relative to ω_{rep}, so that the peaks are considered to be delta functions.

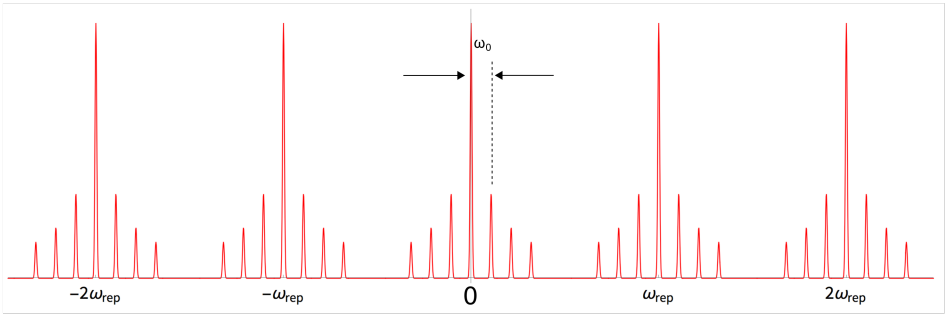

Figure 5.12: Modification of the probe spectrum due to square wave modulation of optical power reflected from samples. In our experiment, $\omega_{rep}/\omega_0 \approx 10^2$. Peak heights are proportional to delta function areas.

5.4.4 Colinear design and polarized beam separation

The last essential feature of the TTR setup to consider is seen on the apparatus diagram in figure 5.6, where the pump and probe arms recombine at the polarizing beamsplitter

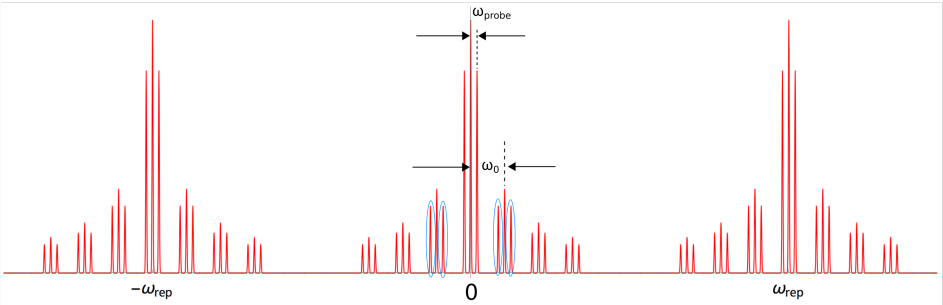

Figure 5.13: Further probe spectrum alteration from sine wave modulation, adding sum and difference frequencies. The experimental ratio of pump to probe modulation rates is $\omega_0/\omega_{probe} \approx 10^3$. The circled components are the amplitudes measured by dual lock-in amplifiers.

cube into a single colinear beam, which appears to reflect from the nanoparticle sample and transmit through the beamsplitter again, then through the probe's 50/50 beamsplitter, to reach the photodetector, seemingly removing the distinct roles of the pump and probe beams as excitation and measurement beams.

Though the beams are colinear to and from the sample as far as the polarizing beamsplitter, at this point they are again split, so that essentially only the probe beam transmits through the beamsplitter to arrive at the photodetector, while the pump beam is reflected at the beamsplitter along its incoming path, and is not strongly detected. In the beam paths shown in figure 5.6 the polarization is linear and vertical, *i.e.* normal to the surface of the table, or S mode, with the exception of a short distance at the optical isolator, as described in section 5.4.1, and the probe beam following the half-waveplate downstream from the first 50/50 beamsplitter, which rotates the polarization to be parallel to the table surface, or P mode. Unlike a fractional beamsplitter, the polarizing beamsplitter cube is polarization-sensitive, and is aligned so that nearly all incident pump beam power is reflected toward the sample, then reflected again away from the photodetector on its return

path from the sample. Likewise, nearly all the incident P-mode probe power is transmitted through the cube to the sample, then again transmitted to the photodetector on the return path. In attempting to measure the discrimination efficiency of the cube with the pump beam, we found that 91% of the S-mode incident power was reflected by the cube, while the transmitted power was very low and therefore difficult to accurately measure. We suspect that the remaining 9% of the beam power was mostly backreflected at the incoming face of the cube.

The separate functions of pump and probe are maintained by these polarization features. The modulated pump may be considered as modulating the surface temperature of the nanoparticles, inducing a small decrease in the (separate) reflected probe power when the pump is in the 'on' state. However, a small fraction of the pump beam is transmitted by the cube, and reaches the photodetector. Because the first lock-in amplifier is locked to the same modulation frequency of this 'leak-through' pump power, and also since the thermoreflectance effect causes only a small fractional change in probe power, the leak-through contributes an offset which is comparable to the desired probe signal. We decribe correction for this offset in section 5.5 below.

5.4.5 Sample imaging

Our TTR apparatus included sample imaging optics consisting of a magnifying 'telescope' lens pair, a CCD camera, and a glass slide just upstream of the photodetector, to divert a fraction of the probe beam power to the camera (see figure 5.14). The resulting image was used to view the size of the beam spot on the sample or on a substituted mirror, while the sample was being moved along the optical axis and through the objective lens waist on a manual translation stage. The imaged spot size decreases as the waist is approached, and moving the sample to where the minimum spot size is seen places the

sample at the beam waist. The image was also used to simultaneously view the spots on the sample from the pump and probe beams, and to adjust the position of the probe using two-axis rotation of an upstream mirror for maximum overlap of pump and probe spots.

A lens pair in a telescope arrangement, with an object in the focal plane of the first lens, and focal lengths f_1 and f_2, has a magnification of $-\frac{f_2}{f_1}$, with the image located in the focal plane of the second lens. In our experiment, the objective had $f_1 = 20$ mm, and the focusing lens before the CCD had a typical focal length of 15 cm, for a magnification of approximately 7.5, and the beam waist of 6.59 μm after the objective was then magnified to an image of about 50 μm. Our CCD camera had 2.2 μm square pixels, so that the spot image on the CCD would span about 25 pixels or more, and the beam position and size could be resolved and optimized.

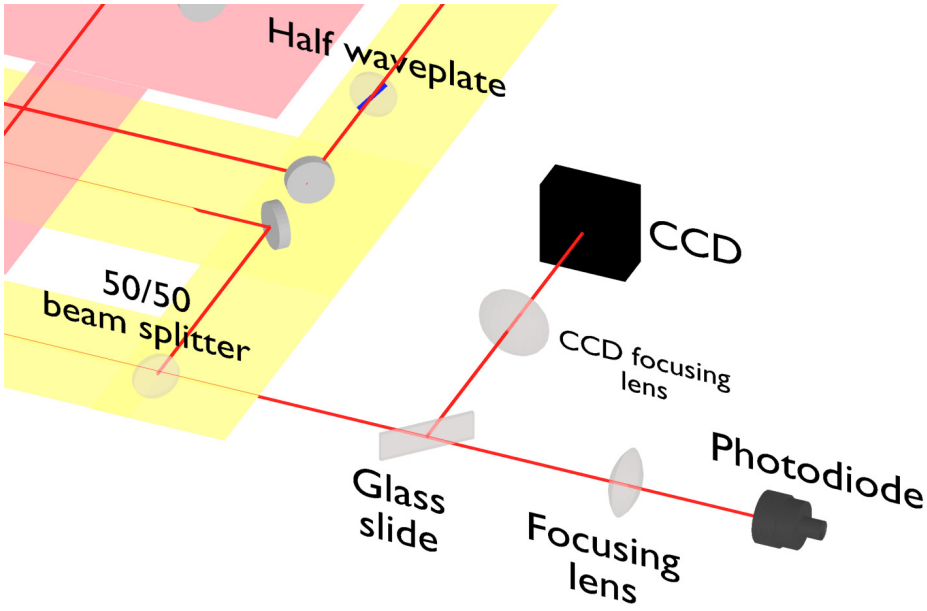

Figure 5.14: Zoomed-in view of the TTR optical layout, showing the imaging components. The objective lens upstream of the sample (not shown in this view, see figure 5.6) is the pair lens to the CCD focusing lens shown, making a 'telescope' pair.

5.4.6 Band-pass filtering

As a final feature of the TTR apparatus, we recall from section 5.4.3 that the pump modulation frequency for final data collection was chosen to be 50 kHz. Prior to final data collection, it was important to have the option to increase the frequency well above this value, to test for the best combination of signal-to-noise ratio and TBR sensitivity. This required frequencies above the bandwidth of 102 kHz of the Stanford 830 lock-in amplifier, which was available and could otherwise have been used as the pump/first lock-in. We therefore used a Stanford 844 RF lock-in for the first stage of lock-in detection, with a range of 25 kHz to 200 MHz. The controller generating the EOM control signal had a bandwidth of 30 MHz, and frequencies up to this value were available. However, the RF lock-in is designed to be a square wave-detecting lock-in, meaning that its output is calculated by mixing the input, presumed to be an RF square wave, with an internally-generated square wave at the detection frequency, so that the output includes contributions from both the fundamental and also odd harmonics of the input. As mentioned in section 5.4.3, the control signal for the EOM modulator of the pump beam was available only as a square wave. While locking into this square wave modulation spectrum would have been effective from a detection point of view, including harmonic contributions would have complicated the theoretical model of the TTR signal, and departed from the typical practice of detection at a single frequency, making comparisons with the results of other studies more difficult.

We therefore required a band-pass filter of the photodetector output, to remove any significant harmonics above the fundamental, and pass only the fundamental to the RF lock-in for mixing, effectively using it as a sine wave-detecting lock-in. We could therefore remain with a single-frequency model of the lock-in signal. We also desired to remove any DC offset from the photodetector output, to aid in keeping the input to the lock-in within its limits. We implemented the bandpass filter in-house as an RC highpass filter followed by

a second-order Butterworth lowpass filter, using a 300 MHz op amp (Analog Devices 8055). The op amp was powered by the output of a voltage regulator (Fairchild Semiconductor LM 317). Using the spectrum analyzer feature of an oscilloscope and a square wave test signal, we confirmed that the amplitude of second harmonic, and higher harmonics, were a small fraction of that of the first harmonic. We also avoided any overload indication at the RF lock-in input by removing most of the original DC offset.

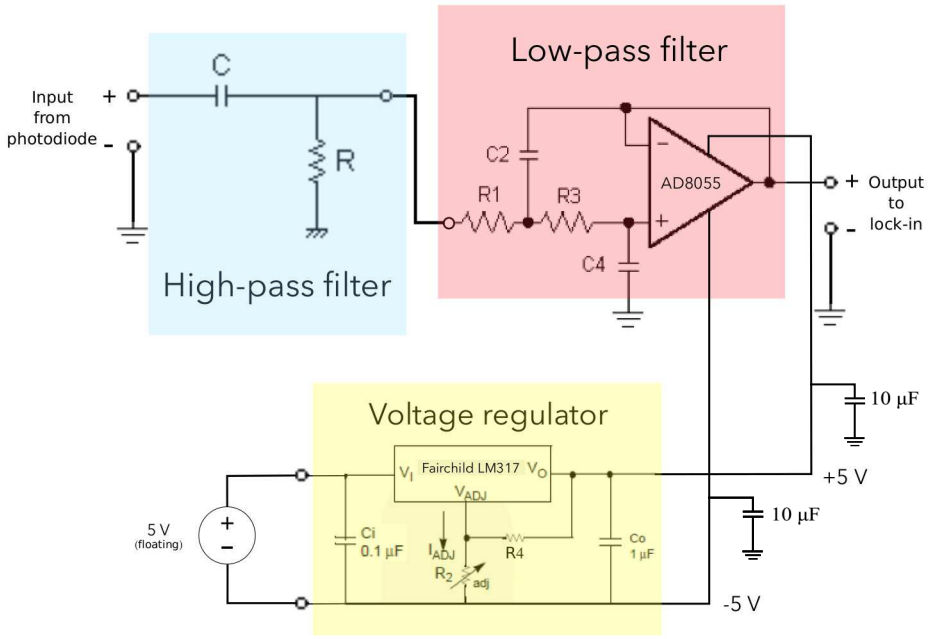

Figure 5.15: The band-pass filter between the photodiode output and the first lock-in input. Filter parameters are listed in table 5.4.

5.5 Experimental results

From figure 5.7, it can be seen that the estimated sensitivity of the TTR signal to the main property of interest, TBR, was somewhat low at 0.078% change in TTR value per 1% increase in TBR value. At this sensitivity, a 1% measurement uncertainty in the

Band-pass filter parameters		
R1	6.8	kΩ
R2	24	kΩ
R3	5	kΩ
R4	3.9	kΩ
C2	330	pF
C4	330	pF
R	47	kΩ
C	3.3	nF

Table 5.4: Component values for the filter shown in figure 5.15.

TTR signal would imply a $\frac{1}{0.07} = 14\%$ uncertainty in the final TBR value. For this reason, it was important to minimize random measurement error as much as reasonably possible, and this was done in two ways: increasing the integration times of the two second-stage lock-in amplifiers to 3 s, to stabilze the signal, and additionally taking multiple scans over the chosen range of probe delays, 100 to 1500 ps, and averaging these scans together. In our final data collection, nine such scans were averaged together, yielding the data plotted in figure 5.19.

An additional step of data processing was required to correct for the arbitrary difference in phase between the photodetector output and the frequency reference (from the function generator controlling the EOM driver). The true phase of the lock-in signal meets the condition[2] that the change in the imaginary part of the signal is zero between times shortly before and after time zero. The difference in our setup is due to the different paths taken by the two signals from the EOM's function generator: the detector output reaches the lock-in by a path consisting of a cable from the function generator to the EOM controller, through its electronics to cables to the EOM itself, an optical path about 1.5 m long, to the detector, and along another cable to the lock-in, while the reference signal is the sync output of the function generator connected to the lock-in directly by a cable.

The RF lock-in has a phase adjustment for this purpose which would have worked equally well to remove the phase difference - in our case, we chose to correct the phase as a data processing step. The phase of all data points was rotated by the same amount to meet the condition above. Figures 5.16 and 5.17 illustrate the phase correction process with a clockwise rotation.

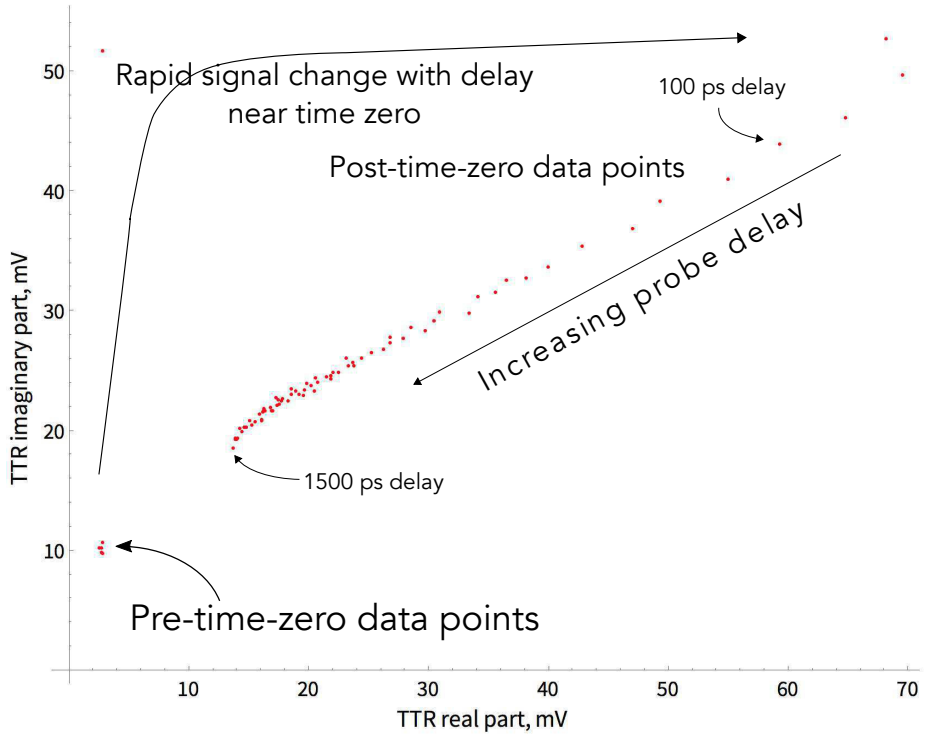

Figure 5.16: TTR data before phase correction.

The final step of data processing was compensation for the effect of the 'leak-through' of pump power through the polarizing beamsplitter to the photodetector, as mentioned in section 5.4.4. In order to assess the magnitude of the offset caused by the leak-through, we measured the signal output, with the sample in place, while blocking the probe beam. The offset proved to be a large value of 85% relative to the TTR signal at 100 ps probe delay

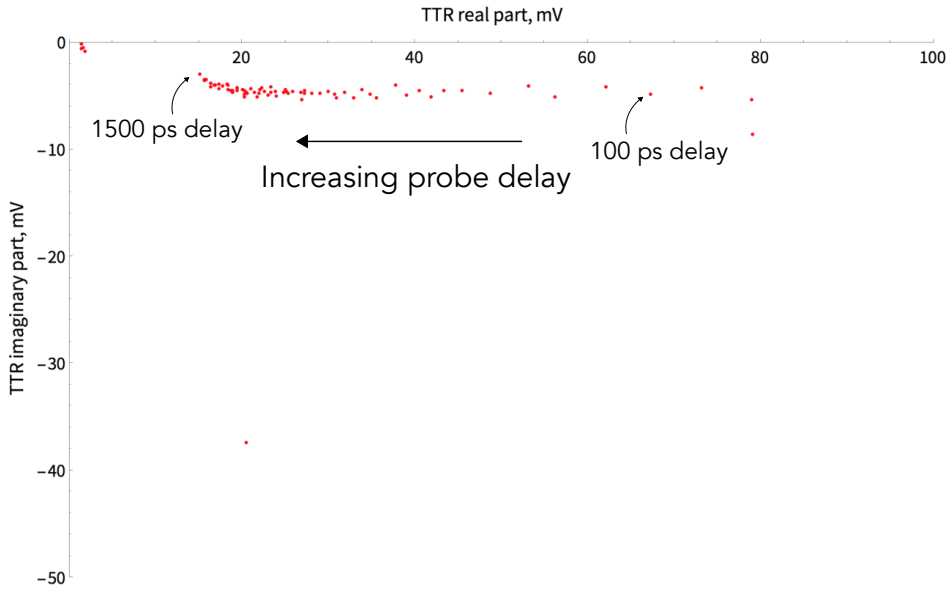

Figure 5.17: TTR data after a phase correction of $-27°$, ensuring that the pre-zero and post-zero imaginary parts are constant.

time. The offset value was constant with probe delay time, and following phase correction, was subtracted from the lock-in output. The remainder of the signal is attributed to the probe beam, the values of which appear in figure 5.19.

Figure 5.19 shows our TTR cooling data (black dots), as well as fits of two models: the multilayer model of section 5.3 (red line), and a single-interface model that considers only the nanoparticle and matrix layers, with TBR at the interface (black line). Experimental and fitted modeling parameters are given in Table 5.5. The fitted parameters were TBC, capping layer thickness, and matrix conductivity. For the multilayer model, greater dissimilarities in both elastic properties and phonon spectra are expected at the metal/organic (Au/citrate) interface, than at the organic/polymer (citrate/pDADMAC) interface, and we model TBR as present only at the Au/citrate interface. Discussion of the significance of these measurements continues in section 5.7.

In addition to improving the quality of the fit to experimental data, the multilayer model leads to measured materials properties which compare much better with literature and expected values. Using the model geometry shown in figure 5.18 and the parameters of table 5.5, we find a fitted TBC of 410 MW/m^{2}K, which is only 17% higher than the value calculated from the diffuse mismatch model,[20] described in section 5.6, from which we find a value of 349 MW/m^{2}K. By comparison, the single-interface model fit gives a near-zero result for TBR at the Au/polymer interface. The fitted value of the capping layer thickness is 7.3 nm. Though we did not find literature values for the conductivity of pDADMAC for comparison, significant porosity may account for its fitted conductivity value of 0.062 W/mK, lying below values for non-porous, pure polymers ranging from 0.1 to 0.6 W/mK.[91]

The parameter values used for fits, listed in table 5.5, include a value for the conductivity of gold which is a bulk experimental value. However, phonon mean-free-paths in gold are comparable to the listed mean nanoparticle diameter of 20 nm: a recent first-principles study[92] places mean-free-paths in the range of 22 to 41 nm for the electron contribution to conductivity in gold. We acknowledge that the actual conductivity is likely reduced significantly from the bulk value. In our particular case of gold nanoparticles embedded in a polymer matrix, the low conductivity of the polymer controls the cooling dynamics, and we assumed that our model is insensitive to the conductivity value used for the gold particle, which remains in internal equilibrium during diffusion in the adjacent polymer. To confirm this, we calculated the TTR signal over the probe delays plotted in figure 5.19 with both the listed gold conductivity, and a value reduced by 50%. The difference between the two cases was less than one part in 10^3 relative to the curve found using the bulk value of conductivity, confirming minimal sensitivity of the model to nanoparticle conductivity in this case.

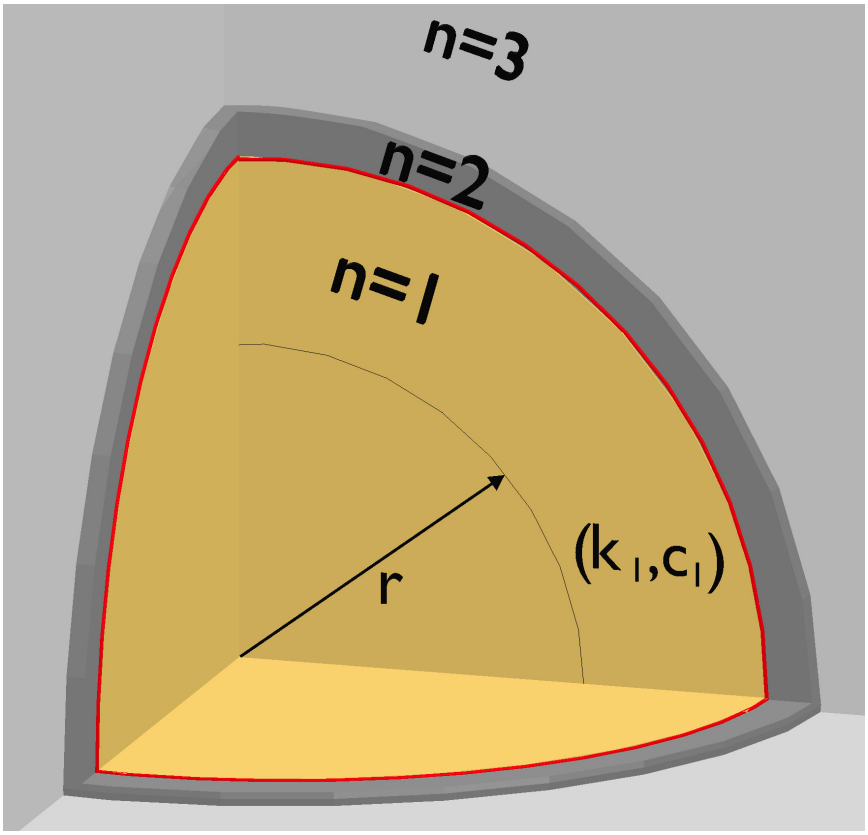

Figure 5.18: Model geometry for fitting to nanoparticle cooling TTR data. The Au particle is layer 1, the citrate capping layer is 2, and the polymer matrix is layer 3. Surface heating is shown at the boundary between layers 1 and 2. Each layer i has thermal conductivity k_i and specific heat c_i, given in table 5.5.

Final TTR data was collected in a series of nine scans and averaged, as described in section 5.5.1, with an overall uncertainty of 0.9% (see section 5.5.1). To quantify the effect of this uncertainty on the precision of the fitted TBC value, we utilize the multilayer model to plot the sensitivity of the TTR signal to TBC in figure 5.20. The multilayer model was fitted to data over the range 100 to 1500 ps probe delay, and we therefore select the delay time which places the greatest restriction on the TBC value at the maximum of 0.078% at 275 ps. We find a TBC uncertainty of $\frac{0.9\%\text{TTR}}{0.078\%\ \text{TTR}/\%\ \text{TBC}} = 12\%$, and report our TBC result as 410 $\text{MW/m}^2\text{K} \pm 12\%$.

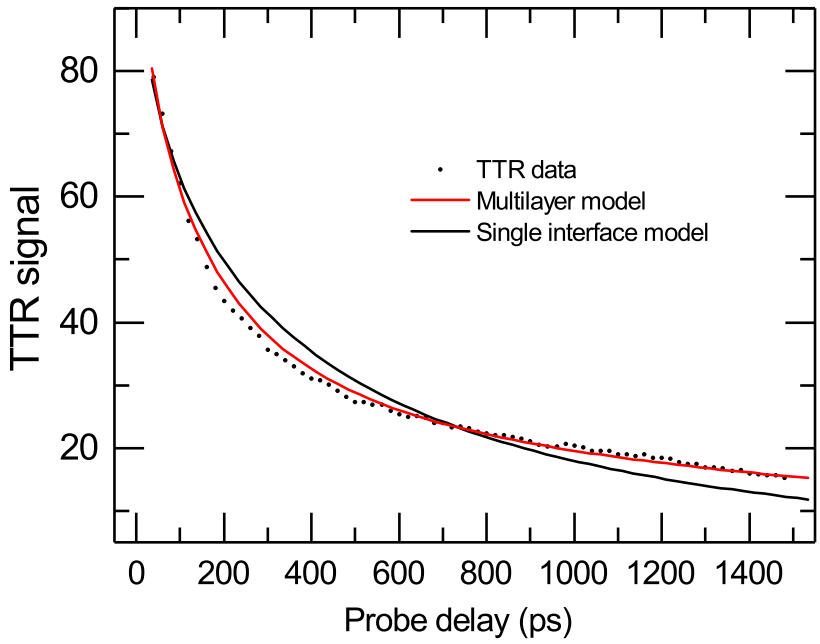

Figure 5.19: TTR data (black dots) with multilayer and single-interface fits (red and black lines, respectively) for polymer-embedded Au nanoparticles. The multilayer model shows an improved fit ($R^2 = 0.994$) over the single-interface model ($R^2 = 0.947$). The small amplitude oscillations, with period 106 ps, are possibly due to acoustic wave reflection in the nanoparticle and capping layer. The multilayer fitted value of TBC is 410 MW/m^{2}K, while the single-interface model fit gives a misleading nearly-zero value for TBR.

5.5.1 Experimental uncertainties

Figure 5.21, which plots the average of nine TTR scans, includes the estimated random error of the TTR signal as a function of delay time. The random error was calculated as the standard deviation of the signal value of the nine scans at each delay time. The average relative uncertainty over all delay times is 3.8%, and the average uncertainty of the mean is 0.9%. Relative uncertainties refer to the mean signal value at each delay time.

These uncertainties are judged to be acceptably low (see the discussion in section 5.5). We attribute the low error to the reduction of noise by the dual lock-in amplifier

Experiment parameters			
Model inputs			
Repetition rate	ω_s	$2\pi \cdot 76.3$	Mrad/s
Pump modulation frequency	ω_0	$2\pi \cdot 50$	krad/s
Probe modulation frequency	ω_{pr}	$2\pi \cdot 500$	rad/s
Beam width	w	6.59	μm
Nanoparticle radius	a	10	nm
Au thermal conductivity[87]	k_1	318	W/mK
Au volumetric specific heat[87]	c_1	$2.49 \cdot 10^6$	J/m^{3}K
Au longitudinal acoustic velocity[38]	$v_{Au,l}$	3240	m/s
Au transverse acoustic velocity[38]	$v_{Au,t}$	1200	m/s
Au Debye frequency[38]	ω_{Au}	$2.23 \cdot 10^{13}$	rad/s
Citrate thermal conductivity[89]	k_2	0.1353	W/mK
Citrate volumetric specific heat[93]	c_2	$1.82 \cdot 10^6$	J/m^{3}K
Citrate longitudinal acoustic velocity[89]	$v_{cit,l}$	1653	m/s
Citrate transverse acoustic velocity[94]	$v_{cit,t}$	827	m/s
Citrate Debye frequency[95]	ω_{cit}	$1.96 \cdot 10^{13}$	rad/s
Polymer volumetric specific heat[91]	c_3	$1.1 \cdot 10^6$	J/m^{3}K
Model outputs			
Thermal boundary conductance (fitted)	1/R	410	MW/m^{2}K
Capping layer thickness (fitted)	$r_2 - r_1$	7.3	nm
Polymer thermal conductivity (fitted)	k_3	0.062	W/mK

Table 5.5: Experimental and modeling parameters for polymer-embedded gold nanoparticles. In the absence of a literature value for the specific polymer pDADMAC, the specific heat is an estimate taken from typical polymer values. See section 5.6 concerning the acoustic velocities and Debye frequencies.

configuration. Also, the function generator driving the pump beam's EOM modulator controller was selected for its frequency stability. To attempt to identify sources of noise, we consider the fluctuating power of the pump and probe beams, and noise generated in the bandpass filter and lock-in amplifier electronics. We find that the larger contributor is likely to be noise generated by the pump's lock-in. Beam power data was collected automatically during TTR scans from a power meter (not shown in figure 5.6) which was connected to the auxiliary input of one of the lock-ins for the probe beam. The typical uncertainty in the beam power is approximately 0.9%. This value happens to be essentially the same as our uncertainty in the average TTR signal, when averaged over nine repeats.

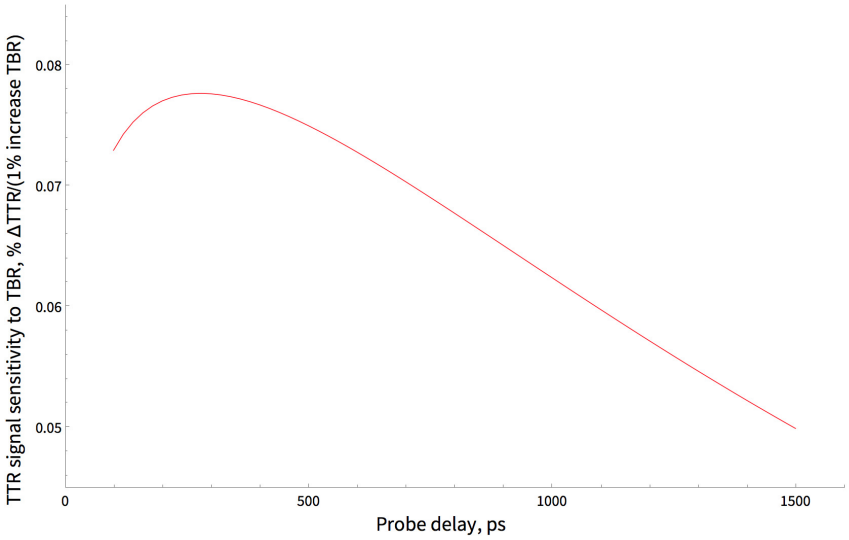

Figure 5.20: Sensitivity of the TTR signal to changes in TBC. The greatest sensitivity occurs at 275 ps, with a value of 0.078%/(% change in TBC).

For the case of the pump lock-in, its noise is estimated by

$$(input\ noise)\,\sqrt{ENBW}\,(gain), \tag{5.35}$$

where $ENBW$ is the bandwidth of an ideal step edge low-pass filter which would generate the same noise as the lock-in's low pass filter. With the parameters in table 5.2, the ENBW is 2.5 kHz, and the lock-in input noise specification is 6 nV/$\sqrt{\text{Hz}}$. The gain is automatically set by the lock-in to give an output of 10 V for a full-scale input, so gain was 10/100mV for a gain of 100, giving an rms noise value of 30 μV. The output of the pump lock-in was on the scale of the sensitivity setting of the probe lock-in of 1 mV, so the pump lock-in noise was near 3% of the output signal. This is a relatively high noise value for a well-adjusted lock-in, and is due to a requirement of the dual-lock-in configuration: the time constant was set to a low value to ensure that the pump lock-in had a response time (about $5 \cdot (time\ constant) = 0.5$ ms) which was smaller than the period of the probe modulation ($\frac{1}{500\ \text{Hz}} = 2$ ms). This low time constant gives a higher ENBW, increasing the output noise.

However, the overall result of the dual lock-in arrangement was acceptably low noise in the measured TTR signal.

The probe lock-ins were run at long integration times of 3 s for greater noise reduction. This long time constant reduces the ENBW relative to the pump case. For greater resolution of the collected amplitude and phase data, the probe lock-ins' sensitivities were set slightly above the input level, causing the automatic gain to be higher than the pump case. Despite the greater gain, with the narrow bandwidth setting, the probe lock-ins generate noise of less than 0.1% of the output. Combining the beam power and pump lock-in uncertainties as independent random errors, the result is 3.1% uncertainty, near the observed value of 3.8%. This method of adding uncertainties, as well as the identification of beam power and pump lock-in as the greatest noise sources, was not tested systematically. For example, the pump lock-in gain could have been doubled in a controlled experiment, and the effect on the measurement uncertainty observed. The near agreement of the estimated uncertainty with the observed uncertainty suggests that the two largest error sources have been identified. Other possibilities are breathing modes in the nanoparticles, as seen in figure 5.19, vibrations of the sample and optics, and variance in the timing of probe pulses following pump pulses.

5.6 Comparison with diffuse mismatch model prediction

Section 3.2 describes the DMM[20] as a theory which best predicts TBC at interfaces between dissimilar materials, and as such we employ it to evaluate our TTR experimental result for the Au/citrate TBC of 410 $MW/m^2K \pm 12\%$. The inputs to this model are the acoustic velocities and Debye frequencies in table 5.5. For the measurement of acoustic velocities in solids, both the transient pulse method,[96] as well as calculation from the measurement of the frequency of standing waves, continue to be chosen methods for accurate

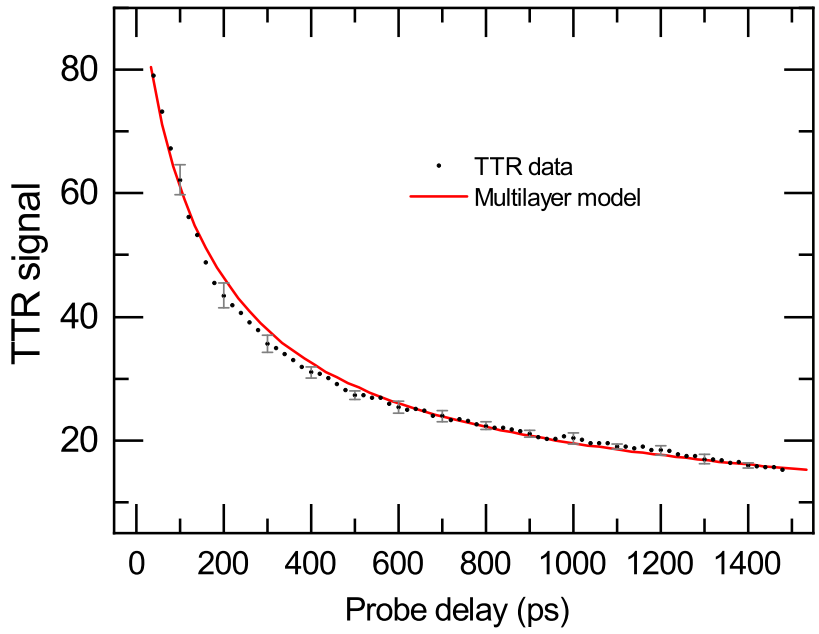

Figure 5.21: TTR data with measured error. The data points are the averages of nine scans, while the error bars show the standard deviation calculated from the nine scans.

measurement, and provide our values for the two vibration modes of gold. For citrate, we referred to published ultrasonic velocimeter measurements for the longitudinal acoustic velocity.[95] For the transverse acoustic velocity of citrate, in the absence of a literature value, we estimate it as 50% of the longitudinal acoustic velocity.[94] Debye frequencies are found from literature Debye temperatures by $\hbar\omega_D = k_B T_D$.[38,97] In reference 38, the Debye temperatures were obtained by adjusting the value so that the specific heat in the quantum harmonic model of the solid, using the Debye approximation, matches the observed specific heat.

From these parameters, we calculate a TBC value of 349 $\mathrm{MW/m^2K}$ from the DMM, using eqs. 3.18, 3.19, and 3.21. Uncertainty in the DMM value is due to uncertainties in the input parameters, and although these are not known, we estimate the DMM value uncer-

tainty by considering the change in the value if the acoustic velocity of citrate, perhaps the least certain input, were uncertain by (at least) 10%, in the absence of measurements. We find that the DMM result changes by 6%, for a DMM TBC result of $349\,\mathrm{MW/m^2K} \pm 6\%$. Our experimental value was $410\,\mathrm{MW/m^2K} \pm 12\%$. The DMM result of $349\,\mathrm{MW/m^2K}$ value is 15% lower than the experimental value of $410\,\mathrm{MW/m^2K}$, and is below the experimental uncertainty range by 3%. However, the uncertainties overlap by 2% of the experimental value. Considering uncertainty in the DMM value due to the use of the Debye approximation, and the use of literature values, rather than measurements, for some parameters, this is good agreement between the DMM and the measured value. From the AMM model described in section 3.2.2, we calculate a TBC of $9.5\,\mathrm{MW/m^2K}$, a small fraction of the experimental value. Park[86] *et al.*, in a rare structural study of the adsorbtion of citrate anions to the surface of Au NPs, find that three different configurations of anions bond to the Au surface, and that their configurations also vary between whether the exposed Au face is the (111), (110), or (100) surface. This variety of configurations implies significant disorder at the Au/citrate interface and a high rate of diffuse phonon scattering, and is consistent with the good agreement of the DMM prediction with measurements.

5.7 Conclusions

This chapter on nanoparticle studies has described the design and implementation of our TTR experiment for measuring the TBR of gold nanoparticles, and the development of the spherical multilayer model required to calculate the TBR value from measurements. Having quantified measurement uncertainties, our experimental result lies slightly above the value predicted by the DMM, and the DMM prediction is 3% below the experimental uncertainty range. The best way to reduce measurement error would be by enclosing the experiment, thereby stabilizing beam powers and pointing. On the theoretical side, more

accurate material parameters for the DMM could improve the agreement between theory and experiments. We have also discussed the Debye approximation as the most significant source of theoretical discrepancy,

Beyond considerations of agreement, our results indicate that phonon scattering at the Au/citrate interface is diffuse. The estimate of the (specular) AMM lies far below the measured TBC, as it does for other material pairs. The approximate agreement we see in these results confirms, as an underlying concept of the DMM, that diffuse transmission channels not accounted for in the specular picture contribute heavily to conduction at the interface.

Chapter 6

Membrane Systems

6.1 Extending existing TTR studies of metal films on insulating substrates

Though TTR is established as one of the primary tools for exploring and measuring thermal properties at the nanoscale,[5] it continues to rely on certain assumptions which may be reasonable, but which are unconfirmed in some cases. One of its successes has been the accurate measurement of reduced thermal conductivity in planar thin films approaching nanoscale thickness.[98] However, such experiments have been carried out with films deposited on substrates with large thicknesses, relative to film thickness. Any transport occurring in the substrate is assumed to take place in substrate regions very close to the thin film, within a substrate depth on the order of the film thickness. Also, in order to calculate results from a TTR signal - for example, the thermal conductivity of the film - models generally assume that thermal transport is diffusive in character.

To test the assumption of near-film diffusion, we have applied the TTR method to a structure which consists of a thin metal film deposited on a thermally insulated membrane.[99] In a system in which significant cooling occurs in the substrate far from the film, relative to the film thickness, a model should underestimate the actual cooling time in our thin-substrate system. In a system with cooling occurring ballistically, our diffusive model

should again underestimate the actual cooling time. Our initial results agree with the assumptions of near-film substrate transport, and diffusive transport: we observe a cooling time comparable to the estimated time of 1900 ps, and film conductivity results comparable to that observed in the same structures by means of the thermal isolation method. To fully confirm these result, we suggest further experiments to accomplish the additional task of removing any bridge-to-air conduction by performing experiments in a vacuum.

6.2 Multilayer planar diffusion and TTR signal model

Our thermal model is an accepted diffusive, multilayer model of the TTR signal similar to that used in section 5.3.[78,80] The planar model of Schmidt *et al.*[80] is directly applicable to the thermal isolation platform system, if the assumption of zero transport from bridge to air is made. In this model, the multilayer structure is again handled by means of the transfer matrix method - however, instead of the thermal wave formulation of Feldman,[78] temperatures within the system are represented by $2 \cdot 1$ column vectors with temperature as the upper element, and flux as the lower. The model also distinguishes between the in- and cross-plane thermal conductivities k_{ri} and k_{zi} of a layer i by applying a Hankel transform to the frequency-domain heat equation. The temperature/flux vector at the bottom of the n-layer system system is then related to that of the top by

$$\begin{pmatrix} \theta_b \\ f_b \end{pmatrix} = \mathbf{M}_n \, \mathbf{M}_{n-1} ... \mathbf{M}_1 \begin{pmatrix} \theta_t \\ f_t \end{pmatrix} = \mathbf{M} \begin{pmatrix} \theta_t \\ f_t \end{pmatrix}, \tag{6.1}$$

$$\mathbf{M} = \begin{pmatrix} A & B \\ C & D \end{pmatrix}, \tag{6.2}$$

and with each layer matrix given by

$$\mathbf{M}_i = \begin{pmatrix} \cosh q_i d_i & -\frac{1}{k_i q_i} \sinh q_i d_i \\ -k_i q_i \sinh q_i d_i & \cosh q_i d_i \end{pmatrix}, \tag{6.3}$$

with

$$q_i^2 = \frac{k_{ri}k^2 + i\omega c_{pvi}}{k_{zi}}, \tag{6.4}$$

where k is the transform variable, and c_{pvi} is the isobaric, volumetric specific heat of layer i. The top temperature is determined by the zero bridge-to-air transport condition $f_b = 0$, giving

$$\theta_t = -\frac{D}{C} f_t, \tag{6.5}$$

for a fixed value of k. The real-space temperature $H(\omega)$, the inverse transform of θ_t,

$$H(\omega) = \frac{A_0}{2\pi} \int_0^\infty k \left(-\frac{D}{C}\right) e^{\frac{-k^2w^2}{8}} \tag{6.6}$$

with heating A_0 and beam width w, is substituted into eq. 5.26 for the TTR response. The heating A_0 is treated as a free parameter, and the film conductivities $k_{r,z0}$ are determined as fitting parameters. Values for model parameters are listed in table 6.1.

Lastly, we use the planar model to estimate the sensitivity of the measured signal to the values of any fitted thermal parameters, in order to select a pump modulation frequency with the greatest sensitivity, and least uncertainty in fitted values. Figure 6.1 shows the TTR signal $-\frac{\mathrm{Re}\, Z}{\mathrm{Im}\, Z}$ sensitivity plotted as a function of modulation frequency. As in section 5.5, the sensitivity is defined as the signal percent change per percent change in the parameter. We choose 1 MHz as the experimental modulation frequency, a value which retains high sensitivity to all three of in- and cross-plane film conductivity, and film/substrate thermal boundary resistance,

6.3 Design of thermal isolation structure experiment

6.3.1 The thermal isolation platform

The thermal isolation platform[99,100] is designed to enable experiments which directly measure the thermal conductivities of thin films of controlled thickness. The platform is

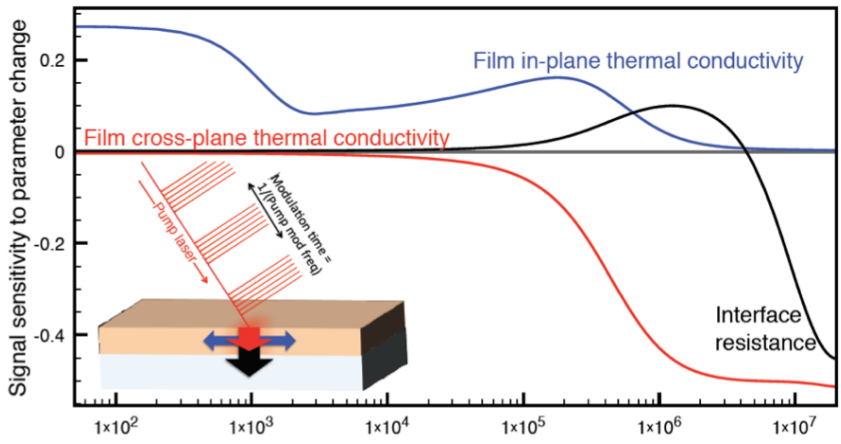

Figure 6.1: The sensitivity of the TTR signal to thermal parameters of in- and cross-plane film conductivity, and film/substrate thermal boundary resistance.

designed, fabricated, and characterized by our collaborators of the Zink research group at the University of Denver, for whose support and assistance we are grateful. Platform parameters are listed in table 6.1. The platform's essential feature is its structure of thin metallic or insulating films coated on suspended, thermally-insulated silicon nitride (Si-N) membranes (see figure 6.2). The thermal isolation and small thickness of the Si-N underlying the coated film enables the sensitive measurement of the thermal conductance of the coating, which would otherwise be indistinguishable from the large conductance of a thick substrate. The membrane structure is accomplished by a KOH back-etch of the Si substrate supporting an original 500 nm Si-N coating. The membranes make thermal contact at each end with larger island structures, themselves suspended by Si-N legs, and experiments are performed in vacuum. A controlled temperature at one island is obtained by joule heating in a conductor lithographically patterned on the island, while a similar conductor acts as a thermometer measuring the resulting temperature on the opposite island. From known specific heats, dimensions, and input power, the film thermal conductivity can be calculated. The platforms have been successfully used for a number of experiments, including

transport by long-wavelength phonon modes near room temperature,[100] measurement of the conductivity of the suspended Si-N membranes themselves,[99] and observation of the planar Nernst effect.[101]

Thermal isolation platform TTR Dimensions and model parameters			
Bridge length		800	μm
Bridge width		35	μm
Mo coating thickness	d_0	200	μm
Mo specific heat	c_0	0.251	J/gK
Mo mass density	ρ_0	$10.28 \cdot 10^6$	g/m^3
Si-N thickness	d_1	500	μm
Si-N conductivity	k_1	3.0	W/mK
Si-N specific heat	c_1	0.40	J/gK
Si-N mass density	ρ_1	$3.2 \cdot 10^6$	g/m^3
Beam spot size	w	2.71	μm

Table 6.1: Parameters of the thermal isolation platform and thermal model used in TTR experiments.

6.3.2 TTR experiment implementation

The TTR experiment optical layout for bridge structure studies was the same as shown in figure 5.6, and has parameters listed in table 6.2. The bridge structure was mounted on a two-axis manual translation stage, with axes normal to the optical axis, for positioning relative to the beams. The location of the pump and probe beams on the structure was imaged with a CCD as described in section 5.4.5, using long exposure times, and with the addition of a green 532 nm laser focused on the structure for illumination, incident at approximately 45° from the optical axis. Figure 6.3 is a typical image of the thermal isolation structure, showing the illumination laser incident from the left, and the white reflection of the pump and probe beam spots. Note that the long CCD exposure causes the beams to appear to have a greater width than that listed in table 6.2. A section of an island component is visible in the lower portion of the image.

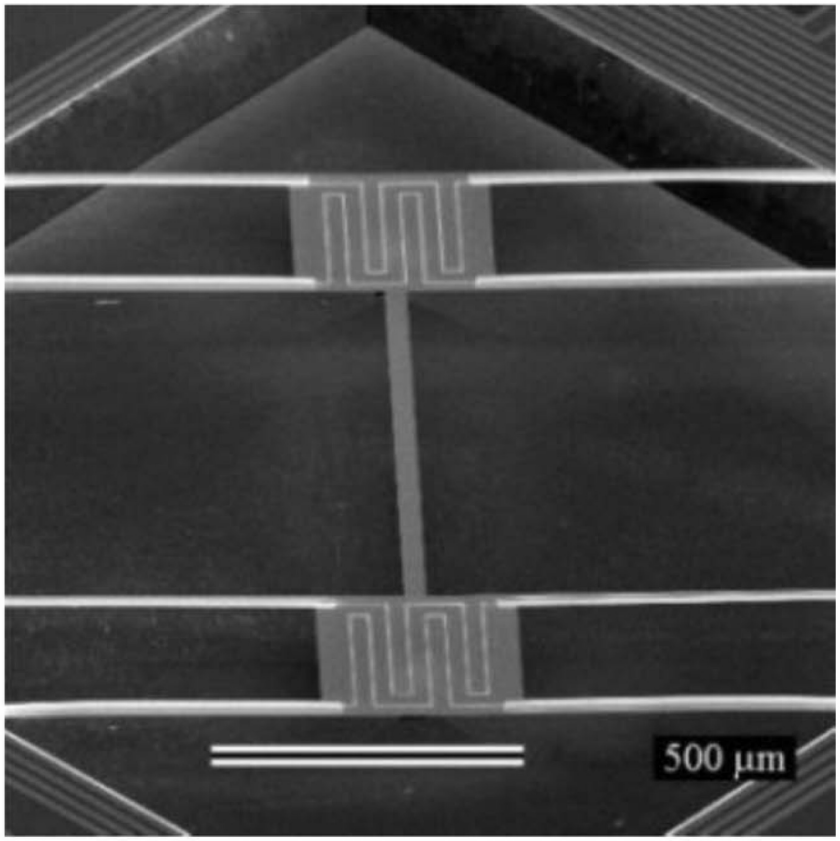

Figure 6.2: SEM image of the thermal isolation platform, provided by our collaborators of the Zink research group at the University of Denver.[99] The Si-N bridge has length 800 μm, thickness 500 nm, and is coated with a Mo film of 200 nm thickness. The island components have dimensions $250 \cdot 250\,\mu\mathrm{m}^2$.

The pump beam power required for a 1 K temperature gain in the Mo film is calculated in a similar way to that described in subsection 5.4.2. An expression for the pump arm power has the same structure as eq. 5.32,

$$\begin{aligned} P_{inc} &= \frac{(\text{heat capacity})(\text{temperature gain})(\text{frequency})}{1-\mathrm{R}} \\ &= (\text{heat capacity})\,\frac{\Delta T\, f_{rep}}{1-\mathrm{R}}, \end{aligned} \tag{6.7}$$

where again $\Delta T = 1\,\mathrm{K}$ and $f_{rep} = 76.3\,\mathrm{MHz}$. For the heat capacity we use the volumetric specific heat of Mo times the volume of a right cylinder with diameter equal to the e^{-2} beam

width, and height equal to the optical penetration depth ζ_o of Mo, found from $\zeta_o = \frac{\lambda}{4\pi k}$,[46] where the wavelength $\lambda = 800\,\text{nm}$, and the imaginary part k of the complex refractive index $\tilde{n} = 3.653 + i\,3.357$[102] at 800 nm. We find the reflection coefficient at normal incidence R from the Fresnel equation

$$\mathrm{R} = \left|\frac{1-\tilde{n}}{1+\tilde{n}}\right|. \tag{6.8}$$

The final power reads

$$P_{inc} = \pi\left(\frac{w}{2}\right)^2 \zeta_o c_{pv} \frac{\Delta T\, f_{rep}}{1-\mathrm{R}}. \tag{6.9}$$

With these values and those in tables 6.1 and 6.2, we find a pump power of 0.24 mW for a 1 K temperature gain of the Mo film. In experiments, a pump beam power of 3.5 mW, stepped down with an ND 1 filter to 0.35 mW, was used for final data collection, for an acceptably low temperature gain between 1 and 2 K. Probe beam power was usually set to half the pump beam power.

Thermal isolation platform TTR Optical parameters			
Pump beam power		0.35	mW
Probe beam power		0.18	mW
Beam spot size	w	2.71	μm FWHM
Pump modulation frequency	ω_0	1	MHz
Probe modulation frequency		500	Hz
Objective lens focal length		9	mm
Lock-in integration time		1	s
Lock-in sensitivity		10	μV

Table 6.2: Optical parameters of the TTR thermal isolation platform experiment.

6.4 Experiment results

Data from initial TTR scans are shown in figure 6.4, and a subset of the data points, selected for clarity, are shown in figure 6.5. These scans were taken with the pump and probe beam powers varying by a factor of up to $10^{1.6} \approx 40$. The lock-in amplitude results

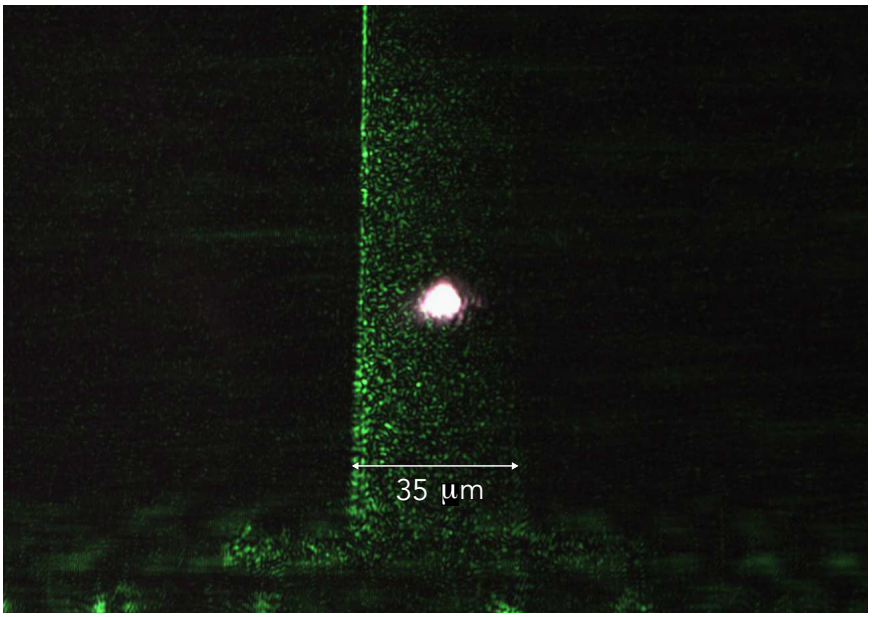

Figure 6.3: CCD image of the thermal isolation platform positioned in the pump/probe beam. In the lower part of the image, a portion of an island structure scatters the green illumination laser.

were scaled upward by the same downward factor of ND filtering of the beam powers, so that *e.g.* with downward filtering of $10^{-0.6} \approx 0.25$, the amplitude values were mathematically scaled upward by $10^{0.6} \approx 4$ for comparison between scans. These results show us that the signal is strongly dependent on the probe pulse delay time, with a cooling time of about 800 ps, so the signal must be responding to the thermal cooling process in the Mo film surface, rather than originating as an unwanted signal, such as pump leak-through or scatter at the pump modulation frequency. The scaled values vary by a factor of approximately 2 or less, while the incident powers vary by a factor of 40, with consistent cooling times, indicating that thermal parameters, including the Mo thermoreflectance coefficient are at most weakly dependent on the incident beam power and film temperature. We expect these behaviors in a correctly functioning TTR measurement, and can reasonably interpret the TTR signal as proportional to the film surface temperature.

We use a separate series of measurements shown in figure 6.6 to investigate the effect of substrate thickness, and for the determination of the Mo film conductivity. The spot location was moved from the lengthwise center of the bridge structure toward one of the islands, with other parameters remaining constant. The positioning of the Mo surface at the beam waist, and the overlap between pump and probe spots, were optimized with each TTR scan. The multilayer TTR signal model of section 6.2 was fit to each scan, with the heating power as a free parameter, and the Mo thermal conductivity as a fitting parameter, with the results shown in the figure inset, varying from 77 to 85 W/mK. By comparison, a value of 55.1 W/mK,[99] at room temperature was measured using the thermal isolation method, for a similar 200 nm Mo film sputtered on the bridge structure surface, and measured in a vacuum environment.

The higher value from our TTR measurements could be due to an additional cooling channel of bridge-to-air conduction which was not included in the model of cooling. TTR experiments are normally done with samples in air, with the assumption that the transport channel of conduction from an excited layer to adjacent lower and substrate layers greatly outweighs any excited layer to air transport. With a relatively thick substrate present to act as a cold reservoir, thereby supporting heavy transport through this channel, the assumption is reasonable. However, in our film-on-membrane experiments, without a thick substrate serving as a reservoir, transport could be significantly less, making excited layer to air conduction visible against the excited layer to thin substrate background. Including this additional conduction would decrease modeled cooling times, and the fitted Mo conductivity would also then decrease for the modeled cooling time to match observations, decreasing the difference between the TTR and thermal isolation results.

An alternative explanation for the difference in conductivities is the age of the Mo film at the time of measurements, and likely significant oxidation of the film. With a scale

on the order of 100s of nm, and pulse absorption and heating occurring at the upper Mo film surface, cooling dynamics in TTR measurements are controlled primarily by diffusion in the Mo film. Oxidation would increase the heat capacity of the Mo layer and increase cooling times. The sample preparation procedure described in nuclear resonant scattering experiments[103] explains that, in order to limit the thickness of a forming native Fe-oxide layer to several nm, Fe films could be exposed to ambient air for controlled times. It is therefore reasonable that oxides have formed through a large part of the depth of the long-exposed Mo film of our experiments. Mo has two prevalent oxidation states, MoO_2 and MoO_3. X-ray photoelectron spectroscopy studies[104] of Mo films indicate that while MoO_3 is predominant in oxidized crystalline films, amorphous films, as in our studies, contain both oxides. The effect of increasing oxidation on the volumetric specific heat of Mo, the form which appears in the multilayer model, in shown in table 6.3, where specific heat increases significantly with oxidation. Using a higher heat capacity in the model would raise the fitted conductivity for the modeled cooling time to match observations, increasing the already-large difference between the TTR and thermal isolation conductivity values. An analysis of the sensitivity of the cooling time to Mo heat capacity would gauge the importance of characterizing oxidation in the Mo film.

Molybdenum and its oxides					
	Specific heat, $J/mol\,K$	Mass density, $10^6\,g/m^3$	Molecular weight, Da	Specific heat, $10^{-8}\,J/m^3\,K$	Relative specific heat, to Mo
Mo	24.06	10.28	95.95	2.44	1.0
MoO_2	55.88	6.47	127.94	6.75	2.8
MoO_3	75.00	4.70	143.95	11.09	4.5

Table 6.3: Specific heat and mass density comparison between Mo and its oxides. Specific heats in the last column are relative to the volumetric value for Mo in the fifth column. Values are taken from references 87 and 93.

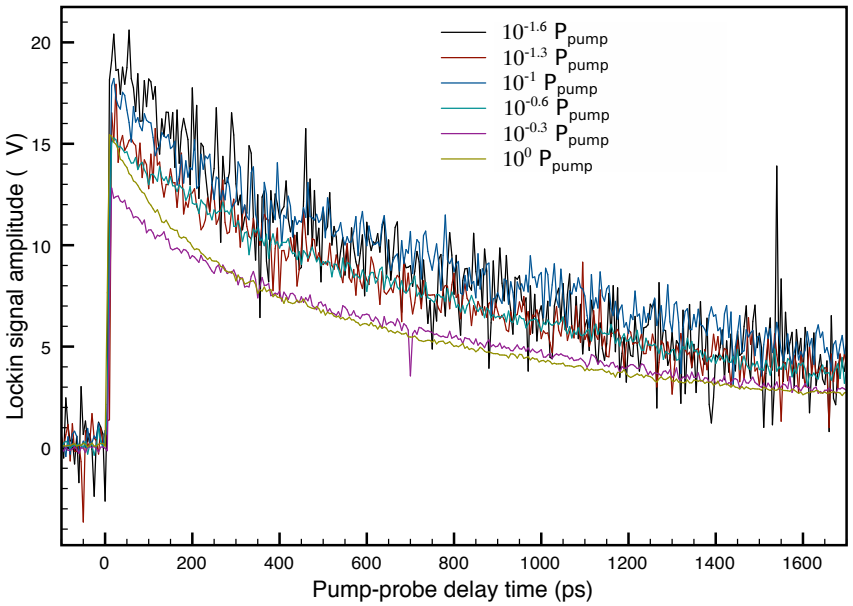

Figure 6.4: TTR data from the center location of the bridge structure, with a 200 nm thick Mo film. Pump power has been stepped downward from the original value P_{pump} by the factors shown, and the resulting signal was scaled upward by the same factor for comparison between powers. The signal uncertainty is seen to increase with decreasing pump power.

6.5 Conclusions

For the amorphous Si-N substrate of these experiments, literature[100,105] methods of estimating the mean-free-path of phonons places the value at a relatively small 0.6 nm at room temperature. This value would place thermal dynamics firmly in the diffusive regime, and is implicit in the hypothesis that cooling dynamics would be identical between experiments with substrates at the 500 nm thickness, as in our studies, and those with very thick substrates. In this picture, no significant transport occurs far from the film/substrate interface, *i.e.* at distances much greater than the film 200 nm thickness. Significant macroscale transport by modes with mean-free-path much longer than our 500 nm substrate thickness would produce measurements on our membrane structure with cooling times longer than those of our diffusive model, which assumes zero thermal flux at the lower surface of the

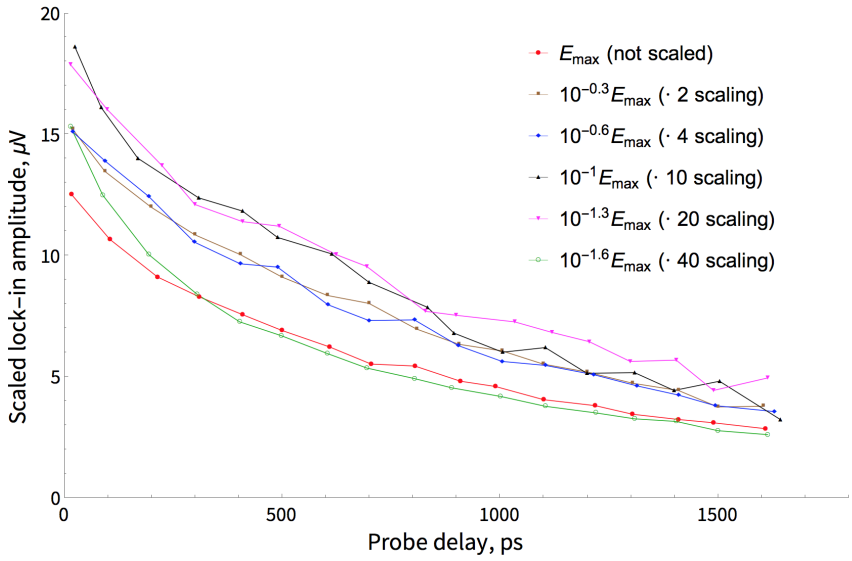

Figure 6.5: A subset of TTR bridge structure data selected for clarity from figure 6.4, with points chosen from near the mean value of the original signal. The cooling time is seen to be consistently about 800 ps.

substrate. The agreement between the model and measurements suggests that diffusion is indeed occurring near the film/substrate interface.

However, the mean fitted value of Mo film conductivity was 81 W/mK, 47% above the value of 55 W/mK obtained with thermal isolation measurements,[100] and the same studies show that long mean-free-path modes, of length up to 3 μm, contribute significantly to transport and to this conductivity value. Performing TTR measurements with bridge structures in vacuum would increase observed cooling times, and decrease fitted conductivities. A fitted conductivity less than 55 W/mK could be independent evidence of long mean-free-path contributions to transport.

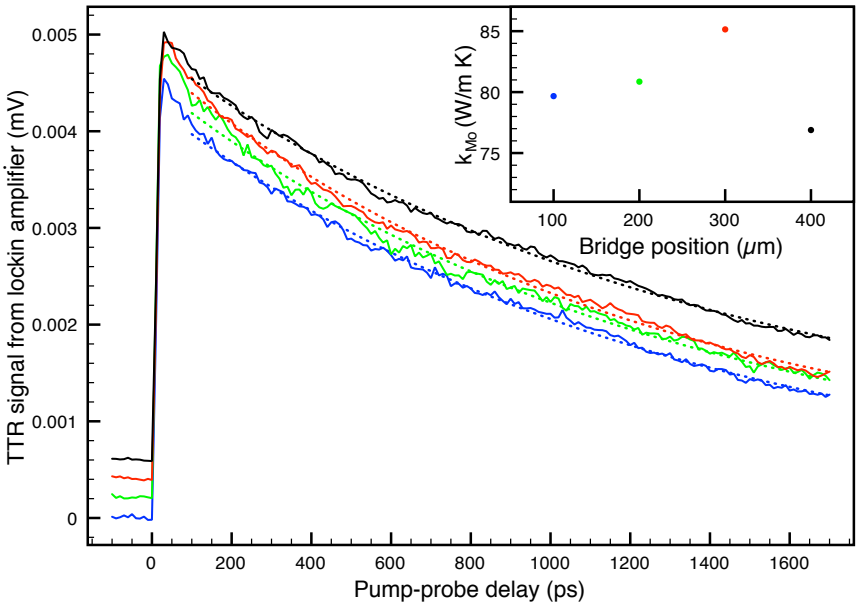

Figure 6.6: Bridge structure data from successive points along the length of the structure, and centered transversely. Positions are measured from the edge of the island component at one end of the bridge. Fits of a diffusive model yield the Mo conductivities shown in the inset. The total length of the bridge is 800 μm. Data have been shifted upward for clarity.

Chapter 7

Nanoparticle Optical Properties

7.1 Introduction

The exciting nanoparticle applications of *chemical sensing* and *biosensing* utilize the sensitivity of nanoparticle absorption of visible light to changes in the surrounding medium, such as the arrival of an organic compound of interest.[74] Plasmon resonance is the oscillation of electrons in response to an external electromagnetic field, either in a plasma, or in the electron gas of a solid, as in our case of gold nanoparticles. The oscillation occurs throughout the bulk of the material, and is coherent and collective among the electrons. In the case of light propagating through air, or another dielectric material, and impinging on the surface of a solid, *surface plasmon resonance* (SPR) occurs as the incident wave induces surface waves of periodically-varying electron density, which propagate along the surface of the solid.[106] SPR is the interaction between incident photons and quanta of electron polarization (*plasmons*) to form the hybrid quasiparticle state of *surface plasmon polaritons* (SPPs). SPPs exist only within the optical penetration depth of the solid, but in some metals can propagate along the surface tens of nm before scattering or absorption occurs. *Localized* surface plasmon resonance (LSPR) describes SPR in the case of nanoparticles of sub-wavelength size, which confine SPPs to within the particle's surface, producing a sharp absorption peak in the visible spectrum.

Small changes in the medium refractive index can shift the LSPR wavelength,[61,62] and the shift is measurable with conventional equipment, such as a UV/visible spectrometer. This is one way of enabling the diagnostic method of chemical sensing,[68] which is especially useful in biochemical experiments, in which nanoparticles are functionalized to bond with specific proteins, which change the refractive index surrounding the nanoparticle upon bonding to it. A redshift of the nanoparticle absorption peak wavelength then signals the presence of specific proteins.

The chemical sensing application relies on an understanding of how the refractive index of a nanoparticle's medium influences absorption properties. With collaborators Scott Reed and Stephen Budy of the University of Colorado, Denver, Department of Chemistry, we planned to numerically analyze the relationship between absorption spectra and the medium refractive index. Studies of nanoparticle absorption using the computational method of finite-difference time-domain (FDTD) modeling can simulate the interaction of a particle/medium system with an exciting optical pulse.[66] Our simulation goals consisted of utilizing an FDTD simulation to predict the medium refractive index change occurring with an observed resonance shift, for the case of gold particles in water, simulated from the interaction of an optical pulse with a single nanoparticle. Additionally, an observation of peak redshifting due to medium index change can be mimicked by redshifting due to particle aggregation. We therefore planned to also simulate the spectra of collections of nanoparticles, and identify spectral features, including peak redshifting and broadening, which could distinguish the redshifting caused by aggregation from that of medium index change.

However, we initially find that significant discrepancies exist between spectral simulation results and experimental spectra. Part of the discrepancy is explained by varying literature values for the dielectric function of gold,[107] which underlies its refractive index

and absorption properties, and is used as an input to an FDTD model. The implementation of FDTD we used for calculations expresses the dielectric function with the Lorentz-Drude (LD) model, which represents the electronic behavior in gold as a combination of distinct scattering and resonance responses. Agreement is improved by fitting the LD model to recent experimental dielectric function data.[108] Despite this improved agreement, significant differences remain between the modeled and measured spectra (shown in figure 7.5 below). We find that close agreement of the FDTD model and experimental spectra would require an FDTD implementation which can represent the dielectric function as an interpolation to data in a tabular format, rather than relying on the LD form. Without accurate spectra for single particles, we were unable to proceed to multiparticle simulations. However, we identified the source of the discrepancy as the dielectric function of gold provided with the simulation software, and found recent dielectric data which we used to calculate improved absorption spectra.

7.2 FDTD modeling method

The finite-difference time-domain[109] numerical analysis method uses Faraday's and Ampère's laws to approximate the electric and magnetic fields throughout a region in response to a given incident wave. The incident wave is known over a set of points at the beginning of the simulation time, and the fields throughout the simulation region are calculated from these known fields over the total simulation time. In our simulations, we then use the field values to calculate the optical power leaving the region, and subtract the result from the incident power to find the nanoparticle absorbed power.

The only condition on Maxwell's equations is that the system has no free charges or currents. In our simulations, we also assumed that materials were non-magnetic, and that the dielectric function of the materials is not explicitly time-dependent. Faraday's and

Ampère's laws then read

$$\epsilon(\vec{r},\omega)\frac{\partial \vec{E}}{\partial t} = \nabla \times \vec{H} \tag{7.1}$$

$$\mu_0 \frac{\partial \vec{H}}{\partial t} = -\nabla \times \vec{E} \tag{7.2}$$

The simulation region is defined as two orthorhombic lattices, one each for $\vec{E}$ and $\vec{H}$, with side lengths Δx, Δy, and Δz. The two lattices are offset from each other by half the side length in each direction, giving finite difference approximation accuracy to the second degree in side length. Beginning with an isolated particle of 20 nm diameter, we used successively smaller values of the side length starting from about 3 nm, until we saw less than 1% change between successive values. Our simulation used cubic lattices with fianl values of $\Delta x = \Delta y = \Delta z = 1.3\,\text{nm}$ for both fields. A lattice cell is shown in figure 7.1. Fields values are defined at the midpoints of the edges of each lattice: in the figure, components of $\vec{E}$ are defined at the blue points shown, and components of $\vec{H}$ at the black points. Unlike a region in continuous space, only one of three components is defined at each field point. Time is also discretized with step Δt. At each time step, the $\vec{H}$ field is calculated from the $\vec{E}$ field values from half a time step earlier, and vice-versa, so that field values are staggered in both space and time. The value of a field component at a given point and time step is found from its value at the previous full time step and from the four components of the other field lying on the edges of the square centered on the point of interest. For example, in figure 7.1, using indices (i,j,k) and n for the lattice points and time steps, respectively, the central difference approximation for $E(i, j+\frac{1}{2}, k, n+1)$ (a y-component of $\vec{E}$) at time step $n+1$ is found from its value at step n and the four values of $H(i, j, k \pm \frac{1}{2}, n+\frac{1}{2})$ and

$H(i \pm \frac{1}{2}, j, k, n + \frac{1}{2})$ at time $n + \frac{1}{2}$ by means of Ampère's law (eq. 7.1):

$$\begin{aligned} \epsilon(i, j + \frac{1}{2}, k) \frac{E(i, j + \frac{1}{2}, k, n + 1) - E(i, j + \frac{1}{2}, k, n)}{\Delta t} \\ = \frac{[H(i, j + \frac{1}{2}, k + \frac{1}{2}, n + \frac{1}{2}) - H(i, j + \frac{1}{2}, k - \frac{1}{2}, n + \frac{1}{2})]}{\Delta x} \\ - \frac{[H(i + \frac{1}{2}, j + \frac{1}{2}, k, n + \frac{1}{2}) - H(i - \frac{1}{2}, j + \frac{1}{2}, k, n + \frac{1}{2})]}{\Delta x}. \end{aligned} \tag{7.3}$$

In general, the lattice spacing must be small enough[66] to support the shortest wavelengths

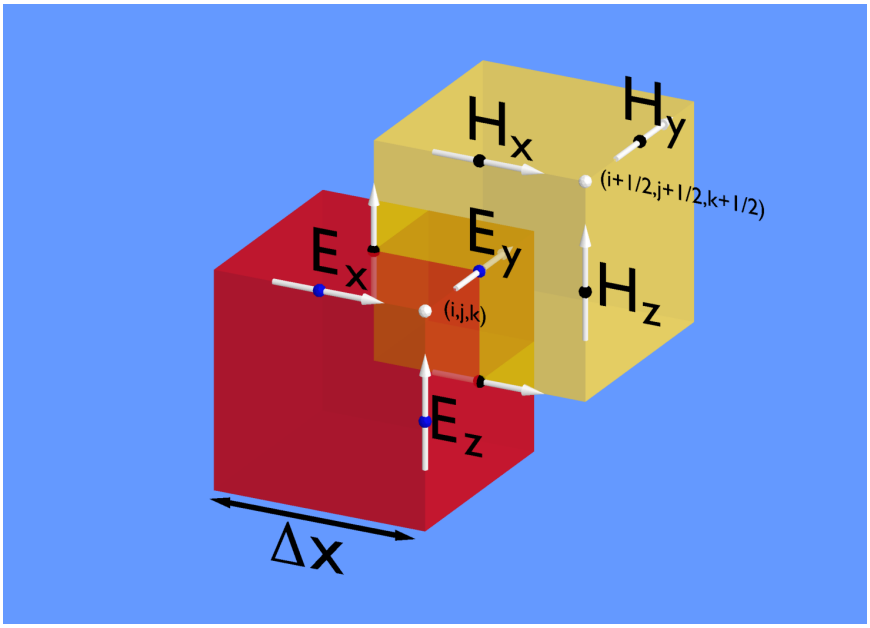

Figure 7.1: A single Yee cell in the FDTD computational domain. Both fields $\vec{E}$ and $\vec{H}$ lie on the edges of cubes defined by a cubic lattice, but with the $\vec{E}$ and $\vec{H}$ lattices staggered from each other by $\frac{\Delta x}{2}$.

present in a simulation. Ten to twenty[66] points within the shortest simulated wavelength is generally adequate; with our spectral range of 400 to 800 nm (see table 7.1), twenty points/wavelength would give a spacing of 20 nm. In our simulation we chose an even smaller value, to place about fifteen points spanning a nanoparticle diameter of 20 nm, for a spacing of 1.3 nm. The approximation error for this value was estimated as described above. The convergence in time of the approximation is dependent on satisfying the Courant-Friedrichs-Lewy[110] condition for the convergence of discrete approximations to systems of

partial differential equations. In three dimensions ($d = 3$) the condition is

$$\Delta t = S_C \frac{\Delta x}{c_0 \sqrt{d}}, \tag{7.4}$$

where the Courant number S_C lies between 0 and 1, and c_0 is the speed of light in the predominant medium. Our FDTD implementation software sets the value of S_C to 0.729 by default, determining the time step we used of $2.43 \cdot 10^{-18}$ s in an aqueous medium.

For our simulations we used the OptiWave OptiFDTD software, running on Microsoft Windows 7. The 3D arrangement of the simulation is shown in figure 7.2. The simulation region was a cube of sides 100 nm, centered on a gold nanoparticle with diameter 20 nm, in a water medium. FDTD simulations rely on two additional regions surrounding the main simulation space (called the 'total field' region), to simulate an infinite surrounding medium while also allowing truncation of the total field region to a finite size. The first layer outside the total field region is the 'scattered field' layer, which is then surrounded by the 'absorbing' layer where fields are set to zero. Truncation of the total field space artificially generates wave reflections into the simulation which become part of the model outputs. Selection of the proper scattered field layer reduces any reflections to a negligible level relative to the outgoing wave. The scattered field layer is defined by its boundary conditions and thickness in number of cells. By both enlarging the total field region, and also comparing outputs to experimental spectra, we found that a scattered field layer using 'asymmetric perfectly matched layer' (APML) boundary conditions, with a thickness of 10 cells, reduced wave reflections sufficiently. A parameter selection dialog is shown in figure 7.3.

The experimental spectra to which FDTD outputs were to be compared were taken over the spectral range of 400 to 800 nm. To generate FDTD results over this range, we made use of the ability of the FDTD method to find responses to an input defined in the time domain, but with spectral content spanning our range of interest. Figure 7.4 shows

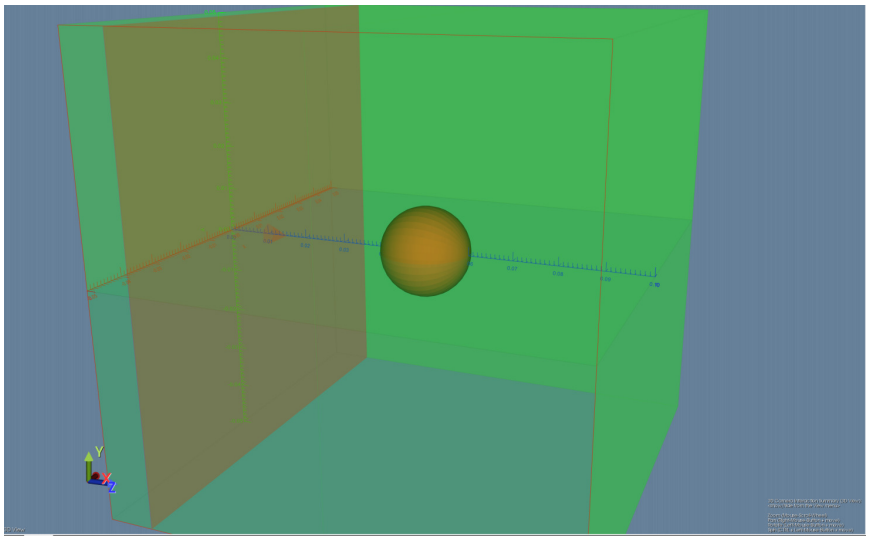

Figure 7.2: 3D editor view from the OptiFDTD Designer application of a single Au spherical nanoparticle of 20 nm diameter, with H_2O defined as the matrix material. The cubical region of the model has side length 100 nm, and the final mesh spacing was 1.3 nm. The red plane on the left was the source of the incident plane wave. The model output was the total energy passing through the right-hand plane during the simulation time.

our input waveform, and our calculated amplitude of its fast-Fourier transform. The input was a linearly-polarized plane wave with x-direction field shown in the figure. To center the wavelength peak at about 550 nm, we used an input of a 1100 nm monochromatic wave modulated by a Gaussian pulse of duration chosen to span the 400 to 800 nm range. Since optical power was our main model output, and is proportional to the square of the field strength, the power spectrum peaks at twice the frequency/half the wavelength of the input field. The final envelope duration was 10.2 fs. The FDTD software normalizes the output power spectrum to the relative input spectral amplitude. By reducing the total number of time steps of the simulation from a larger value, we found that a total time of 25 fs, about 2.5 times longer than the input pulse duration, gave convergence of the output power.

A summary of parameters used in our simulations is shown in table 7.1. The dielectric function of gold is discussed in section 7.3.

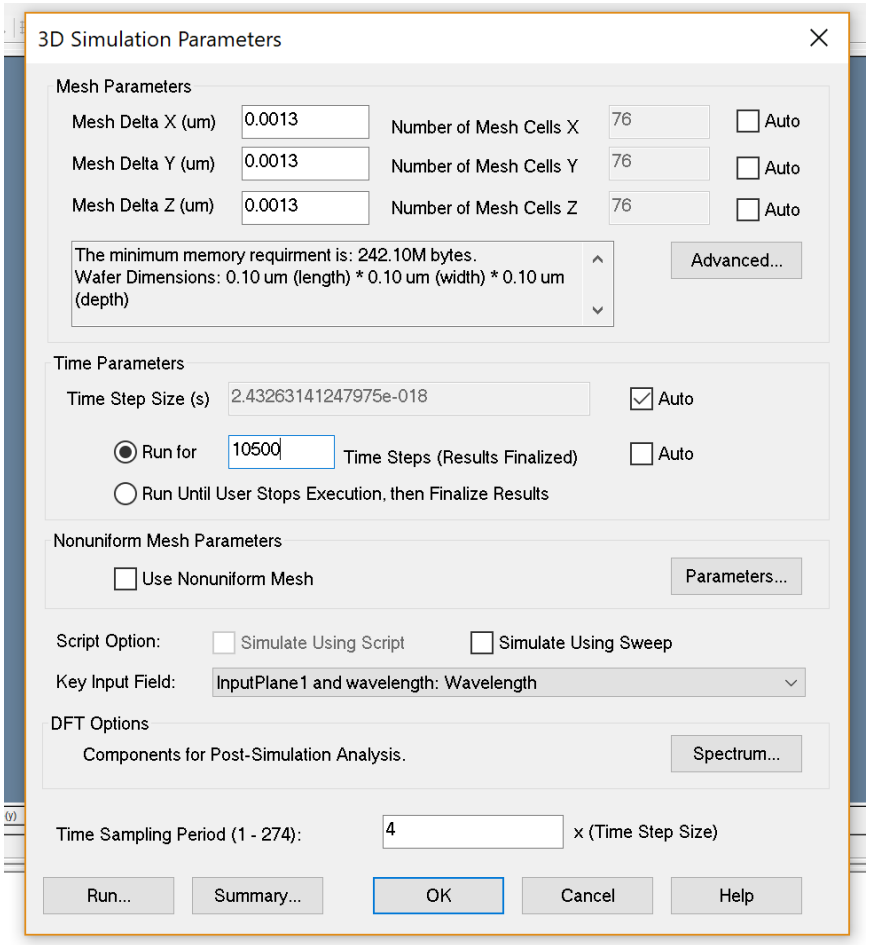

Figure 7.3: Definition of simulation parameters apart from materials. With the number of time steps at 10500 and with the default 2.43 as step duration for this model, the total simulation time was 25 fs.

7.3 FDTD modeling results

Initial absorption spectrum simulation results are shown in figure 7.5, along with spectra taken by collaborators at CU-Denver and another published spectrum.[74] Aqueous gold nanoparticles with diameter 20 nm have a well-known absorption peak near 520 nm. The experimental spectra agree well with each other, with peaks at 518 nm. Simulation results initially placed the peak at 538 nm, significantly too high, and also with a greater

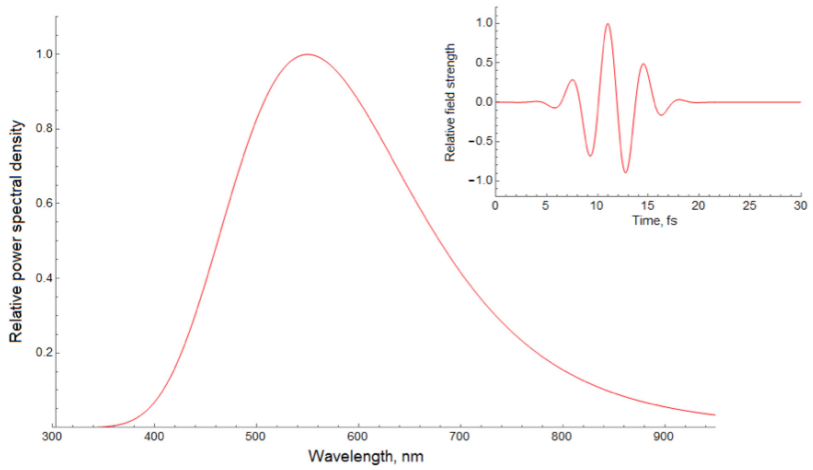

Figure 7.4: Time-domain waveform and wavelength spectrum of the input Gaussian pulse which enters the simulation from the red-colored plane of figure 7.2. The frequency spectrum of the input is actually symmetric about the peak at 550 nm, the asymmetry of the wavelength spectrum is due to the reciprocal relationship between wavelength and frequency, from $\lambda(\omega) = \frac{2\pi c/n}{\omega}$.

width than observed spectra. Several simulation features were investigated as possible causes of the discrepancy, including time step and cell sizes, scattering layer boundary conditions, computational region size, and particle diameter. Varying these features had only small effects on the final calculated spectra, but we found a large effect from varying the dielectric function of the gold particle.

These initial simulations used the dielectric function provided in the OptiFDTD Designer materials library, which was originally determined by using the Lorentz-Drude[111] (LD) phenomenological model of the dielectric function, with LD parameters determined by a fit by Djurišić *et al.*[112] of the model to early spectroscopic ellipsometry data.[102] The LD model has the form of a sum of oscillator resonances,

$$\epsilon(\omega) = \epsilon_\infty - \sum_{n=0}^{N} \frac{f_n \omega_p^2}{\omega^2 - \omega_n^2 - i\Gamma_n \omega}, \tag{7.5}$$

Finite-difference time-domain Simulation parameters		
Simulation space cube side length	100	nm
Target spectral range	400 to 800	nm
Nanoparticle diameter	20	nm
H_2O refractive index	1.33	
Time steps	10500	
Time step duration	2.43	as
Cell side length	1.3	nm
Input pulse center wavelength	1100	nm
Gaussian pulse envelope duration	10.2	fs
Scattering layer thickness	10	cells
Scattering layer boundary condition	APML	

Table 7.1: Parameters of the aqueous Au nanoparticle absorption simulation.

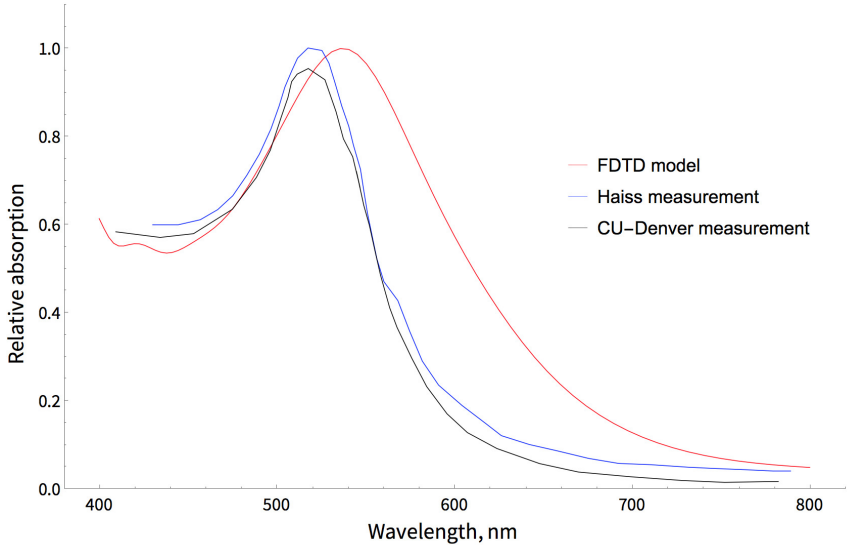

Figure 7.5: Comparison of Au nanoparticle absorption spectra between the FDTD modeled spectrum, calculated from a fit of the Au LD dielectric function model to early experimental values, and experimental spectra from collaborators at CU-Denver and published measurements.[74] The modeled absorption peak lies about 20 nm greater than the observed peak at 518 nm.

where $\epsilon(\omega)$ is the relative permittivity, ω_p is the plasma frequency for gold, ϵ_∞ is the dielectric value as $\omega \to \infty$, N is the number of Lorentz resonance peaks, f_n is the oscillator

strength, ω_n is the resonance frequency, and Γ_n is the scattering rate. The term $n = 0$ is the Drude peak representing intraband, free-electron scattering, with $\omega_1 = 0$, and the higher terms are interband resonances. The frequencies are often given in units of eV from $\hbar\omega$, while the oscillator strength parameters are dimensionless.

We also referred to an evaluation[108] by Olmon, Raschke, *et al.,* published in 2012, of several literature sources of data, which shows that literature data varied by as much as a factor of three over our spectral range of interest. The Olmon study also reported their own ellipsometry measurements of the dielectric function, using gold films and varying their surface preparation between three different methods, so that the effect of surface morphology on the dielectric function could be understood. Over our range of interest, the Olmon results varied by only $\pm 15\%$, and the results also lie near the mean of the collection of earlier studies. The authors conclude that significant systematic errors were likely present in the earlier studies.

The particular data[102] due to Lynch *et al.* used indirectly by OptiFDTD was not included in the Olmon evaluation, but was reprinted in Djurîŝiċ;[112] an interpolation is shown in figure 7.6, alongside the Olmon results. The imaginary part is plotted separately in figure 7.7, to show the significant discrepancy between the Djurîŝiċ fit used by OptiFDTD and the Olmon data. We chose to perform our own fit of the LD model to the Olmon data, and use this fit for our FDTD simulations, to achieve results which would be based on data closer to the actual properties of gold. The OptiFDTD software includes the feature of adding additional materials to the software library, as long as they are given in the LD model form. Our fits are shown in figure 7.6, along with the Olmon data, and the earlier data and fits from the materials library. Actually our fits agree better with both sets of data, especially for the imaginary part of the function. This is likely because we had the advantage of fitting over a smaller near-infrared to visible range of 1.5 to 3.2 eV (400 to 800 nm), while the

original fit was for the much larger mid-infrared to extreme ultraviolet range of 0.1 to 20 eV (12 μm to 60 nm). The final parameters of our fit, and those of the original by Djurišić,[112] are shown in table 7.2. Our fit contains two Lorentz resonances in addition to the Drude term, while for the broader spectral range, the Djurišić fit contains 6 Lorentz terms.

Gold dielectric function LD model fitting parameters							
n	0	1	2	3	4	5	6
Green							
ω_p	9.41	-	9.41	9.41	-	-	-
ω_n	0	-	2.929	4.256	-	-	-
f_n	0.866	-	0.140	0.746	-	-	-
Γ_n	0.0233	-	0.789	0.410	-	-	-
Djurišić							
ω_p	9.03	9.03	9.03	9.03	9.03	9.03	9.03
ω_n	0	0.899	2.467	6.236	9.878	13.635	19.340
f_n	1.048	1.650	4.740	0.115	2.571	4.959	8.520
Γ_n	0.083	0.970	7.177	1.236	5.489	13.286	9.398

Table 7.2: Parameters of least-squares fits of the LD model to experimental Au dielectric function data. Units are eV from $E = \hbar\omega$, except for dimensionless oscillator strengths. Both models use $\epsilon_\infty = 1$. The terms for our fit are placed at the index n of the Djurišić fit with the closest resonance.

The resulting simulations were significantly improved, with a typical spectrum shown in figure 7.8. The surface morphology which best agrees with observed spectra is that resulting from 'template stripped' surface preparation. The simulated absorption peak is now slightly wider than in the measured spectrum, and the resonance lies about 7 nm above the measured, compared with the library dielectric function which placed the peak 20 nm above the measured peak. We consider the significance of this improvement in section 7.4.

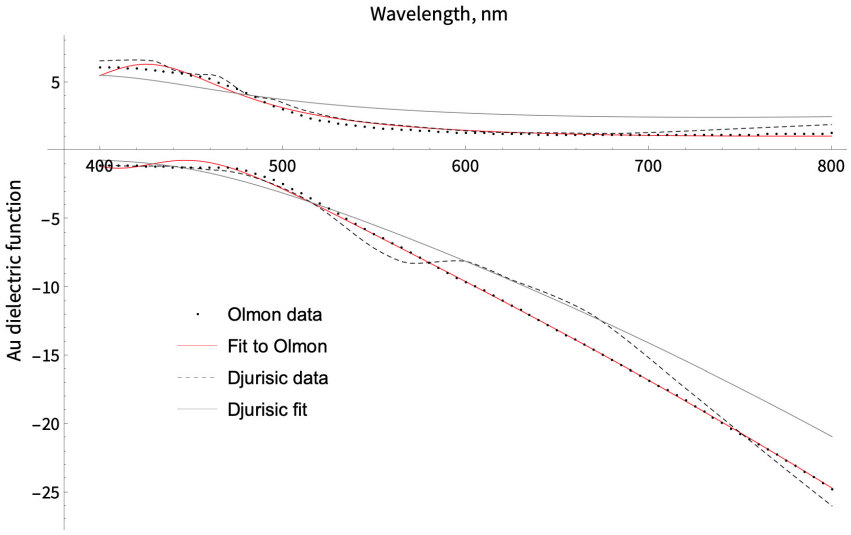

Figure 7.6: Models and measurements of the dielectric function of Au. Negative plotted values are the real part, and positive values are the imaginary part. Fits are of the Lorentz-Drude dielectric function model to recent spectroscopic ellipsometry data[108] (dotted), and to earlier data[102] (dashed). Referenced to the Olmon data, our least squares fit (red line) had an error function value of 1.9, while the earlier fit[112](gray line, originally fit to different data) had an error of 125 (also referenced to Olmon data).

7.4 Conclusions

In chemical sensing experiments and applications, the sensitivity of a nanoparticle as a sensor is typically measured in 10s to 100s of nm/(refractive index change) of resonance redshift, and a refractive index change on the order of 0.1 is a practical value. The sensitivity depends strongly on composition, shape, and size of the particle. Given these numbers, a typical desired redshift might be a few nm, so a reasonable choice for the accuracy of simulations of the peak would be about 1 nm at the most, and the discrepancy of about 7 nm was considered too large to proceed with simulating particle sensitivities and proximity effects.

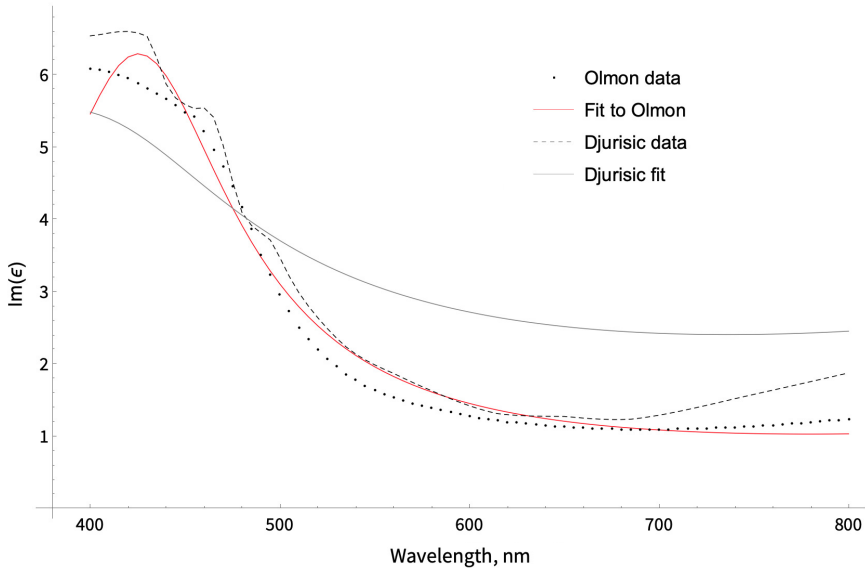

Figure 7.7: Models and measurements of the imaginary part of the dielectric function of Au.

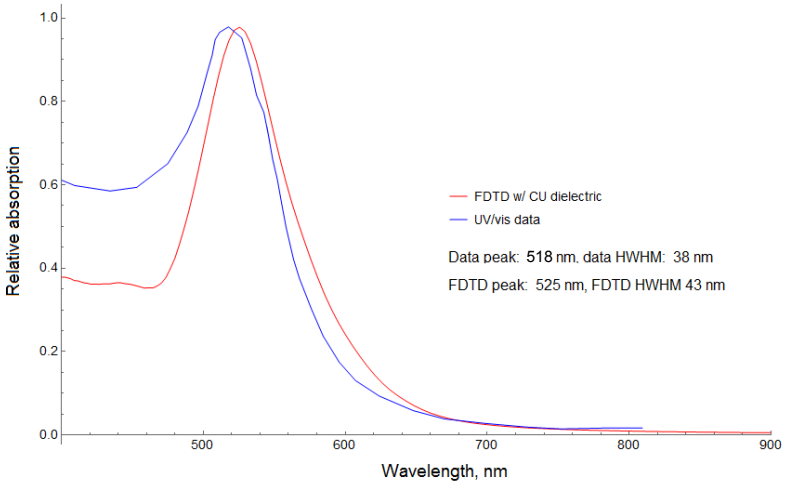

Figure 7.8: Comparison of Au nanoparticle absorption spectra between an improved FDTD modeled spectrum, calculated from a fit of the Au LD dielectric function to recent experimental values, and experimental spectra from collaborators at CU-Denver. The modeled absorption peak continues to lie above the observed peak by about 5 nm.

However, the work done by Olmon[108] *et al.* has shown us at least two reasons for the differences: the effects of surface morphology and systematic errors in measurements of the dielectric function, and has provided data which improves our simulations. Additionally, we can see a clear possibility for fully resolving the accuracy issue from figure 7.6, where the best LD model fit still carries significant differences from the observed dielectric function, especially in the imaginary part. Changing the software platform to one which is able to accept a material's function in tabular or polynomial format could readily produce more accurate simulations. Sensitivity could then be predicted by simply varying the medium index and calculating the redshift, and any width change. Additionally, utilizing 3D design software such as Blender would allow the design of particles of varying shapes and sizes, with their geometry specified by the coordinates of mesh structures which could be imported into FDTD software with such a feature.

Chapter 8

Conclusions

8.1 Nanoparticle systems

To summarize the major conclusions reached in these studies, we begin by considering the role of thermal isolation in each of the two main systems which were studied. For polymer-embedded gold nanoparticles, the low conductivity of the medium extended the thermal cooling time to the 100s of ps scale, allowing the cooling dynamics to be clearly distinguished from other effects, such as electron/phonon interaction, occurring at shorter times. For membrane studies, the bridge design of the thermal isolation platform, and thinness of the bridge layers, enabled a comparison of measurements to those done with thick substrates.

In our study of nanoparticle thermal transport, we developed a spherical multilayer model which enables the explicit separation of the effects of thermal boundary resistance and capping layer presence on transient thermoreflectance cooling measurements, in the regime of diffusive transport. The dual lock-in configuration of the transient thermoreflectance experiment achieved a high signal-to-noise ratio for measuring the small signal of oscillations at the pump beam modulation frequency. The thermal boundary resistance of the noble metal/organic interface of Au/citrate was measured within acceptable uncertainty, while other parameters were seen to converge to reasonable values in fitting the model to data.

Lastly, we saw that phonon scattering at this metallic/organic boundary is predominantly diffuse, with the diffuse mismatch model estimating a reasonably accurate resistance value.

For future work with boundary transport in multilayer nanoparticles, our study pointed to identifiable improvements: measuring or confirming more experimental parameters, rather than estimating from literature, would be important. The greatest value would lie in measuring the thermal conductivity of the citrate capping layer, and of the matrix polymer. For the matrix polymer, its conductivity is a controlling parameter of the cooling process: a sensitivity calculation of its value could be done with the existing model, and its uncertainty determined from the sensitivity and measurement uncertainty. Similarly, measurements on a similar sample with capping layers of increasing thickness could improve the measurement sensitivity of the capping layer conductivity. Possibilities for more accurate determination of such parameters is discussed in section 8.3.2 below.

8.2 Membrane systems

Thermal isolation of the bridge structure films and membrane substrates enabled us to make initial measurements of any effect of large thickness of substrates on the cooling dynamics of a metallic film. This was an experiment which tested the reasonable but unconfirmed assumption that transport in a thick, relatively insulating substrate, with phonon mean-free-paths much smaller than film thickness, occurs near the film/substrate boundary. We showed that the observed transient thermoreflectance signal was indeed due to the structure cooling dynamics, and that mounting bridge structures on manual, three-axis translation stages was a simple and effective method of sample alignment.

Although the observed cooling times of this system were on the expected time scale, our agreement between data and the multilayer diffusive model needs to be improved. Two opportunities in this direction are apparent from the work so far: removing any structure-

to-air conduction by performing measurements in a vacuum, and including any signal offset due to pump leak-through to the photodetector in analysis of data. Also in contrast to the above ideas about transport, evidence of in-plane transport in the SiN beams of the thermal isolation platform was observed in studies by the Zink research group.[100] With these improvements in place, and with length scales on the order of 100s of nm and larger, fitting the diffusive transport model we have described to TTR data could reveal whether the above assumptions prove to be valid, or if transport by long mean-free-path phonons is also observed in the cross-plane direction. If possible, performing TTR experiments with a series of platforms with increasing bridge thickness could be a probe of the upper phonon mean-free-path cutoff of significant contribution to transport.

8.3 Nanothermal research outlooks

Nanothermal transport is an active and rich area of research, which is continuing to grow in importance as technologies continue to move toward smaller scales, and progress in understanding it more robustly is rightly considered a key to advancement in many actual and potential areas of technology. We conclude by suggesting some possibilities for the futures of transient thermoreflectance and nanothermal theoretical methods.

8.3.1 Transient thermoreflectance

As a time-resolved technique, TTR necessarily involves a pulsed laser source, and for nanoscale systems, the required pulse duration implied by cooling times on the order of 100s of ps, or faster, is on the ultrafast or 100 fs scale of pulse duration, or faster. The availability of such lasers up to high optical powers, including wavelength-tunable lasers, means that many systems of interest can be probed. The photon energies are more limited in general, but advancements such as tabletop pulsed x-ray sources[113] continue to appear.

An area of greater limitation for TTR is in the materials and systems being studied: a sufficient coefficient of thermoreflectance is necessary for a measureable signal, and practical minimum beam waist diameters sit at several microns, at least an order of magnitude larger than many systems of interest. Again, for a measureable signal, a significant fraction of the probe pulse energy must be reflected from the cooling nanostructure.

We suggest two ideas that could lead to improvements in these areas. In our gold nanoparticle experiments, we confirmed that, with sufficiently long integration times, and measurement repetitions, a high signal-to-noise ratio could be achieved even when the photon excitation energy (1.55 eV/800 nm in our experiments) was significantly below, but still in the vicinity of, the interband transition threshold (2.54 eV/494 nm for gold), where the thermoreflectance peak occurs. The greatest contribution to the thermoreflectance coefficient in this case is increased phonon population and resulting electron-phonon scattering with temperature, as opposed to the changes in available electron states near the Fermi level that occur near the ITT energy. Workers in the Halas group also observed such a thermoreflectance response,[62] where it is identified as a temperature-induced change in the screening role of hot electrons. If the screening effect is sufficiently strong in typical nanodevice materials, TTR experiments could potentially probe thermal dynamics in devices without requiring the addition of thermoreflective materials to serve as transducers.

TTR experiments with nanoparticles successfully collect a signal from large numbers of nanoparticle arrays, *i.e.* large numbers of sub-spot size particles contribute to a measureable probe pulse reflection. This suggests designing arrays of nanodevices which reach up to the spot size in total extent, and where a single device electrode is accessible to pump/probe pulses, *e.g.* a CMOS array in which only the source electrodes are exposed, while other connections are masked. A single device is too small to be probed by a 'large' laser spot, but an array of devices, fabricated by a stable system with a sufficiently narrow distribution

of variables such as dimensions, surface roughnesses and defect densities, could enable the measurement of thermal features of real devices.

As a broader consideration, typically several secondary, but important, parameters of materials, such as a matrix conductivity, of an experiment require determination, with minimal uncertainty, to enable the calculation of a final desired quantity through fittings of a model to data, and with minimal uncertainty in the final result. Of course, literature values may be available, but there is no real substitute for measurements of the actual device under study. In many research settings, independent methods of measuring such parameters could be available, but are often macroscale methods, and therefore possibly inapplicable, or if capable of nanoscale measurements, may have limitations of availability and access. Simply put, there are great benefits to a TTR experiment that can be shown to be itself sensitive to the values of several parameters. We consider possible advances in this experimental area by means of theoretical improvements in the following subsection.

8.3.2 Nanothermal theory

Relaxing certain simplifying assumptions suggests some opportunities for improvements in the theoretical areas of models of TBR and in models of transport. We begin with TBR modeling.

Two fairly clear strategies can be visualized for TBR models: utilizing exact phonon dispersions,[33] rather than assuming a Debye approximation, when metals and other crystals are involved, and accounting for mixed specular/diffuse phonon transmission and reflection at a boundary, rather than assuming one of the extremes of fully specular/acoustic or diffuse mismatch models. These models also assume thermal equilibrium at interfaces, but since TTR experiments can function well with only about 1 K temperature differences, this is likely a milder assumption than that of phonon dispersions. The equilibrium approxima-

tion allows the calculation of transmission probabilities with the knowledge of the phonon dispersion on only one side of the interface, so if one material is crystalline with a known spectrum, that side can be used. To address the issue of mixed specular/diffuse interaction, we note that both the AMM and the DMM find TBC from the same equation for flux, and differ only in the calculation of transmission probabilities. The probability, already a function of polarization and frequency, could have dependence on one additional binary variable m specifying interaction mode (specular or diffuse), itself a function of phonon frequency: at frequencies of greater overlap of energies between the two materials is greater, the specular mode is given more weight, and vice-versa, and smooth transitions between frequencies assumed. Sums would run over modes, frequencies, and polarizations. Additionally, molecular dynamics simulations could also have an important role through calculation of phonon densities of states from interatomic potentials, again in place of ideal Debye pictures.[36]

Moving further away from diffusive models toward ballistic ones, and ideally also away from the relaxation-time approximation, is far more challenging, but could ultimately lead to greater discoveries. Ballistic models rest on the solid foundation of the Boltzmann equation, but they present significant challenges: they require phonon dispersions, carrier relaxation times, and interatomic potentials which may not be known for materials of interest, and are mathematically complex, even for simple geometries.[114] Cahill[5] nevertheless discusses fully ballistic modeling as a forefront issue for two main reasons: studies aim to investigate the modification of thermal properties due to nanoscale dimensions, but often determine values by fitting incongruous diffusive models, and TBR models (inaccurately) assume thermal equilibrium at all distances from interfaces.

A great deal of insight has been reached through quasi-ballistic[115] models, which divide transport between ballistic and diffusive contributions. Application of these models to measurements[116,117] of nanoscale devices demonstrates the device scales at which ballistic

effects emerge, and how thermal properties are affected. Such models often make the relaxation-time approximation.

However, at least for the case of well-studied, crystalline materials, the works of Broido *et al.*[16] and Omini *et al.*[118] show a path forward, based mostly on first principles, with the exception of calculating the collision kernel from empirical interatomic potentials. From a mathematical perspective, calculations use an iterative, analytical method, and the method is used to calculate the bulk thermal conductivity of silicon. The authors show that modification of the interatomic potential is required for close agreement of the modeled conductivity with measurements.

If some progress can be achieved along these lines, there are many possibilities for realizing the above-mentioned potential of TTR to determine multiple thermal parameters of a nanoscale device or system. With a more robust model in place, and leveraging the capability of TTR experiments to vary excitation modulation frequencies over large ranges, the sensitivity of parameters to the TTR signal could be calculated, and experiments designed which could determine the values of the most important thermal features. Also, for a given thermal device, a true diffusive/ballistic transition could be calculated by scaling down the device size.

Specifically, if a multilayer ballistic transport model could be developed which includes TBR, exploring the boundary between diffusive and ballistic transport in these systems, with measurements of responses from a series of particles with decreasing diameter, would be an exciting project. A quasi-ballistic model of this kind has been developed by Shirdel-Havar *et al.*,[119] using a core-shell solution of the Boltzmann transport equation by Rashidi-Huyeh *et al.*,[81] the relaxation-time approximation, and the diffusive-ballistic approximation of Chen.[115] This model assumes zero TBR, but solutions are reached using a finite-difference

solution of a system of differential equations, so it is possible that a TBR term could be added to the analytical equations, and then solved numerically, as in Shirdel-Havar.[119]

Bibliography

[1] D. G. Cahill, W. K. Ford, K. E. Goodson, G. D. Mahan, A. Majumdar, H. J. Maris, R. Merlin, and S. R. Phillpot, "Nanoscale thermal transport," Journal of Applied Physics, vol. 93, no. 2, pp. 793–818, 2003.

[2] D. G. Cahill, "Analysis of heat flow in layered structures for time-domain thermoreflectance," Review of scientific instruments, vol. 75, no. 12, pp. 5119–5122, 2004.

[3] H. S. Carslaw, J. C. Jaeger, and H. Feshbach, "Conduction of heat in solids," Physics Today, vol. 15, p. 74, 1962.

[4] D. Gall, "Electron mean free path in elemental metals," Journal of Applied Physics, vol. 119, no. 8, p. 085101, 2016.

[5] D. G. Cahill, P. V. Braun, G. Chen, D. R. Clarke, S. Fan, K. E. Goodson, P. Keblinski, W. P. King, G. D. Mahan, A. Majumdar, et al., "Nanoscale thermal transport II. 2003–2012," Applied Physics Reviews, vol. 1, no. 1, p. 011305, 2014.

[6] W. Liu, K. Etessam-Yazdani, R. Hussin, and M. Asheghi, "Modeling and data for thermal conductivity of ultrathin single-crystal soi layers at high temperature," IEEE Transactions on Electron Devices, vol. 53, no. 8, pp. 1868–1876, 2006.

[7] K. Imaizumi, T. Ono, T. Kota, S. Okamoto, and S. Sakurai, "Transformation of cubic symmetry for spherical microdomains from face-centred to body-centred cubic upon uniaxial elongation in an elastomeric triblock copolymer," Journal of applied crystallography, vol. 36, no. 4, pp. 976–981, 2003.

[8] W. Setyawan and S. Curtarolo, "High-throughput electronic band structure calculations: Challenges and tools," Computational Materials Science, vol. 49, no. 2, pp. 299–312, 2010.

[9] J. Behari and B. Tripathi, "Phonon dispersion relations in noble metals," Journal of Physics C: Solid State Physics, vol. 3, no. 3, p. 659, 1970.

[10] J. Lynn, H. Smith, and R. Nicklow, "Lattice dynamics of gold," Physical Review B, vol. 8, no. 8, p. 3493, 1973.

[11] J. Turney, E. Landry, A. McGaughey, and C. Amon, "Predicting phonon properties and thermal conductivity from anharmonic lattice dynamics calculations and molecular dynamics simulations," Physical Review B, vol. 79, no. 6, p. 064301, 2009.

[12] A. Maradudin and A. Fein, "Scattering of neutrons by an anharmonic crystal," Physical Review, vol. 128, no. 6, p. 2589, 1962.

[13] S. Tamura and H. Maris, "Temperature dependence of phonon lifetimes in dielectric crystals," Physical Review B, vol. 51, no. 5, p. 2857, 1995.

[14] A. Akhieser, "On the absorption of sound in solids," J. Phys.(Ussr), vol. 1, p. 277, 1939.

[15] H. Maris, "Phonon viscosity," Physical Review, vol. 188, no. 3, p. 1303, 1969.

[16] D. Broido, A. Ward, and N. Mingo, "Lattice thermal conductivity of silicon from empirical interatomic potentials," Physical Review B, vol. 72, no. 1, p. 014308, 2005.

[17] D. Broido, M. Malorny, G. Birner, N. Mingo, and D. Stewart, "Intrinsic lattice thermal conductivity of semiconductors from first principles," Applied Physics Letters, vol. 91, no. 23, p. 231922, 2007.

[18] A. Ward, D. Broido, D. A. Stewart, and G. Deinzer, "Ab initio theory of the lattice thermal conductivity in diamond," Physical Review B, vol. 80, no. 12, p. 125203, 2009.

[19] P. Kapitza, "The study of heat transfer in helium ii," J. Phys.(USSR), vol. 4, no. 1-6, pp. 181–210, 1941.

[20] E. T. Swartz and R. O. Pohl, "Thermal boundary resistance," Rev. Mod. Phys., vol. 61, no. 3, p. 605, 1989.

[21] I. M. Khalatnikov, "Teploobmen mezhdu tverdym telom i geliem-ii," Zhurnal Eksperimentalnoi I Teoreticheskoi Fiziki, vol. 22, no. 6, pp. 687–704, 1952.

[22] E. Swartz and R. Pohl, "Thermal resistance at interfaces," Applied Physics Letters, vol. 51, no. 26, pp. 2200–2202, 1987.

[23] Z. Ge, D. G. Cahill, and P. V. Braun, "Thermal conductance of hydrophilic and hydrophobic interfaces," Physical review letters, vol. 96, no. 18, p. 186101, 2006.

[24] N. Shenogina, R. Godawat, P. Keblinski, and S. Garde, "How wetting and adhesion affect thermal conductance of a range of hydrophobic to hydrophilic aqueous interfaces," Physical review letters, vol. 102, no. 15, p. 156101, 2009.

[25] M. Shen, W. J. Evans, D. Cahill, and P. Keblinski, "Bonding and pressure-tunable interfacial thermal conductance," Physical Review B, vol. 84, no. 19, p. 195432, 2011.

[26] R. Prasher, "Acoustic mismatch model for thermal contact resistance of van der waals contacts," Applied Physics Letters, vol. 94, no. 4, p. 041905, 2009.

[27] L. Hu, T. Desai, and P. Keblinski, "Determination of interfacial thermal resistance at the nanoscale," Physical Review B, vol. 83, no. 19, p. 195423, 2011.

[28] S. T. Huxtable, D. G. Cahill, S. Shenogin, L. Xue, R. Ozisik, P. Barone, M. Usrey, M. S. Strano, G. Siddons, M. Shim, et al., "Interfacial heat flow in carbon nanotube suspensions," Nature materials, vol. 2, no. 11, pp. 731–734, 2003.

[29] J. Cheeke, H. Ettinger, and B. Hebral, "Analysis of heat transfer between solids at low temperatures," Canadian Journal of Physics, vol. 54, no. 17, pp. 1749–1771, 1976.

[30] N. Snyder, "Heat transport through helium ii: Kapitza conductance," Cryogenics, vol. 10, no. 2, pp. 89–95, 1970.

[31] H.-K. Lyeo and D. G. Cahill, "Thermal conductance of interfaces between highly dissimilar materials," Physical Review B, vol. 73, no. 14, p. 144301, 2006.

[32] J. C. Duda, J. L. Smoyer, P. M. Norris, and P. E. Hopkins, "Extension of the diffuse mismatch model for thermal boundary conductance between isotropic and anisotropic materials," Applied Physics Letters, vol. 95, no. 3, p. 031912, 2009.

[33] P. Reddy, K. Castelino, and A. Majumdar, "Diffuse mismatch model of thermal boundary conductance using exact phonon dispersion," Applied Physics Letters, vol. 87, no. 21, p. 211908, 2005.

[34] D. Young and H. Maris, "Lattice-dynamical calculation of the kapitza resistance between fcc lattices," Physical Review B, vol. 40, no. 6, p. 3685, 1989.

[35] B. C. Gundrum, D. G. Cahill, and R. S. Averback, "Thermal conductance of metal-metal interfaces," Physical Review B, vol. 72, no. 24, p. 245426, 2005.

[36] M. E. Caplan, A. Giri, and P. E. Hopkins, "Analytical model for the effects of wetting on thermal boundary conductance across solid/classical liquid interfaces," The Journal of Chemical Physics, vol. 140, no. 15, p. 154701, 2014.

[37] D. Bolmatov, V. Brazhkin, and K. Trachenko, "The phonon theory of liquid thermodynamics," Scientific reports, vol. 2, p. 421, 2012.

[38] N. W. Ashcroft and N. D. Mermin, Solid State Physics. Saunders College, 1976.

[39] W. S. Capinski and H. J. Maris, "Improved apparatus for picosecond pump-and-probe optical measurements," Review of Scientific Instruments, vol. 67, no. 8, pp. 2720–2726, 1996.

[40] Z. Ge, D. G. Cahill, and P. V. Braun, "Aupd metal nanoparticles as probes of nanoscale thermal transport in aqueous solution," J. Phys. Chem. B, vol. 108, no. 49, pp. 18 870–18 875, 2004.

[41] Z. Ge, Y. Kang, T. A. Taton, P. V. Braun, and D. G. Cahill, "Thermal transport in au-core polymer-shell nanoparticles," Nano Lett., vol. 5, no. 3, pp. 531–535, 2005.

[42] T. Rangel, D. Kecik, P. Trevisanutto, G.-M. Rignanese, H. Van Swygenhoven, and V. Olevano, "Band structure of gold from many-body perturbation theory," Physical Review B, vol. 86, no. 12, p. 125125, 2012.

[43] R. Rosei and D. W. Lynch, "Thermomodulation spectra of Al, Au, and Cu," Physical Review B, vol. 5, no. 10, p. 3883, 1972.

[44] R. Wilson, B. A. Apgar, L. W. Martin, and D. G. Cahill, "Thermoreflectance of metal transducers for optical pump-probe studies of thermal properties," Opt. Express, vol. 20, no. 27, pp. 28 829–28 838, 2012.

[45] E. Colavita, A. Franciosi, R. Rosei, F. Sacchetti, E. Giuliano, R. Ruggeri, and D. W. Lynch, "Electronic structure of nb-mo alloys," Physical Review B, vol. 20, no. 12, p. 4864, 1979.

[46] M. E. Siemens, "Nanoscale thermal, acoustic, and magnetic dynamics probed with soft x-ray light," Ph.D. dissertation, University of Colorado, 2010.

[47] D. Von der Linde, K. Sokolowski-Tinten, and J. Bialkowski, "Laser–solid interaction in the femtosecond time regime," Applied Surface Science, vol. 109, pp. 1–10, 1997.

[48] J. Hohlfeld, S.-S. Wellershoff, J. Güdde, U. Conrad, V. Jähnke, and E. Matthias, "Electron and lattice dynamics following optical excitation of metals," Chemical Physics, vol. 251, no. 1, pp. 237–258, 2000.

[49] P. B. Johnson and R.-W. Christy, "Optical constants of the noble metals," Physical review B, vol. 6, no. 12, p. 4370, 1972.

[50] S. Anisimov, "Effect of very short laser pulses on absorbing substances," Sov. Phys. JETP, vol. 31, no. 1, pp. 181–182, 1970.

[51] M. Hu, P. Keblinski, and P. K. Schelling, "Kapitza conductance of silicon–amorphous polyethylene interfaces by molecular dynamics simulations," Physical Review B, vol. 79, no. 10, p. 104305, 2009.

[52] W. S. Werner, K. Glantschnig, and C. Ambrosch-Draxl, "Optical constants and inelastic electron-scattering data for 17 elemental metals," Journal of Physical and Chemical Reference Data, vol. 38, no. 4, pp. 1013–1092, 2009.

[53] R. Letfullin, V. Zharov, C. Joenathan, and T. George, "Nanophotothermolysis of cancer cells," SPIE Newsroom DOI, vol. 10, no. 2.1200701, pp. 0634–1, 2007.

[54] N. R. Panyala, E. M. Pena-Mendez, and J. Havel, "Gold and nano-gold in medicine: overview, toxicology and perspectives," J. Appl. Biomed., vol. 7, no. 2, pp. 75–91, 2009.

[55] M. Hu and G. V. Hartland, "Heat dissipation for au particles in aqueous solution: relaxation time versus size," J. Phys. Chem. B, vol. 106, no. 28, pp. 7029–7033, 2002.

[56] V. Juvé, M. Scardamaglia, P. Maioli, A. Crut, S. Merabia, L. Joly, N. Del Fatti, and F. Vallée, "Cooling dynamics and thermal interface resistance of glass-embedded metal nanoparticles," Phys. Rev. B, vol. 80, no. 19, p. 195406, 2009.

[57] R. Averitt, S. Westcott, and N. Halas, "Ultrafast electron dynamics in gold nanoshells," Physical Review B, vol. 58, no. 16, p. R10203, 1998.

[58] M. B. Mohamed, T. S. Ahmadi, S. Link, M. Braun, and M. A. El-Sayed, "Hot electron and phonon dynamics of gold nanoparticles embedded in a gel matrix," Chemical physics letters, vol. 343, no. 1, pp. 55–63, 2001.

[59] C. Guillon, P. Langot, N. Del Fatti, F. Vallée, A. Kirakosyan, T. Shahbazyan, T. Cardinal, and M. Treguer, "Coherent acoustic vibration of metal nanoshells," Nano letters, vol. 7, no. 1, pp. 138–142, 2007.

[60] G. A. Antonelli, H. J. Maris, S. G. Malhotra, and J. M. Harper, "A study of the vibrational modes of a nanostructure with picosecond ultrasonics," Physica B: Condensed Matter, vol. 316, pp. 434–437, 2002.

[61] R. Averitt, D. Sarkar, and N. Halas, "Plasmon resonance shifts of Au-coated Au_2S nanoshells: insight into multicomponent nanoparticle growth," Physical Review Letters, vol. 78, no. 22, p. 4217, 1997.

[62] R. D. Averitt, S. L. Westcott, and N. J. Halas, "Ultrafast optical properties of gold nanoshells," JOSA B, vol. 16, no. 10, pp. 1814–1823, 1999.

[63] M. D. Losego, M. E. Grady, N. R. Sottos, D. G. Cahill, and P. V. Braun, "Effects of chemical bonding on heat transport across interfaces," Nature materials, vol. 11, no. 6, pp. 502–506, 2012.

[64] O. M. Wilson, X. Hu, D. G. Cahill, and P. V. Braun, "Colloidal metal particles as probes of nanoscale thermal transport in fluids," Phys. Rev. B, vol. 66, no. 22, p. 224301, 2002.

[65] K. M. Stocker, S. M. Neidhart, and J. D. Gezelter, "Interfacial thermal conductance of thiolate-protected gold nanospheres," Journal of Applied Physics, vol. 119, no. 2, p. 025106, 2016.

[66] C. Oubre and P. Nordlander, "Optical properties of metallodielectric nanostructures calculated using the finite difference time domain method," The Journal of Physical Chemistry B, vol. 108, no. 46, pp. 17 740–17 747, 2004.

[67] J.-P. Mulet, K. Joulain, R. Carminati, and J.-J. Greffet, "Nanoscale radiative heat transfer between a small particle and a plane surface," Applied Physics Letters, vol. 78, no. 19, pp. 2931–2933, 2001.

[68] N. G. Khlebtsov, V. A. Bogatyrev, L. A. Dykman, and A. G. Melnikov, "Spectral extinction of colloidal gold and its biospecific conjugates," Journal of colloid and interface science, vol. 180, no. 2, pp. 436–445, 1996.

[69] B. Khlebtsov, A. Melnikov, V. Zharov, and N. Khlebtsov, "Absorption and scattering of light by a dimer of metal nanospheres: comparison of dipole and multipole approaches," Nanotechnology, vol. 17, no. 5, p. 1437, 2006.

[70] U. Kreibig and L. Genzel, "Optical absorption of small metallic particles," Surface Science, vol. 156, pp. 678–700, 1985.

[71] A. L. Aden and M. Kerker, "Scattering of electromagnetic waves from two concentric spheres," Journal of Applied Physics, vol. 22, no. 10, pp. 1242–1246, 1951.

[72] J. S. Sekhon and S. Verma, "Refractive index sensitivity analysis of Ag, Au, and Cu nanoparticles," Plasmonics, vol. 6, no. 2, pp. 311–317, 2011.

[73] H. Du, "Mie-scattering calculation," Applied Optics, vol. 43, no. 9, pp. 1951–1956, 2004.

[74] W. Haiss, N. T. Thanh, J. Aveyard, and D. G. Fernig, "Determination of size and concentration of gold nanoparticles from uv-vis spectra," Analytical chemistry, vol. 79, no. 11, pp. 4215–4221, 2007.

[75] P. K. Jain, K. S. Lee, I. H. El-Sayed, and M. A. El-Sayed, "Calculated absorption and scattering properties of gold nanoparticles of different size, shape, and composition: applications in biological imaging and biomedicine," J. Phys. Chem. B, vol. 110, no. 14, pp. 7238–7248, 2006.

[76] M. Shopa, K. Kolwas, A. Derkachova, and G. Derkachov, "Dipole and quadrupole surface plasmon resonance contributions in formation of near-field images of a gold nanosphere," Opto-Electronics Review, vol. 18, no. 4, pp. 421–428, 2010.

[77] D. Wu, X. Xu, and X. Liu, "Influence of dielectric core, embedding medium and size on the optical properties of gold nanoshells," Solid State Communications, vol. 146, no. 1, pp. 7–11, 2008.

[78] A. Feldman, "Algorithm for solutions of the thermal diffusion equation in a stratified medium with a modulated heating source," High Temp.-High Press., vol. 31, no. 3, pp. 293–298, 1999.

[79] N. Taketoshi, T. Baba, E. Schaub, and A. Ono, "Homodyne detection technique using spontaneously generated reference signal in picosecond thermoreflectance measurements," Rev. Sci. Instrum., vol. 74, no. 12, pp. 5226–5230, 2003.

[80] A. J. Schmidt, X. Chen, and G. Chen, "Pulse accumulation, radial heat conduction, and anisotropic thermal conductivity in pump-probe transient thermoreflectance," Rev. Sci. Instrum., vol. 79, no. 11, p. 114902, 2008.

[81] M. Rashidi-Huyeh, S. Volz, and B. Palpant, "Non-fourier heat transport in metal-dielectric core-shell nanoparticles under ultrafast laser pulse excitation," Physical Review B, vol. 78, no. 12, p. 125408, 2008.

[82] D. Ding, X. Chen, and A. Minnich, "Radial quasiballistic transport in time-domain thermoreflectance studied using monte carlo simulations," Appl. Phys. Lett., vol. 104, no. 14, p. 143104, 2014.

[83] G. Mahan and F. Claro, "Nonlocal theory of thermal conductivity," Phys. Rev. B, vol. 38, no. 3, p. 1963, 1988.

[84] Y. K. Koh, D. G. Cahill, and B. Sun, "Nonlocal theory for heat transport at high frequencies," Phys. Rev. B, vol. 90, no. 20, p. 205412, 2014.

[85] R. D. Averitt, S. L. Westcott, and N. J. Halas, "Ultrafast optical properties of gold nanoshells," J. Opt. Soc. Am. B, vol. 16, no. 10, p. 1814, Oct 1999. [Online]. Available: http://dx.doi.org/10.1364/JOSAB.16.001814

[86] J.-W. Park and J. S. Shumaker-Parry, "Structural study of citrate layers on gold nanoparticles: role of intermolecular interactions in stabilizing nanoparticles," J. Am. Chem. Soc., vol. 136, no. 5, pp. 1907–1921, 2014.

[87] W. M. Haynes, CRC Handbook of Chemistry and Physics. CRC press, 2014.

[88] J. A. Dean and N. A. Lange, Lange's Handbook of Chemistry, 15th ed. Mc-Graw-Hill, New York, 1998.

[89] A. Apelblat, "Properties of citric acid and its solutions," in Citric Acid. Springer, 2014, pp. 13–141.

[90] A. J. Schmidt, R. Cheaito, and M. Chiesa, "A frequency-domain thermoreflectance method for the characterization of thermal properties," Rev. Sci. Instrum., vol. 80, no. 9, p. 094901, 2009.

[91] J. E. Mark, Physical Properties of Polymers Handbook. Springer, 2007, vol. 1076.

[92] A. Jain and A. J. McGaughey, "Thermal transport by phonons and electrons in aluminum, silver, and gold from first principles," Physical Review B, vol. 93, no. 8, p. 081206, 2016.

[93] P. J. Linstrom and W. G. Mallard, "The nist chemistry webbook: A chemical data resource on the internet," Journal of Chemical & Engineering Data, vol. 46, no. 5, pp. 1059–1063, 2001.

[94] M. De Podesta, Understanding the Properties of Matter. CRC Press, 2002.

[95] A. Apelblat, E. Korin, and E. Manzurola, "Thermodynamic properties of aqueous solutions with citrate ions. compressibility studies in aqueous solutions of citric acid," The Journal of Chemical Thermodynamics, vol. 64, pp. 14–21, 2013.

[96] T. Proctor, "Sound speed measurements in solids: Absolute accuracy of an improved transient pulse method," NBS J. Res., vol. 75, no. 1, pp. 33–40, 1971.

[97] D. M. Evans, F. Hoare, and T. Melia, "Heat capacity, enthalpy and entropy of citric acid monohydrate," Transactions of the Faraday Society, vol. 58, pp. 1511–1514, 1962.

[98] C. A. Paddock and G. L. Eesley, "Transient thermoreflectance from thin metal films," Journal of Applied Physics, vol. 60, no. 1, pp. 285–290, 1986.

[99] R. Sultan, A. Avery, G. Stiehl, and B. Zink, "Thermal conductivity of micromachined low-stress silicon-nitride beams from 77 to 325 k," Journal of Applied Physics, vol. 105, no. 4, p. 043501, 2009.

[100] R. Sultan, A. Avery, J. Underwood, S. Mason, D. Bassett, and B. Zink, "Heat transport by long mean free path vibrations in amorphous silicon nitride near room temperature," Physical review B, vol. 87, no. 21, p. 214305, 2013.

[101] A. Avery, M. Pufall, and B. L. Zink, "Observation of the planar Nernst effect in permalloy and nickel thin films with in-plane thermal gradients," Physical review letters, vol. 109, no. 19, p. 196602, 2012.

[102] E. D. Palik, Handbook of Optical Constants of Solids, Five-Volume Set: Handbook of Thermo-Optic Coefficients of Optical Materials with Applications. Elsevier, 1997.

[103] S. Couet, T. Diederich, S. Stankov, K. Schlage, T. Slezak, R. Rüffer, J. Korecki, and R. Röhlsberger, "Probing the magnetic state of fe/feo/fe trilayers by multiple isotopic sensor layers," Applied Physics Letters, vol. 94, no. 16, p. 162501, 2009.

[104] T. S. Sian and G. Reddy, "Optical, structural and photoelectron spectroscopic studies on amorphous and crystalline molybdenum oxide thin films," Solar energy materials and solar cells, vol. 82, no. 3, pp. 375–386, 2004.

[105] R. Zeller and R. Pohl, "Thermal conductivity and specific heat of noncrystalline solids," Physical Review B, vol. 4, no. 6, p. 2029, 1971.

[106] P. R. West, S. Ishii, G. V. Naik, N. K. Emani, V. M. Shalaev, and A. Boltasseva, "Searching for better plasmonic materials," Laser & Photonics Reviews, vol. 4, no. 6, pp. 795–808, 2010.

[107] A. D. Rakić, A. B. Djurišić, J. M. Elazar, and M. L. Majewski, "Optical properties of metallic films for vertical-cavity optoelectronic devices," Applied optics, vol. 37, no. 22, pp. 5271–5283, 1998.

[108] R. L. Olmon, B. Slovick, T. W. Johnson, D. Shelton, S.-H. Oh, G. D. Boreman, and M. B. Raschke, "Optical dielectric function of gold," Physical Review B, vol. 86, no. 23, p. 235147, 2012.

[109] K. Yee, "Numerical solution of initial boundary value problems involving Maxwell's equations in isotropic media," IEEE Transactions on antennas and propagation, vol. 14, no. 3, pp. 302–307, 1966.

[110] R. Courant, K. Friedrichs, and H. Lewy, "Über die partiellen differenzengleichungen der mathematischen physik," Mathematische annalen, vol. 100, no. 1, pp. 32–74, 1928.

[111] C. Powell, "Analysis of optical-and inelastic-electron-scattering data. ii. application to al," JOSA, vol. 60, no. 1, pp. 78–93, 1970.

[112] A. B. Djurišić, J. M. Elazar, and A. D. Rakić, "Modeling the optical constants of solids using genetic algorithms with parameter space size adjustment," Optics Communications, vol. 134, no. 1-6, pp. 407–414, 1997.

[113] T. Popmintchev, M.-C. Chen, D. Popmintchev, P. Arpin, S. Brown, S. Ališauskas, G. Andriukaitis, T. Balčiunas, O. D. Mücke, A. Pugzlys, et al., "Bright coherent ultrahigh harmonics in the kev x-ray regime from mid-infrared femtosecond lasers," science, vol. 336, no. 6086, pp. 1287–1291, 2012.

[114] A. J. Minnich, "Determining phonon mean free paths from observations of quasiballistic thermal transport," Physical review letters, vol. 109, no. 20, p. 205901, 2012.

[115] G. Chen, "Ballistic-diffusive heat-conduction equations," Physical Review Letters, vol. 86, no. 11, p. 2297, 2001.

[116] A. J. Minnich, J. Johnson, A. Schmidt, K. Esfarjani, M. Dresselhaus, K. A. Nelson, and G. Chen, "Thermal conductivity spectroscopy technique to measure phonon mean free paths," Physical review letters, vol. 107, no. 9, p. 095901, 2011.

[117] M. E. Siemens, Q. Li, R. Yang, K. A. Nelson, E. H. Anderson, M. M. Murnane, and H. C. Kapteyn, "Quasi-ballistic thermal transport from nanoscale interfaces observed using ultrafast coherent soft x-ray beams," Nat. Mater., vol. 9, no. 1, pp. 26–30, 2010.

[118] M. Omini and A. Sparavigna, "An iterative approach to the phonon boltzmann equation in the theory of thermal conductivity," Physica B: Condensed Matter, vol. 212, no. 2, pp. 101–112, 1995.

[119] A. Shirdel-Havar and R. Masoudian Saadabad, "Ballistic-diffusive approximation for the thermal dynamics of metallic nanoparticles in nanocomposite materials," Journal of Applied Physics, vol. 117, no. 11, p. 114304, 2015.